Studies on the Mid-latitude Ionospheric Electric Field Fluctuations(Dissertation_全文)

AUTHOR(S):

Saito, Akinori

学位申請論文

齊藤 昭則

Studies on the Mid-latitude Ionospheric Electric Field Fluctuations

A. Saito

Dissertation for the degree of Doctor of Science

Department of Geophysics, Graduate School of Science
Kyoto University

January 1997

Acknowledgments.

I wish to thank Prof. T. Araki and Drs. T. Iyemori and M. Takeda for their instructive guidance on this study. DE 2 data are provided by Drs. N. C. Maynard and J. A. Slavin. The MU radar observations were carried out with the cooperation of the staff of Radio Atmospheric Science Center at Kyoto University, especially, Profs. S. Fukao and T. Tsuda and Dr. M. Yamamoto. Freja data are provided by Dr. L. G. Blomberg. Ionograms of the Kokubunji observatory are provided by WDC-C2 for ionosphere, operated by the Communications Research Laboratory(CRL), Japan. Softwares of IRI 90 and MSIS 86 models are provided by National Space Science Data Center at NASA, and of IGRF 95 model is provided by Data Analysis Center for Geomagnetism and Space Magnetism at Kyoto University. I thank all of them for their cooperation.

PREFACE

The start point of this study was our finding of the mid-latitude electric field in the satellite data. Although the observations of electric field fluctuations observed by satellites have been studied for three decades, those studies are concentrated on the high latitude and equatorial regions. There had been little reports on the mid-latitude electric fluctuations.

At the first step, we studied the characteristics of these fluctuations, which are termed as mid-latitude ionospheric electric field fluctuations (MEFs), using the data obtained by the DE-2 satellite. Their morphology, occurrence distribution and relation with the other plasma parameters are studied. This part of my study is reported in Chapter 1 of this thesis.

Two of the most interesting features of MEFs are the fact that they often appear magnetically conjugate points simultaneously, and that they are not accompanied by any significant plasma density variations. These features indicate the uniqueness of MEFs compared with the other phenomena at high latitudes and equatorial region.

The information derived by the single satellite, DE-2, is restricted though the scale size of MEFs are large in the horizontal direction and the direction along the geomagnetic field line. Therefore we carried out the coordinated observation with a ground-based radar, the MU radar, and a satellite, Freja. The purpose of this coordinated observation was to obtain some clues about the generation process of MEFs, whose source region is supposed to be inside the ionosphere. This conjugate observation with the MU radar and the Freja satellite is reported in Chapter 2. The linear analysis of the Perkins instability inside traveling ionospheric irregularities are also discussed.

A numerical simulation is made to clarify the generation mechanism of MEFs. The results of this simulation is reported in Chapter 3. We simulate the evolution of the irregularities in

two-dimension. The results derived by this simulation are compared with the observational results in Chapter 1 and 2.

In Chapter 4, the results are summarized and the un-resolved questions are discussed.

Chapter 1.

Mid-latitude Electric Field Fluctuations Observed by the DE-2 satellite

1.1 Introduction

Midlatitude ionospheric irregularities have been observed by techniques such as ionosondes and incoherent scatter radars or by satellite instrumentation. Several authors have reported that midlatitude irregularities such as spread-F and scintillations appear simultaneously at magnetically conjugate points in the northern and southern hemispheres [*Yeh et al.*, 1968; *Rodger*, 1976; *Zinchenko and Nisbet*, 1977; *Rodger and Aarons*, 1988]. Using scintillation data and spread-F data, *Rodger and Aarons* [1988] reported that about 75% of nighttime medium-scale (1- to 10-km) F region irregularities appear simultaneously at conjugate points.

The midlatitude ionospheric electric field is generally stable compared with that at high latitudes and in the equatorial zone. As to midlatitude ionospheric electric field observations by satellites, ac electric field (4 Hz to 4 kHz) fluctuations were observed by OGO 6 in the topside ionosphere between $\pm 35°$ geomagnetic latitude in the 2000−0600 hours local time

sector [*Holtet et al.*, 1977]. Among these electric field fluctuations the most frequently observed type was accompanied by plasma density variations.

Another interesting midlatitude ionospheric phenomenon is the midlatitude F region field-aligned irregularities (FAIs) observed by incoherent scatter (IS) radar [*Fukao and Kelley*, 1991]. These F region FAIs are observed in the nighttime midlatitude F region. Inside an FAI the plasma moves upward with speeds of a few hundred meters per second and has field-aligned structures. The region of FAI moves westward with speeds of 100−200 m/s.

In this paper we report on the characteristics of the midlatitude ionospheric electric field fluctuations (MEFs), which often appear simultaneously at magnetically conjugate points, and discuss the relation between these electric field fluctuations and the F region FAIs. In situ observations of the midlatitude ionospheric electric field by satellites play an important role in understanding the mechanism of the ionospheric irregularities which have been observed by ground-based techniques.

1.2 Observation

The DE 2 satellite flew in polar orbit at about 250-km to 900-km altitudes. It observed the ionospheric electric field at midlatitudes from August 1981 to February 1983 in 3482 orbits. The sampling interval of electric field measurement was 1/16 s. Three pairs of probes were designed to observe the vector electric field [*Maynard et al.*, 1981]. However, one of the three pairs did not deploy, and only two components of the electric field in the meridian plane were observed; the east-west component was not obtained. A Langmuir probe that was also aboard DE 2 provided data on electron temperature, satellite potential, and plasma density with a sampling rate of two samples per second [*Krehbiel et al.*, 1981]. Vector magnetic field data were obtained by a triaxial flux gate magnetometer, with a resolution of ±1.5 nT and

with a sampling rate of 16 vector samples per second [*Farthing et al.*, 1981].

1.2.1 Event on 3 May 1982

Event on 3 May 1982 Typical examples of midlatitude ionospheric electric field fluctuations (MEFs) are shown in Figures 1–6. The upper three panels of Figures 1a and 1b show electron temperature, satellite potential, and plasma density deduced from the DE 2 Langmuir probe observation. The lower two panels show two components of the 1/4 s average electric field data obtained by the vector electric field instrument (VEFI) in the spacecraft coordinate (SPC) system, where the x axis is in the direction of the satellite velocity and the y axis is downward, with the z axis completing a right-handed coordinate system. The z component of the electric field was not observed, as mentioned above.

Figures 1a and 1b show plots for the intervals from 1235:00 to 1237:00 UT and 1248:30 to 1250:30 UT, respectively; in these plots, one division of the horizontal axis is 12 s. Electric field fluctuations are seen between 1235:45 and 1236:35 UT and between 1249:05 and 1250:10 UT. The amplitudes of these fluctuations are a few millivolts per meter. The accuracy of the background electric field intensity is 4 mV/m because of attitude knowledge inaccuracies and sensor asymmetries. Relative accuracies of the variations are of the order of 0.1 mV/m, an order of magnitude less than the fluctuation amplitudes. The potential drops in these fluctuations, which are estimated by integration of the electric field, are of the order of a few hundred volts. The region of these electric field fluctuations extends about 500-km in the latitudinal direction, and the wavelength is typically 10- to 50-km. The plasma density and the electron temperature do not show any significant variations during the electric field fluctuations. This finding is clearly different from the electric field fluctuations inside plasma bubbles observed at low latitudes which are accompanied by severe plasma density depletions

[*Aggson et al.*, 1992] and from the ac electric field fluctuations observed by OGO 6 [*Holtet et al.*, 1977].

When the locations of the electric field fluctuations observed at conjugate points in the northern and southern hemispheres are compared, they are separated about 200-km in altitude and about several degrees in geographic and geomagnetic latitudes, but in invariant latitude the locations (26° to 31°) are almost conjugate in the two hemispheres.

Figures 2a and 2b display the electric field components parallel and perpendicular to the geomagnetic field for the same pass as Figure 1 but for an extended interval, from 1234:00 to 1238:00 UT and from 1247:30 to 1251:00 UT, respectively. The background electric field is subtracted by using a high-pass filter whose cutoff period is 60 s. Here we use the Magsat model [*Langel et al.*, 1980] to calculate the direction of the main geomagnetic field at the satellite.

The angle between the main field and the x-y plane, θ, is plotted in the bottom panels. The angle θ is small enough for us to consider the geomagnetic field parallel to the x-y plane in these time intervals. The electric field is transformed to the components parallel and perpendicular to the geomagnetic field in the x-y plane. The top panels show the perpendicular component of the electric field, in which the positive is radial outward, and the second panels show the parallel component. The angle between the x-z plane and the Magsat model field, φ, is shown in the third panels.

In both intervals the electric field fluctuations are mainly in the perpendicular component, one-sided and radially outward. The parallel component of the electric field ($\mathbf{E}_{\|}$) also fluctuates near 1236:50 in Figure 2a. These fluctuations in $\mathbf{E}_{\|}$ are different from those of the perpendicular component. The fluctuations in $\mathbf{E}_{\|}$ are centered at 1236:50 UT, while those in $\mathbf{E}_{\perp}$ are centered at 1236:10 UT, and the power spectra of the $\mathbf{E}_{\|}$ fluctuations (not shown

here) have a lower spectral index (i.e., larger power in higher frequency) than those of the $\mathbf{E}_\perp$ fluctuations. The axis of one pair of probes was almost parallel to the geomagnetic field line when φ is 45°, and the satellite magnetic wake probably disturbed the electric field [*Bering*, 1983]. The fluctuations in $\mathbf{E}_\parallel$ centered at about 1236:50 UT are likely to have been caused by this circumstance. In fact, fluctuations of the parallel component of the electric field of this type are often observed independently from those in the perpendicular component of $\mathbf{E}$ when one axis of the probes is almost parallel to the geomagnetic field. In the northern hemisphere, in Figure 2b, the same type of $\mathbf{E}_\parallel$ fluctuation is seen when φ is almost 45° at 1248:40 UT.

Fluctuations in the electric field are shown in Figure 3 together with the plasma density over the complete low-latitude pass, in which the electric field data are high-pass filtered with cutoff at 10 s to eliminate the trend. The plasma density data show the Appleton anomaly peak in each hemisphere and show no appreciable variations at midlatitudes. The electric field fluctuations in each hemisphere were poleward of the Appleton anomaly peak, indicating that these fluctuations are outside the influence of the equatorial ionospheric phenomena. Apart from the fluctuations mentioned above, the electric field is stable in this case. During nighttime, plasma bubbles often appear equatorward of the Appleton anomaly peak, and inside these plasma bubbles the electric field fluctuates [*Aggson et al.*, 1992].

In Figure 4 the y component of electric field fluctuations in both hemispheres is plotted as a function of invariant latitude. Some of the large fluctuations indicate gross one-to-one correspondence in the two hemispheres. The amplitudes of the corresponding fluctuations are not exactly the same, but the gradual latitudinal change of the electric field behavior from the lower to higher latitudes is similar in the two hemispheres.

These electric field fluctuations were accompanied by magnetic field fluctuations. The

absolute values of the correlation coefficient between the fluctuations in $\mathbf{E}_x$ and those in $\Delta\mathbf{B}_z$ are over 0.8. In Figures 5a and 5b, magnetic and electric field variations, both band-pass filtered, are shown together in spacecraft coordinates; the band-pass filter used has cutoffs at 3 and 7 s in a period. As is seen in Figure 5a, $-\Delta\mathbf{B}_z$ is highly correlated with $+\mathbf{E}_x$ and $+\mathbf{E}_y$ in the southern hemisphere. Both $-\Delta\mathbf{B}_x$ and $-\Delta\mathbf{B}_y$ also show a correlation with $+\mathbf{E}_x$ and $+\mathbf{E}_y$, as does $-\Delta\mathbf{B}_z$. In the northern hemisphere, $+\Delta\mathbf{B}_z$ has a high correlation with $+\mathbf{E}_x$ and $-\mathbf{E}_y$; on the other hand, both $\Delta\mathbf{B}_x$ and $\Delta\mathbf{B}_y$ have a lower correlation with $\mathbf{E}_x$ and $\mathbf{E}_y$ than does $+\Delta\mathbf{B}_z$. Because amplitudes of the magnetic field fluctuations associated with MEFs are generally near the resolution of the DE 2 magnetic field observation, these magnetic field fluctuations are difficult to identify in the raw data.

The power spectra of the electric field fluctuations in the southern and northern hemispheres are shown in Figures 6a and 6b, respectively. The frequency range is from 3×10^{-2} Hz to 8 Hz, the latter corresponding to the Nyquist frequency. In Figure 6a for the southern hemisphere the power spectrum almost follows a power law of the form $Power \propto f^{-n}$ with a spectral index n of 4.5 for the frequency range 0.2 to 2 Hz. For frequencies higher than 2 Hz the power spectral density, when smoothed, is nearly constant at 1×10^{-4} $[(\mathrm{mV/m})^2/\mathrm{Hz}]$. For the northern hemisphere, shown in Figure 6b, the power spectrum follows a power law with a spectral index of 4.1 for the frequency range from 0.2 to 2 Hz and is constant, on the average, above 2 Hz. On the other hand, the power spectra for other types of ionospheric electric field disturbances observed at high latitudes in association with small-scale Birkeland currents, or those observed in the equatorial region, e.g., in association with plasma bubbles, have spectral indices lower than 3. Thus steep power spectra (i.e., $n > 3$) are characteristic of these midlatitude electric field fluctuations.

1.2.2 Occurrence Rates of MEFs

Occurrence Rates of MEFs Figures 7−11 show the occurrence rates of MEFs during the period from August 1981 to February 1983. The criteria for event selection are as follows. (1) The electric field fluctuation is not accompanied by any significant plasma depletion. (2) The electric field fluctuation is not parallel to the ambient geomagnetic field. (3) The invariant latitude of the location is lower than 50° The first condition serves to distinguish the event from the electric field fluctuation inside a plasma bubble in which the plasma is severely depleted. As mentioned in the discussion of the May 3, 1982, event, when one of the probe axes is parallel to the ambient geomagnetic field, the electric field along that axis shows perturbation by the wake of the spacecraft. To exclude this type of disturbance from analysis, the second condition is applied. The third condition is imposed to distinguish the event from the disturbed electric fields at higher latitudes. The number of observations, i.e., the number of passes in which the electric field data are available in midlatitude, was 3542. Of these, MEFs were observed on 564 passes.

The occurrence rate of MEFs shows a clear dependence on local time, as seen in Figure 7. The occurrence rate is defined as the ratio of the number of events to the number of passes in a local time sector. The occurrence rate is a maximum near local midnight and is very low in daytime. In the 0000−0200 local time sector the electric field fluctuations were observed in 122 cases of 216 traversals.

Figure 8 shows the invariant latitude dependence. This occurrence rate is defined as the ratio of the number of appearances in each invariant latitude range to the total number of events. It has a broad maximum in the range 25° to 40° invariant latitude. A total of 330 events were observed in this invariant latitude range. The electric field fluctuations inside

plasma bubbles are mainly observed at invariant latitudes less than 25°. Therefore these two types of electric field fluctuations are different in the frequency of occurrence with respect to invariant latitude.

The occurrence rate distribution is shown as a local time and invariant latitude contour map in Figure 9a, where the occurrence rate is defined by the percentage ratio of the appearance of MEFs to the number of passes for each square of 1 hour in local time and 10° in invariant latitude. Three peaks are found in the contour map of the occurrence rate shown in Figure 9a instead of one peak in the gross average, shown in Figure 7. The first peak in the 1900−2100 local time sector has a lower occurrence rate than the other two peaks. The second peak is in the 0000−0200 local time sector; this peak is wide in local time and narrow in invariant latitude compared with the third peak in the 0300−0400 local time sector, which is elongated in the direction of invariant latitude.

The occurrence of MEFs does not depend on geomagnetic activity. The maximum and minimum values of the AE index when MEFs were observed are 1161 and 13, respectively. Figures 9b and 9c are contour maps for magnetically disturbed and quiet periods, respectively, i.e., Figure 9b for $AE \geq 200$ nT and Figure 9c for $AE < 200$ nT. MEFs were observed 274 times out of 1724 passes when $AE \geq 200$ nT, and 290 times out of 1818 passes when $AE < 200$ nT. In Figures 9b and 9c, three peaks of the occurrence rate are seen as in Figure 9a. The occurrence rates are very similar for both AE conditions, though the second peak near midnight is slightly shifted toward later local time and higher invariant latitude for the quiet condition.

The geographical distribution of the occurrence rate of MEFs is shown in Figure 10. Contours are drawn based on the average occurrence rates calculated for meshes of 10° in geographic latitude and 20° in geographic longitude. The solid curve near the geographic

equator shows the dip equator. MEFs appear on both sides of the dip equator at nearly all longitudes.

The geographical distribution of the occurrence of MEFs is clearly different from that of plasma bubbles. *Watanabe and Oya* [1986] reported the geographical distribution of the occurrence of plasma bubbles during the period from February 1981 to June 1982, using the data obtained by the Hinotori satellite. This period overlaps the period of the DE 2 observation of MEFs from August 1981 to February 1983. Though the occurrence of plasma bubbles has a maximum between 60°W and 60°E in geographic longitude and between 20°S and 20°N in dip latitude, the occurrence of MEFs does not have any significant maximum in longitude. Furthermore, the region of occurrence of MEFs is poleward of that for plasma bubbles. Therefore MEFs do not seem to be directly related to plasma bubbles.

Figure 11 shows the altitude distribution of the percentage occurrence rate of MEFs. The percentages were calculated by taking the ratio of the number of occurrences to the number of passes for each altitude range. It has a maximum at 600- to 700-km. The altitude of the DE 2 orbit was mainly 300- to 400-km in midlatitude, and the frequency of observation in the 300- to 400-km altitude range was 10 times that in the 800- to 900-km range. It is noted that the apparent peak at 600- to 700-km altitude may be due to the circumstance that the passes in this altitude range occurred nearer midnight than those in the other local time sectors. Thus we do not have enough distribution of observation to discuss the altitude dependence of the occurrence rate in detail. It is only stated that between 250-km and 900-km altitudes the occurrence of MEFs is not restricted to any specific altitude range.

As for the seasonal variation, the DE 2 orbit covered all local time sectors in about 6 months. That is, the local time of the orbital plane and season are not independent. Therefore it is difficult to distinguish seasonal dependence from local time dependence. However,

we can say at least that the occurrence rate is larger at night than in day throughout the year.

MEFs are sometimes accompanied by magnetic field fluctuations, as shown in Figures 5a and 5b. Though the resolution of the magnetic field observation of DE 2 is ± 1.5 nT [*Farthing et al.*, 1981], which is comparable to the amplitude of such magnetic field fluctuations, the absolute value of the correlation coefficient between $\mathbf{E}_x$ and $\Delta\mathbf{B}_z$ is over 0.5 in 45% of the observed MEF cases. In almost one half of such cases, $\mathbf{E}_x$ and $\Delta\mathbf{B}_z$ are anticorrelated, which means that the Poynting vector directs upward, i.e., that the energy flow is upward.

1.3 Discussion

1.3.1 Conjugate Occurrence of MEF

MEFs are often observed simultaneously at magnetically conjugate points. Because the DE 2 orbital plane is a geographic meridian plane, the locations at which DE 2 crosses a given invariant latitude in the northern and southern hemispheres differ in general by several degrees in geomagnetic longitude. When the difference in geomagnetic longitude is within 10°, about 60% of the observed MEFs are accompanied by a counterpart at the conjugate point. As the difference in geomagnetic longitude increases, the number of conjugate appearances decreases. But in some cases, MEFs are observed at conjugate points which are separated by as much as 18° in geomagnetic longitude. From the above result the flux tube that contains an MEF seems to have a longitudinal extent of several degrees. The amplitudes of MEFs in the two hemispheres are often different. This difference may come from their longitudinal structures and/or from their temporal variations.

From the data set used in this paper it is not possible to deduce temporal variations of

MEFs. The conjugate appearance of the fluctuations as observed by DE 2 indicates that these fluctuations often remain for more than 15 min. Sometimes MEFs were observed on successive orbits at different longitudes, but in general, the fluctuations are not observed on successive orbits. This does not necessarily mean that these fluctuations disappear in one orbital period, i.e., about 90 min, because the orbit shifts by 22.5° in longitude in one orbital period.

In the case shown in Figure 1, the altitude at which the fluctuation occurred was about 400-km in the southern hemisphere and 600-km in the northern hemisphere. The similarity of the fluctuations in spite of the 200-km difference in altitude suggests that an MEF is mapped along the geomagnetic field. The extent of the flux tube that contains an MEF is considered to be several hundred kilometers in the direction perpendicular to the geomagnetic field in the meridional plane and several degrees, i.e., several hundred kilometers, in the longitudinal direction.

MEFs are sometimes accompanied by magnetic field fluctuations. The electric and magnetic field fluctuations are highly correlated, as shown in the examples of Figures 5a and 5b. The high correlations between electric and magnetic field perturbations observed in the high latitude ionosphere have been interpreted in terms of two models. In one model, perturbations are interpreted as being static structures in field-aligned currents [*Sugiura*, 1984], and in the other they are interpreted as Alfvén waves [*Gurnett et al.*, 1984]. In the static model the ratio between the orthogonal magnetic and electric field components ($\Delta \mathbf{B}_z/\mu_0 \mathbf{E}_x$) represents the height-integrated Pedersen conductivity (Σ_P). In the Alfvén wave model the ratio $\mathbf{E}_x/\Delta \mathbf{B}_z$ gives the Alfvén wave velocity ($\mathbf{V}_A$). However, because the resolution of the magnetic field observation is comparable to the amplitudes of the magnetic field fluctuations associated with MEFs, and because $\mu_0 \Sigma_P$ is comparable to the inverse of $\mathbf{V}_A$ in the

nighttime midlatitude ionosphere, it is difficult to determine which of the two models is more appropriate for MEFs solely on the basis of the ratio of the electric and magnetic field fluctuations.

Nevertheless, the large variations in MEFs are often similar in the two hemispheres in spite of the time differences, as in the examples shown in Figure 4. This feature favors the static model. Another feature that favors the static model over the Alfvén wave model is that the electric field fluctuation is one-sided, that is, the direction of the electric field in the fluctuations is perpendicular to the geomagnetic field, as in the event shown in Figures 2a and 2b. Thus we interpret that the MEFs are caused by field-aligned currents having static structures.

In the event shown in Figures 5a and 5b the southward and upward components of the electric field fluctuations ($-\mathbf{E}_x$ and $-\mathbf{E}_y$) are highly correlated with the westward component of the magnetic field fluctuations ($\Delta\mathbf{B}_z$) in the southern hemisphere. Thus the Poynting flux is downward along the geomagnetic field. In the northern hemisphere the northward and upward components of the electric field fluctuations ($\mathbf{E}_x$ and $-\mathbf{E}_y$) are highly correlated with westward components of the magnetic field fluctuations ($\Delta\mathbf{B}_z$). Thus the Poynting flux is upward along the geomagnetic field. Therefore the energy flows from the northern hemisphere to the southern hemisphere along the geomagnetic field. It is clearly seen in Figures 2a and 2b that the direction of the electric field of MEFs is one-sided and perpendicular to the geomagnetic field. Considering the direction of the electric field of MEFs and the correlation between the electric and magnetic field fluctuations, a schematic current system, and the electric and magnetic fields in meridian plane, are illustrated in Figure 12. MEFs are interpreted as constituting series of this type of transhemispheric current systems.

I_S and I_N represent the ionospheres in the southern and northern hemispheres, respec-

tively. The shaded and crosshatched areas represent the field-aligned current sheets infinite in the longitudinal direction. In the shaded area the field-aligned current flows from the northern to the southern hemisphere, and in the crosshatched area the field-aligned current flows in the opposite direction. In the ionospheres the closure currents flow perpendicular to the geomagnetic field because of the finite Pedersen conductivities. The source region is in the northern ionosphere in this case. The current density estimated from the magnetic field fluctuations is approximately $0.2-0.3\ \mu\mathrm{A/m}^2$ Assuming the MEFs to extend more than several hundred kilometers in longitude and latitude, the total current can be more than 10^4 A.

The mechanism of the charge separation in the source region is not clear. Some ionospheric instabilities at midlatitude, such as the Perkins instability [*Perkins*, 1973], could play an important role. To clarify the generation process of MEFs, simultaneous observations by satellite and ground-based radar and numerical modelings of midlatitude ionosphere which include the field-aligned current are necessary.

We cannot determine the orientation of the field-aligned current sheets which cause the MEFs, since the z component of the electric field was not observed. High correlation between $\mathbf{E}_x$ and $\mathbf{E}_y$ and $\Delta\mathbf{B}_z$ indicates that the current sheets are elongated in the east-west direction. But the correlation with the electric field fluctuations and $\Delta\mathbf{B}_x$ and $\Delta\mathbf{B}_y$ indicated that these current sheets are not exactly parallel to the east-west direction. The resolution of the magnetic field observation of DE 2 is comparable to the amplitude of such magnetic field fluctuation, so that detailed study of the orientation of the field-aligned current sheets by DE 2 observation is difficult.

The directions of the Poynting fluxes of the MEFs observed at the magnetically conjugate points in the northern and southern hemispheres suggest that the energy flows up from one

hemisphere and down to the other hemisphere. The direction of the energy flux is different for each event, and it can alter even within 1 day. For instance, on August 27, 1982, 3 hours after the observation of an MEF in which the energy flow was from the northern to the southern hemisphere (1442 UT), another MEF was observed in which the energy flow was from the southern to the northern hemisphere (1747 UT). The lowest altitude at which DE 2 observed an upward Poynting flux was 245-km. Thus the source region can be lower than 245-km in altitude.

1.3.2 Interhemispheric Transmission Efficiency of MEF

When the parallel conductivity is infinite, the magnetic field lines are equipotential. However, because of the finite ionospheric conductivity, small-scale field-aligned currents are partially short-circuited, and only large-scale structures are mapped down to the lowest levels of the ionosphere. We estimate approximately the efficiency of transmission of an impressed electric field along dipole field lines. Similar calculations have been made by *Reid* [1965], *Park* [1976, 1979] and *Forget et al.,* [1991].

The basic equation solved is $\nabla \cdot \mathbf{J} = 0$ in the ionosphere, where $\mathbf{J}$ is the electric current density, which can be expressed as $\mathbf{J} = \sigma_D \mathbf{E}_{\|} + \sigma_P \mathbf{E}_{\perp} + \sigma_H \mathbf{b} \times \mathbf{E}_{\perp}$. Here σ_D, σ_P, and σ_H are parallel, Pedersen, and Hall conductivities, respectively, and $\mathbf{E}_{\|}$ and $\mathbf{E}_{\perp}$ are the electric field intensities parallel and perpendicular to the ambient magnetic field, respectively; $\mathbf{b}$ is the unit vector in the direction of the magnetic field.

The transmission efficiency is considered to be mainly affected by the conductivity in low altitude and the length of the field line, and not by the curvature of the field line. Therefore we assume that the geomagnetic field is vertical with the northern and southern ionospheres at both ends. By assuming longitudinal uniformity the Fourier-transformed electrostatic

potential Ψ_k satisfies the following equation:

$$\frac{d^2\Psi_k}{ds^2} + \frac{dln\sigma_D}{ds}\frac{d\Psi_k}{ds} - k^2(s)\frac{\sigma_P}{\sigma_D}\Psi_k = 0 \quad (1)$$

In this equation the s direction is parallel to the magnetic field, and $k(s)$ is the wave number perpendicular to the magnetic field. In order to include the effect of the expansion of flux tube, $k(s)$ is altered with altitude.

The normalized boundary conditions are $\Psi_k = 1$ V at the source region and $\Psi_k = 0$ V at the ground. Conductivities below 1000-km altitude are taken from the IRI-90 model [*Bilitza*, 1990] for May and for 0000 local time with sunspot number 65. Above 1000-km, parallel conductivity is assumed to be constant, and Pedersen conductivity is assumed to decrease with a scale height of 300-km. Equation (1) for the Fourier transformed potential is solved numerically.

Figure 13 shows the results of this calculation. In this model calculation the geomagnetic field line along which the field-aligned current flows corresponds to the dipole geomagnetic field line at 25° invariant latitude, and the source region is assumed to be located at a 200-km altitude.

We considered that the source region would be lower than 250-km altitude because the lowest altitude where DE 2 observed the upward Poynting flux was 245-km, and it would not be in the E region because the electric field is short-circuited in the E region and not to be transmitted to the opposite hemisphere.

The horizontal axis shows the electrostatic potential, and the vertical axis represents altitude on the left-hand side and latitude on the right-hand side. Curves are drawn for the wavelengths indicated. Figure 13 shows that structures larger than about 8-km in size are

not much attenuated throughout the field line. However, structures smaller than this size are heavily attenuated during the transmission along the field line to the opposite hemisphere. Within the ionosphere of the source region, structures of sizes less than about 2-km are significantly attenuated. Similar calculations for the cases of different source locations show that structures typically larger than 8-km in size are transmitted along the field line with no significant attenuation, and structures typically smaller than 8-km are severely attenuated as the distance from the source location increases.

In the DE 2 observation a spatial structure of wavelength larger than 8-km is equivalent to a fluctuation of frequency lower than about 1 Hz as observed by the spacecraft. Therefore it is quite reasonable that the power spectra of the electric field fluctuations of frequencies lower than 1 Hz are very similar in the southern and northern hemispheres, as in the examples shown in Figures 6a and 6b. The observed steep power spectrum with a spectral index of 3.5−4.5 for frequencies below 1 Hz represents the power spectrum in the source region for that frequency range. The power spectrum of the observed electric field fluctuations in frequencies higher than 1 Hz would be attenuated with increasing distance from the source region to the observation point. However, the power in the electric field fluctuations in frequencies higher than 1 Hz is generally below the noise level, i.e., the sensitivity of observation at midlatitudes. Thus we cannot identify the location of the source region from the power spectra of the MEFs observed by DE 2.

1.3.3 Relationship to Other Ionospheric Phenomena

Electric field fluctuations such as those observed by DE 2 could produce perturbations in the midlatitude ionosphere. The possible relations between MEFs and other ionospheric phenomena are discussed below.

The averaged direction, i.e., the dc component, of MEFs is upward (i.e., radially outward and perpendicular to the ambient magnetic field) in 65% of the observed MEFs. Unfortunately, the DE 2 satellite could observe only the meridional component of the electric fields. Therefore it is not certain whether or not MEFs have an east-west component. We tentatively assume that the direction of the electric field fluctuation is only meridional. Since the direction of the averaged electric field is mostly upward if we ignore the largescale trend, and the $\mathbf{E}\times\mathbf{B}$ drift is westward, its speed is about 100 m/s. This drift velocity is comparable with the drift velocity of the plasma containing F region field-aligned irregularities (FAI) observed by the MU radar [*Fukao and Kelley,* 1991]. These ionospheric irregularities appear in the midlatitude nighttime F region and are supposed to be caused by the Perkins instability [*Kelley and Fukao,* 1991]. The north-south component of MEFs could cause the Perkins instability, as in the mechanism originally discussed by *Perkins* [1973]. While F region FAIs are rarely observed near solar maximum, MEFs were observed near a solar maximum. If MEFs also exist in solar minimum, they could drive FAIs.

The relation between MEFs and spread-F is not clear. For several cases we examined the ionograms taken approximately under the location where MEFs were observed in the ionosphere by DE 2. However, no clear relationship was found between MEFs and spread-F. A more detailed and careful examination is necessary to obtain conclusive results on this relationship.

ISIS 1 observed plasma depletions in the nighttime equatorial region above 2000-km altitude [*Burke et al.,* 1979]. These plasma depletions were considered as plasma bubbles which drifted upward. Their scale lengths of several hundred kilometers are much larger than the scale lengths of plasma bubbles at bottomside altitudes. They only appear in the postmidnight time sector. These plasma depletions have a similarity with the MEFs

observed by DE 2 with respect to their locations and scale lengths. But as shown in Figure 9a, MEFs occur in $20°-50°$ invariant latitude in almost every local time sector from 1800 to 0500 hours. This occurrence cannot be explained by upward drifting plasma bubbles.

During a magnetically disturbed period the magnetospheric electric field is supposed to penetrate into lower latitudes and to cause spread-F and scintillations [*Gonzales et al.*, 1983]. We find that the occurrence of the MEFs observed by DE 2 is not restricted by geomagnetic activity expressed, for instance, by the Dst or AE index. Therefore we believe that MEFs are not directly related to high latitude ionospheric electric field disturbances.

1.4 Summary

The DE 2 satellite observed midlatitude ionospheric electric field fluctuations (MEFs) in the topside midlatitude ionosphere. Characteristics of the MEFs are as follows:

1. The region in which the electric field fluctuates extends several hundred kilometers in the north-south direction, and the wavelengths of these fluctuations are several tens of kilometers.

2. MEFs have amplitudes of a few millivolts per meter and are perpendicular to the geomagnetic field. The average electric fields in them are mainly upward.

3. MEFs often appear simultaneously at magnetically conjugate points in the northern and southern hemispheres.

4. MEFs mainly appear in nighttime, their occurrence frequency having a clear postmidnight peak.

5. MEFs are not accompanied by any significant plasma density decreases or electron temperature fluctuations.

6. In the frequency range about 0.1 to 1 Hz, the power spectra follow a power law with a spectral index of about 3.5. The power spectra are steeper than those for other ionospheric

electric field disturbances at high latitudes or in the equatorial region.

7. MEFs are sometimes accompanied by magnetic field fluctuations near the sensitivity limit of the magnetometer.

An MEF is interpreted as electric field structures in a trans-hemispheric field-aligned current. The magnitude of the current is of the order of 0.2 to 0.3 $\mu A/m^2$, and the Poynting flux is from one hemisphere to the other. The direction may vary from day to day or even within one day. The source region of the field-aligned current is in the lower ionosphere, though the location of the seed mechanism could be high above the equatorial ionosphere. Further evidence is required to identify the source mechanism. MEFs are not directly related to plasma bubbles or high latitude activity. While there may be a relationship to F region field-aligned irregularities and spread-F, the relationship is not clear.

Chapter 2.

Conjugate Observations of the Mid-latitude Electric Field Fluctuations with the MU Radar and the Freja Satellite

2.1 Introduction

As reported in Chapter 1, the mid-latitude electric field fluctuations (MEFs) were observed by the DE-2 satellite in the nighttime mid-latitude ionosphere. Their wave length is several tens kilometers and they extend several hundreds kilometers in the latitudinal direction. These fluctuations are often observed simultaneously at the magnetically conjugate points. Several events are accompanied by magnetic field fluctuations. The analysis of their Poynting flux clarifies that they are generated in a nighttime ionosphere and transmitted to the magnetically conjugate point along the geomagnetic field line. Their occurrence rate is more than 15 % in invariant latitudes from 25 to 40 degrees. A clear occurrence maximum is in the post midnight local time sector, and low occurrence in the daytime. The amplitude of the MEFs is several milli-volts per meter, which is comparable with the background

ionospheric electric field. Such intense amplitude suggests that some kind of ionospheric instabilities would play an important role in the evolution of the MEFs.

The relation of this type of electric field fluctuations with the other ionospheric phenomena has not been clarified. One of the purposes of this paper is to clarify the relation between the MEFs and the other ionospheric phenomena which are observed by ground-based observation techniques.

Several types of irregularities in the nighttime mid-latitude ionosphere have been observed with various techniques. The Arecibo IS radar observed well-defined bands of the F-region ionosphere in the nighttime, in which the F-region is alternately high and low with more than 30 km height difference [Behnke, 1979]. The horizontal scale of such bands is several tens km. These bands travel toward south-west with up to 60 m/s drift velocity.

Another interesting mid-latitude F region phenomena was reported by Fukao et al. [1991]. They observed intense back scatter echoes of 46.5 MHz radar wave from field-aligned irregularities. Doppler velocity deduced from these echoes indicates that intense polarization field is generated inside of these irregularities.

The Perkins instability is considered to play an important role in the evolution of these nighttime F region phenomena [Behnke, 1979; Kelley and Fukao, 1991]. The Perkins instability is initially studied as the generation process of the nighttime spread F phenomenon [Perkins, 1973]. Perkins found that the nighttime F region ionosphere supported by the electromagnetic force is unstable if a north-south electric field component exists. The modulation of the ionospheric layer is enhanced in this instability.

The banded structures of the nocturnal F layer over Arecibo, which has 100 km horizontal scale, are interpreted to be caused by the Perkins instability [Behnke, 1979].

$\mathbf{E} \times \mathbf{B}$ instability is another large-scale instability process which is applied in the mid-

latitude ionosphere. The vertical gradient of the plasma density, however, cannot be unstable at mid-latitude, because of the electrical coupling between the bottomside and the topside of ionosphere by the geomagnetic field line. The horizontal gradient of the field line integrated conductivity could be unstable through the $\mathbf{E} \times \mathbf{B}$ instability.

Basu et al. [1981] interpreted that the kilometer scale ionospheric perturbations above Arecibo is caused by the $\mathbf{E} \times \mathbf{B}$ type instability, when the horizontal gradient of the height integrated conductivity is large enough, because of the midnight collapse, a rapid descend of the ionosphere at midnight.

Muldrew [1980] studied MF radio wave ducts with topside sounder satellite. Its distribution of the occurrence rate, which is shown in his Figure 13, is very similar with that of the MEFs observed by DE-2, in the nighttime mid-latitude from L=1.2 to 2. The occurrence distribution of the ducts in the other local time and latitude is interpreted to be related with plasma bubble and asymmetry of the Sq current. There is, however, no discussion about the distribution in the region L=1.2 to 2 in his paper.

The MU radar and the Freja satellite conjugate observations have been carried out to clarify the background ionospheric condition necessary for the generation of the MEFs, and the relation to the other ionospheric irregularities.

2.2 Observation

The electric field is observed by the Freja satellite above 1000 km altitude, and the ionospheric parameters, such as $F2$ layer height and $F2$ peak electron density, are obtained by the MU radar and the ionosonde near its foot point of the geomagnetic field line.

The Freja satellite was launched October 6, 1992, and flew in an orbit with a perigee of 600 km, an apogee of 1750 km, and 63 degrees inclination. Two components of the electric

field in its spin plane were observed with a double probe instrument [Lundin et al., 1994].

The MU radar located at Shigaraki, Japan (34.85°N, 136.10°E in the geographical coordinate, and 24.91°N in the geomagnetic latitude), is an active phased-array radar at 46.5 MHz, and steerable to multiple directions in every inter pulse period, about ten milli seconds [Fukao et al., 1985]. The multi-directional observation would be suitable to detect the background ionospheric conditions of the electric field fluctuations.

The MU radar and the Freja satellite conjugate observations had been conducted in five time periods, which are in May 1993, in April, May, October and November 1994, and in June 1995, total 14 nights.

2.2.1 May 18, 1993

At 14:08 UT (23:08 Japan Standard Time [JST]) on May 18, 1993, Freja flew across the conjugate region of the MU radar at 1300 km altitude. The two electric field components, E1 and E2, observed by Freja from 14:03:20 to 14:13:20 UT are shown in Figure 14. The E1 component is along the projection of the geomagnetic field line onto the Freja spin plane, and the E2 component is perpendicular to the geomagnetic field, its positive towards dusk. The angle between the Freja spin axis and the geomagnetic field line, M-SCZ, was around 30 degrees during this observation period, and therefore the E1 component was rather perpendicular to the geomagnetic field than parallel.

The large scale trend seen in both electric field components is attributed to the satellite attitude ambiguity since Freja was in the eclipse of the earth during this time period. The electric field fluctuations are seen from 14:07:40 to 14:12:00 UT in the E1 component. Large scale trends of both components during these fluctuations are interpolated from the field of each two ends, and represented as broken lines in Figure 14. The amplitude of these electric

field fluctuations is up to 10 mV/m, though it could have some ambiguity caused by the satellite attitude error mentioned above. Subtracting the large scale trend, the direction of the electric field fluctuation is always E1 positive (downward) and E2 negative (dawnward). The location where the electric field fluctuations were observed is from 28 to 31 degrees in the corrected geomagnetic latitude. The one-side feature, the location in latitude, and the spatial scale of the electric field fluctuations are similar to those of the electric field fluctuations observed by the DE-2 satellite, despite of the altitude difference between DE-2 and Freja (*see Chapter 1.*).

The MU radar is located at the foot point of the field line which crosses the region of these electric field fluctuations. The locations of the MU radar site and the Freja trajectory which is mapped along the geomagnetic field line to the ionospheric height, 325 km altitude, are shown in the Figure 15. Solid line with an arrow head represents the Freja trajectory projected to 325 km altitude. The electric field fluctuations of the E1 component are superimposed to the trajectory. The location of the MU radar is represented by a solid circle at the middle. The large open circle around the MU radar represents the MU radar observation region at 325 km altitude when the radar beam zenith angle is 20 degrees.

In the night of May 18, 1993, the MU radar was operated in the standard ionospheric observation mode, in which the radar beam is directed to four directions, north, east, south and west with 20 degrees zenith angle. The electron density profiles of the four directions are obtained in the first quarter of every hour with high range resolution, 10 km. In the remainder 45 minutes of every hour, the range resolution is low, 75 km, but the line-of-sight plasma drift velocities of four beams are obtained. The plasma drift vector can be derived from these four line-of-sight drift velocities [Oliver et al., 1993]. The sampling rate in these two modes is 32 μ second, so the sampling interval is 4.5 km in altitude.

Figure 16 (a) and (b) display the *F*-region peak height obtained by the MU radar electron density observation. The peak heights are obtained in every 15 minutes for each hour. The observation mode is, however, changed between the high range resolution mode and the low resolution mode, as mentioned above. Therefore, the peak heights obtained in the low range resolution mode are calibrated referring those obtained in the high range resolution mode, and the data are smoothed with low pass filter. Figure 16 (a) shows the peak height detected by the northward and the southward directed beams. The regions where these two beams observed are separated by 235 km horizontally at 325 km altitude. The observation of the northern ionosphere shows that the *F*-2 layer gradually ascend after 22:00 JST from 285 km to 325 km altitude, and then descend rapidly about 30 km within 30 minutes around 23:00 JST (14:00 UT).

Similar ascending and descending of the ionosphere are seen in the southern ionosphere with about 30 minutes delay time to the northward ionosphere. The phase difference of the vertical movement of ionosphere between the northward and southward directions indicates that these *F*-2 peak movement would be caused by a traveling ionospheric disturbance [TID]. Figure 16 (b) is the same figure as Figure 16 (a) except for the beam directions are eastward and westward. The *F*-2 peak height changes are also seen around 23:00 JST. The phase of the eastward ionosphere is about 30 minutes ahead of that of the westward ionosphere. The traveling velocity of this TID estimated by these phase differences between the four beam directions is 110 m/s to south-west.

To ensure this TID motion, the ionograms at two sites, Shigaraki (the MU radar site) and Kokubunji (35.42°N G-lat., 139.29° G-lon.), are studied. The location of these sites are displayed in Figure 15 as solid circles. The apparent heights of the *F*-2 region echo at 5 MHz are shown in Figure 16 (c). The sampling interval is 15 minutes, and the data

are smoothed, as the MU radar data. The solid curve is the apparent height of the F-2 region at Shigaraki, and the dotted curve is that at Kokubunji. The solid circles and the open rectangles correspond to the time when the range type spread-F echoes are seen on the ionograms of Shigaraki and Kokubunji, respectively. At Kokubunji, F-region starts to rise before 22:00 JST and 30 minutes later, it begins to fall. During this F-region movement, the spread-F echoes are seen. At Shigaraki, the rise and fall can be seen around 23:00 JST. This excursion are also accompanied by spread-F echoes. The phase difference of the TID between Kokubunji and Shigaraki is about 50 minutes, and the traveling velocity estimated with this phase difference is 92 m/s to south-west, almost consistent with that estimated by the MU radar observation, which is 110 m/s to south-west.

The location of the TID peak at 14:10 UT (23:10 JST) inferred by the MU radar observation is also shown as the hatched area in Figure 15. An arrow below the area of the TID peak represents the direction of the TID motion. We can see that the electric field fluctuations were observed around the peak and the backside of the TID.

2.2.2 Occurrence Rate and Locations

The Freja and the MU radar conjugate observations had been conducted for 14 nights from 1993 to 1995. The trajectories of Freja where the electric field fluctuations were observed are displayed on a map around the MU radar in Figure 17. The solid lines represent the Freja trajectories mapped down to the ionospheric altitude (300 km), in the northern hemisphere along the geomagnetic field line. The dates of the observation are displayed beside of them. The Freja's orbits were above 1200 km altitude in these observations. Kinks of the curves for April 27, 1994 and May 9, 1994 correspond to the equatorial crossing of the orbit.

The electric field fluctuations were observed in five Freja passes out of 14 passes. This

occurrence probability is almost similar to that of the MEFs observed by DE-2, which is 36.8 % in 20−04 local time sector as shown in Figure 7.

Unfortunately, the observation on May 18 in 1993 is the only case where the observation was made on the exactly same field line by Freja and the MU radar. The Freja trajectories of the other observations did not cross the MU radar observing ionosphere. In the following section, the observations in July, 1995 are studied to compare the background ionospheric conditions between the nights with the electric field fluctuations and those without the fluctuations, using the MU radar 8 beam observation.

2.2.3 June 5-8, 1993

The Freja and the MU radar conjugate observations had been conducted in four consecutive nights from June 5 to 8, 1995. The MU radar was operated in a different observation mode from that used in the observation on May 18, 1993. The radar observed eight directions, north, east, south and west with two different zenith angles, 10 and 30 degrees. Electron density profiles are obtained in these eight directions every 5 minutes with 4.8 km range sampling interval.

On June 8, 1995, the conjunction time between Freja and the MU radar was around 00:40 JST (15:40 UT). The MU radar was operated from 21:13 to 23:30 JST (12:13 $\sim$ 14:30 UT), and from 00:23 to 03:17 JST (15:23 $\sim$ 18:17 UT). Unfortunately, an instrumental trouble interrupted the observation between 23:30 and 00:23 JST.

The electric field observation by Freja on June 8 is shown in Figure 18. The electric field fluctuations are seen from 15:36 to 15:45 UT in both, E1 and E2 electric field components. Their amplitude is about 4 mV/m, and the one-side feature are not clear in this case. The footpoint of these electric field fluctuations projected on 300 km altitude are plotted in Figure

17, labeled as June 8, 1995.

The range-time-intensity (RTI) plots of this night is displayed in Figure 19. The RTI plot obtained by the beam 1, directed northward with 10 degrees zenith angle, is shown. The vertical axis indicates the altitude from 300 km to 600 km. The blank region at the middle of this panel is due to the lack of the observation data as mentioned before. The radar echo intensity profiles are obtained at every 5 minutes with 15 minutes data integration centered at the time. Some coherent echoes of the side robes are seen in this RTI plots. High intensity echo below 325 km altitude from 21:40 to 23:30 JST is not the incoherent echo from free electron, but coherent echo from field-aligned irregularities (FAIs) in the sporadic-E layer. This type of FAIs have been eagerly studied with the MU radar coherent mode observation [Yamamoto et al., 1994. Tsunoda et al. 1994]. The echo from F-region ionosphere is mainly seen from 350 km to 400 km altitude. The F-region peak location is hard to be distinguished from this plot, but the ionosphere movement could be seen from iso-intensity contour of the topside F-region. There is a descending after 22:00 JST, which followed by a rise back to the original altitude at 23:10. During the interruption, the echo intensity gets much weaker. After 02:00 JST, the ionosphere descends and echo intensity decreases gradually.

The F-region movements inferred from the RTI plots obtained by the other seven beams show different movement each other. Their large scale behaviors are similar, but there are phase and altitude differences. To show the spatial non-uniformity, the F-region peak heights obtained by the MU radar are plotted in Figure 20. F-region peak heights are obtained by fitting an analytical function to the observed profile to reduce the error. The analytical function used here is as same as used in *Reddy et al.*, [1991], which is based on the Chapman layer theory. Beam 4, which is directed westward with 10 degrees zenith angle, is not included this analysis, because the side robe echo in this beam was too intense to fit the function. The

solid line is average peak altitude of the seven radar beams. The error bar at each points are mean value of the deviations of the seven peaks from the average peak altitude. The difference of peak altitudes between the beams is large throughout the observation.

To find out the necessary conditions for the generation of the MEFs, we examined the ionospheric condition observed by the MU radar on June 6, 1995, when no electric field fluctuations were observed by Freja.

On June 6, 1995, the conjunction time between Freja and the MU radar was around 01:30 JST (16:30 UT). The MU radar was operated from 21:09 to 03:15 JST (12:09 $\sim$ 18:15 UT). The RTI plot of the MU radar beam 1 observation is displayed in figure 21. The observation started at 21:09 JST. Until the midnight, the echo intensity, which is proportional to the electron density, keeps decreasing, the rate of decrease is higher at lower altitude because of the high recombination rate in lower altitude. After midnight, the F-region gradually descend to lower altitude than 300 km altitude. The RTI plots of the eight beams are very similar each other.

The F-region peak height plot, obtained in the same way as Figure 20, is shown in Figure 22. The difference from the average peak altitude is much smaller than that on June 8, the night with the electric field fluctuations. The radar sampling interval is about 4.5 km in altitude, therefore these difference of peak altitudes are negligible. Post-midnight descending is also observed as on June 8, but the peak difference between the eight observation beams are small. Every eight beams which observed the ionosphere in a 200km radius circle at 350 km altitude, observed similar F-region behavior. No large scale structure was seen in this night, when no electric field fluctuation was observed.

2.3 Discussion

The satellite and ground-based radar observation clarified that the mid-latitude electric field fluctuations (MEFs) have close relationship with large scale ionospheric structures, such as TIDs.

Mid-latitude TIDs are often classified into two types [Georges, 1968]. That is, the large scale TIDs (LSTIDs), which are generated in the auroral electrojet during the magnetically disturbed periods, and medium scale TIDs (MSTIDs) which have their source in the lower atmosphere. The occurrence probability of MEFs does not have significant dependence on the geomagnetic activity as shown in Figure 9 (a), (b) and (c). thus, both of LSTIDs and MSTIDs could stimulate MEFs.

The conjugate observations on May 18, 1993 revealed that these fluctuations are embedded around the peak and backside of a TID. It is supposed that small scale (several tens km) modulations, MEFs, which are inside a large scale (several hundreds km) modulation, TID, cause polarization field which is transmitted along the geomagnetic field line. The intensity of the electric field fluctuations are several milli-volts per meter, which is comparable to the background ionospheric electric field [Oliver et al., 1993]. To create such intense polarization electric field, some kind of ionospheric instabilities would play an important role in its evolution.

There are two types of instabilities proposed for the mid-latitude ionospheric irregularities whose scale size is more than one kilometer. One of them is the $\mathbf{E} \times \mathbf{B}$ gradient drift instability [Basu et al., 1981; Maruyama 1990], and the other is the Perkins instability [Perkins, 1973, Behnke, 1979; Kelley and Fukao, 1991].

In the following section, the growth rate of these mid-latitude ionospheric instabilities

are discussed with the MEF observational results.

2.3.1 The Growth Rate of Mid-latitude Irregularities

The mid-latitude ionosphere is equipotential along the geomagnetic field line when the electric potential is more than kilometer scale size as shown in Figure 13. It is comprehensive to use the field-line integrated parameters for describing the mid-latitude ionospheric phenomena. A set of equations for the field-line integrated Pedersen conductivity and the electric potential was derived from the continuity and momentum equations of ions and from the electric current continuity equation by *Perkins* [1973]. The effect of the opposite hemisphere is not included in this discussion though it could be important for the evolution of the MEFs. The momentum equation of the field-line integrated Pedersen conductivity, which is similar to the Perkins' equation (15), but including neutral wind explicitly, is as follows, (*see Appendix 1*):

$$\frac{\partial \Sigma}{\partial t} + \nabla_\perp \cdot \{\Sigma(\frac{\mathbf{E}_\perp \times \mathbf{B}}{B^2} + \frac{m\mathbf{g} \times \mathbf{B}}{eB^2})\} = -\Sigma \frac{E_{east}}{B}\frac{cosD}{H} + \Sigma U_\parallel \frac{sinD}{H} + \frac{Nmg_\parallel}{B^2}\frac{sinD}{H} \qquad (2)$$

Σ is the field-line integrated Pedersen conductivity, m and $\mathbf{g}$ are mean molecular mass, and the gravity acceleration, respectively. D and H are the dip angle and the scale height, and the symbols $\parallel and\ \perp$ denote parallel and northward perpendicular components to the geomagnetic field, respectively.

Following equation is used as the electric current continuity equation:

$$\nabla_\perp \cdot \{\Sigma(\mathbf{E}_\perp + \mathbf{U}_\perp \times \mathbf{B})\} = 0 \qquad (3)$$

Field aligned currents are ignored in this discussion. Combining equations (2) and (3), the growth rate is derived in the frame moving in the velocity of $\frac{\mathbf{E}_\perp \times \mathbf{B}}{B^2} + \frac{m\mathbf{g}_\perp \times \mathbf{B}}{eB^2}$, (*see Appendix 2*).

$$\gamma = \frac{E_0^*}{B}\frac{cosD}{H}sin\alpha sin(\theta^* - \alpha) + \frac{E_0^*}{B}\frac{\nabla_\perp \Sigma_0}{\Sigma_0}cos(\theta^* - \alpha)sin(\beta - \alpha) \quad (4)$$

E^* is the effective electric field, $\mathbf{E}_0^* = \mathbf{E}_0 + \mathbf{U} \times \mathbf{B}$ and the neutral wind is assumed to be horizontal. The configuration of $\mathbf{E}^*$, conductivity gradient, and wave vector is illustrated in Figure 23 in a plane perpendicular to the geomagnetic field. α, β, and θ^* are the angles of the wave vector, $\nabla\Sigma$ and $\mathbf{E}^*$ from east, respectively.

The first term of the equation (4) comes from the change of the field-line integrated conductivity as the result of the ascent and descent of ionosphere, which is called the Perkins instability. The second term comes from the $\mathbf{E} \times \mathbf{B}$ drift with the initial gradient of the field-line integrated conductivity, which cause $\mathbf{E} \times \mathbf{B}$ gradient drift instability.

The growth rate depends on the direction of the wave vector. The growth rate of the $\mathbf{E} \times \mathbf{B}$ type instability is maximum when $\mathbf{k} || \mathbf{E}^*$, and proportional to $sin(\beta - \theta^*)$. The growth rate of the Perkins instability is positive when the wave vector is between the direction of $\mathbf{E}^*$ and east, and gets lower for the smaller angle between the wave vector and the $\mathbf{E}^*$ or east is smaller. Therefore, the perturbation along the background electric field or along the east-westward are stable, and the growth rate is maximum when $\alpha = \frac{\theta^*}{2}$.

Here, we estimate the growth rate of the mid-latitude ionospheric instabilities using the average ionospheric condition. The ion drift velocities had been observed by the MU radar from September 1986 to January 1991 [Oliver et al., 1993]. The averaged electric field is not intense around the midnight local time sector. The southward component of the electric field is about 0.4 mV/m and the westward component is about 0.4 mV/m at midnight. The electric field observations by the other IS radars at mid-latitude provide similar results [Kelley, 1989]. The meridional component of the neutral wind is also obtained by the MU

radar observations under an assumption that the neutral wind has no vertical component [Oliver et al., 1990]. The horizontal southward neutral wind is about 50 m/s at midnight, which is equivalent to the eastward electric field with 2.0 mV/m. Using these values, the growth rate of the Perkins instability, which is the first term of the right hand side of the equation (4) is in an order of 10^{-5} sec^{-1} without east-westward wind. The actual growth time of this phenomenon have not been observed. But, considering their scale size and time scale of the variability of the ionosphere, it is considered that less than 15 minutes of the e-folding time seems to be reasonable to explain this phenomenon. The growth rate of 10^{-3}, which corresponds to the *e*-folding time of about 15 minutes, requires 200 m/s eastward wind. The average zonal wind around the midnight is, however, less than 50 m/s [Hedin et al., 1991]. Thus, east-westward wind and/or north-southward electric field much larger than the average value are needed for the enough growth rate of the Perkins instability.

The growth rate of the $\mathbf{E} \times \mathbf{B}$ type instability is described as the second term of the right hand side of the equation (4). The gradient of the Pedersen conductivity inside an TID can be estimated by the observation of the MU radar on May 18 in 1993. The height change of the ionosphere by TIDs make the field-line integrated conductivity change. The peak height change of the ionosphere from 280 km to 320 km altitude reduces the field-line integrated Pedersen conductivity from 0.84 to 0.50 S at the MU radar site, which are calculated with MSIS86, IRI90, IGRF95 models with the condition of May 18, 1993. The scale length of this conductivity gradients is about 130 km in this case. The *e*-folding time of the $\mathbf{E} \times \mathbf{B}$ type instability is about 40 minutes for the 130 km the scale size, with 50 m/s of the effective $\mathbf{E} \times \mathbf{B}$ drift velocity perpendicular to the conductivity gradient.

The growth rate of these instabilities under the average ionospheric condition is too small to grow up the modulations enough to generate the polarization field which are observed by

satellites. Furthermore, the growth rate dependencies on the direction of the wave vector are different both two types of instabilities. Therefore, the coupling of the Perkins instability and $\mathbf{E} \times \mathbf{B}$ instability is not easily achieved.

2.3.2 The Growth Rate inside TIDs

In the conjugate observation of Freja and the MU radar, the electric field fluctuations are observed inside a TID. The intense neutral wind of the acoustic gravity waves (AGWs) causes the traveling ionospheric disturbances (TIDs) [Hooke, 1968]. This neutral wind inside TID is not horizontal wind. The simplified dispersion relation of the acoustic gravity wave is as follows:

$$\omega^2(k^2_{horizontal} + k^2_{vertical}) - \omega^2_B k^2_{horizontal} = 0 \quad (5)$$

where ω_B is the Brunt-Bäisälä angular frequency [Hines, 1964]. With 12 minutes Brunt-Bäisälä period, the angle between the phase velocity and the horizontal is about 60 degrees for the AGW whose period is 60 minutes. Because the AGW is transverse wave, the wind vector of AGW is slanted from horizontal plane with 30 degrees.

When the neutral wind is horizontal, the growth rate of Perkins instability is expressed as (4), which is same as that of the case without neutral wind when the effective electric field, $\mathbf{E} + \mathbf{U} \times \mathbf{B}$ is replaced by the electric field, $\mathbf{E}$. The growth rate including the vertical component of the neutral wind is given by the following expression, for the case of the dip angle D = 45°, and the scale height, H = 50 km, (*see Appendix 2.*):

$$\gamma = 1.41 \times 10^{-5}\{\frac{E_0}{B} sin\alpha sin(\theta - \alpha) + U_{\parallel} - U_{\perp north} cos^2\alpha + \frac{1}{2} U_{east} sin2\alpha\} \quad (6)$$

satellites. Furthermore, the growth rate dependencies on the direction of the wave vector are different both two types of instabilities. Therefore, the coupling of the Perkins instability and $\mathbf{E} \times \mathbf{B}$ instability is not easily achieved.

2.3.2 The Growth Rate inside TIDs

In the conjugate observation of Freja and the MU radar, the electric field fluctuations are observed inside a TID. The intense neutral wind of the acoustic gravity waves (AGWs) causes the traveling ionospheric disturbances (TIDs) [Hooke, 1968]. This neutral wind inside TID is not horizontal wind. The simplified dispersion relation of the acoustic gravity wave is as follows:

$$\omega^2(k^2_{horizontal} + k^2_{vertical}) - \omega^2_B k^2_{horizontal} = 0 \quad (5)$$

where ω_B is the Brunt-Bäisälä angular frequency [Hines, 1964]. With 12 minutes Brunt-Bäisälä period, the angle between the phase velocity and the horizontal is about 60 degrees for the AGW whose period is 60 minutes. Because the AGW is transverse wave, the wind vector of AGW is slanted from horizontal plane with 30 degrees.

When the neutral wind is horizontal, the growth rate of Perkins instability is expressed as (4), which is same as that of the case without neutral wind when the effective electric field, $\mathbf{E} + \mathbf{U} \times \mathbf{B}$ is replaced by the electric field, $\mathbf{E}$. The growth rate including the vertical component of the neutral wind is given by the following expression, for the case of the dip angle D = 45°, and the scale height, H = 50 km, (*see Appendix 2.*):

$$\gamma = 1.41 \times 10^{-5}\{\frac{E_0}{B} sin\alpha sin(\theta - \alpha) + U_{\parallel} - U_{\perp north} cos^2\alpha + \frac{1}{2} U_{east} sin2\alpha\} \quad (6)$$

We can see the wind along the geomagnetic field line is effective for the growth of the irregularities. The 100 m/s parallel wind makes the e-folding time of the Perkins instability about 15 minutes. Furthermore, the parallel wind term is independent of the angle α. The irregularities with any direction can grow up through the Perkins instability when the parallel neutral wind is significant. Thus the coupling with the $\mathbf{E} \times \mathbf{B}$ instability is easily achieved. This coupling would enhance the evolution of the MEFs.

In above discussion, the background electric field and neutral wind are treated as independent each other. Electric field, however, would be generated to cancel the electric current induced by the neutral wind, $\Sigma\mathbf{U}\times\mathbf{B}$. The intense neutral wind inside a TID would generate the polarization electric field to be -$\mathbf{U} \times \mathbf{B}$. When the $\mathbf{E} + \mathbf{U} \times \mathbf{B}$ vanishes, the ionospheric irregularities could not grow. Considering the coupling of the nighttime F-region with the other region, such as the conjugate ionosphere and the E-region ionosphere, $\mathbf{E}$ would not cancel $\mathbf{U} \times \mathbf{B}$ completely because of the field aligned currents. Therefore, the coupling with the other region is important in the evolution of the irregularities. The effect of the coupling depends on the conductivity and the neutral wind in each regions. It makes the evolution process of the irregularities complicated. Further study including the coupling effect is needed.

2.4 Summary

The mid-latitude electric field fluctuations (MEFs) were observed by the conjugate observations of the MU radar and the Freja satellite. These electric field fluctuations were found on the field lines whose footpoints were around the peak and backside of a traveling ionospheric disturbance. The large scale modulation of the ionosphere, such as TIDs, would cause small scale modulations to grow up through ionospheric instabilities. Linear analysis

indicates that the Perkins instability and the $\mathbf{E} \times \mathbf{B}$ gradient drift instability inside TIDs would grow the MEFs up. Further theoretical studies are needed, in order to clarify the non-linear evolution of the fluctuations.

Chapter 3.

Evolution Process of Tens Kilometer Scale Irregularities in the Nighttime Mid-latitude Ionosphere

3.1 Introduction

As shown in Chapter 1, The wave length of the mid-latitude ionospheric electric field fluctuations (MEFs) is several tens kilometer and they extend several hundreds kilometer in the latitudinal direction. They are often observed simultaneously at the both magnetically conjugate points. They are interpreted to be transmitted along the geomagnetic field line from the source region to the opposite hemisphere. Magnetic field fluctuations also appear accompanying to the electric fluctuations in some cases. Therefore, field-aligned current is supposed to flow from the source ionosphere to the opposite ionosphere. Their occurrence rate is maximum at the invariant latitudes from 25 to 40 degrees. They have clear occurrence maximum in the post midnight local time sector, and rarely appear in the daytime.

A series of coordinated observations with the MU radar and the Freja satellite was conducted between 1993 and 1995 in order to clarify the relationship between ionospheric phe-

nomena detected by radars and MEFs, which is reported in Chapter 2. In these observations, the electric field fluctuations were observed on the field line whose foot point is in the region of the large scale ionospheric modulations, traveling ionospheric disturbances (TIDs). The relationship between TIDs and MEFs are discussed with the the linear analysis in Section 2.3.

The purpose of this chapter is to clarify the evolution process of the ionospheric irregularities with numerical simulation based on the equations derived by *Perkins* [1973]. Under an assumption that the geomagnetic field line to be equipotential, the momentum equation of ion is integrated along the geomagnetic field line. The growth rate of the irregularities obtained by the simulation is compared with that derived by the linear analysis by *Perkins* [1973]. The contribution of the conjugate ionosphere is one of the important features to be clarified. The results of the simulation are discussed with the observational results.

3.2 Basic Equations

Nighttime mid-latitude ionosphere is here numerically simulated to study the evolution of the irregularities through plasma process. Our objective is to clarify the physical process controlling the evolution of the MEFs observed by the DE-2 and the Freja satellites.

Our simulation is based on the equation derived by *Perkins* [1973]. The following equation (7) is derived by integration of the ion momentum equation along the geomagnetic field line, essentially the same as the equation (15) of *Perkins* [1973], but the neutral wind is explicitly expressed in our case, (*see Appendix 1*):

$$\frac{\partial \Sigma}{\partial t} + \nabla_\perp \cdot \{\Sigma(\frac{\mathbf{E}_\perp \times \mathbf{B}}{B^2} + \frac{m\mathbf{g} \times \mathbf{B}}{eB^2})\} = -\Sigma \frac{E_{east}}{B} \frac{cosD}{H} + \Sigma U_\parallel \frac{sinD}{H} + \frac{Nmg_\parallel}{B^2} \frac{sinD}{H}$$

(7)

Here, Σ is the field-line integrated Pedersen conductivity, $\mathbf{E}_\perp$ is electric field perpendicular to the geomagnetic field, $\mathbf{B}$ is the geomagnetic field, m is the mean molecular mass of ion, D is dip angle of the geomagnetic field, H is the scale height of the neutral atmosphere, $U_\parallel$ is neutral wind velocity parallel to the geomagnetic field, and N is the total electron content. The first term of the right hand side of the equation is the change of the conductivity by eastward electric field. Eastward electric field raises the ionosphere and decreases the line-integrated conductivity. The second term of the right hand side is the change of the line-integrated conductivity by the parallel neutral wind to the geomagnetic field. Parallel wind pushes down the plasma and increases the line-integrated conductivity in the northern hemisphere. The last term is the conductivity change caused by the gravity force.

The following is the electric current continuity equation.

$$\nabla_\perp \cdot (\mathbf{J}_{\perp N} + \mathbf{J}_{\perp S}) = 0 \tag{8}$$

or it can be written as

$$\nabla_\perp \cdot \{(\Sigma_N + \Sigma_S)\mathbf{E}_\perp + \Sigma_N \mathbf{U}_{\perp N} \times \mathbf{B} + \Sigma_S \mathbf{U}_{\perp S} \times \mathbf{B}\} = 0 \tag{9}$$

Subscripts "N" and "S" represent the values in the northern and southern hemispheres, respectively. This equation is similar to the equation (13) of *Perkins*, but the electric currents in the both hemispheres are included, and the currents by the plasma pressure and the gravity force are neglected.

Electric potential is calculated by solving the current continuity equation (9). The time evolution of the field-line integrated Pedersen conductivity of the each hemisphere is calculated using the equation (7) with the electric potential.

Cyclic boundary is used because the simulation box is considered to be smaller than the scale size of the region where the irregularities extend. That is, we simulate a portion of the irregularities which extend a few tens of wave length, with several tens of kilometer wave length.

The electric conductivity is calculated from the MSIS 86 [Hedin ,1987] and IRI 90 [Bilitza, 1990] models with the equations for the collision frequency by *Chapman* [1956]. The conductivity and electron density are integrated along the geomagnetic field of IGRF 95 model [IAGA Division V, 1995] from 200 km to 1000 km altitude. Field aligned flows of the plasma at the topside, 1000 km altitude, and bottomside, 200 km altitude, are neglected.

The growth rate of the Perkins instability can be estimated by the linear analysis [Perkins, 1973]. The growth rate is given by the following form, (*see Appendix 2*):

$$\gamma = \frac{E_0}{B}\frac{cosD}{H}sin\alpha sin(\theta-\alpha) + \frac{cosD}{BH}(U_{\parallel}B\frac{sinD}{cosD} - U_{north}Bcos^2\alpha + U_{east}Bsin\alpha cos\alpha) \tag{10}$$

α and θ are the angles of the direction of the wave vector, and the electric field from east, respectively. This growth rate is too small to grow the ionospheric irregularities from thermal fluctuations to the irregularities responsible for the electric field fluctuations observed by satellites under usual condition. Therefore, the gravity wave seeding is considered in this study, which *Kelley and Fukao* [1991] proposed in the study on the *F*-region field-aligned irregularities. Acoustic gravity waves initially generate vertical modulations of ionosphere, and then these modulations are enhanced by the plasma process and generate the conductivity modulations responsible for the polarization electric field observed by satellites.

In our simulation, these modulations induced by the gravity waves are given as $\pm$ 3.6 km

altitude modulations whose horizontal scale size is 64 km.

3.3 Results

3.3.1 A case of intense neutral wind in one hemisphere

The neutral wind is assumed only in the northern hemisphere in this case (case A). Ionospheric condition is chosen to match the condition of the June solstice in 1993, when the electric field fluctuations were observed by the Freja satellite in the coordinated observations with the MU radar [Saito et al., 1996]. The sunspot number is 50 and the magnetic activity set to be quiet. The location of the simulation region is selected to be over the MU radar site (35°N Lat. and 136°E Long.) and its magnetically conjugate region (17°S Lat. and 135°E Long.). Simulation box is 128 km×128 km in a plane perpendicular to the geomagnetic field. Local time is selected to be 23:00.

The field-line integrated Pedersen conductivity is 0.41 S and 0.19 S in the northern and southern ionospheres, respectively. The total electron content is $2.1\times10^{17}/\mathrm{m}^{-2}$ in the northern hemisphere and $7.1\times10^{16}/\mathrm{m}^{-2}$ in the southern hemisphere.

Figure 24 (a) is the initial state of ionosphere in the northern hemisphere. The perturbation component of the line-integrated Pedersen conductivity, which is normalized by the background value, is displayed in color contour. The descend(ascend) of the ionosphere increases(decreases) the line-integrated conductivity because the density of the neutral atmosphere is higher at lower altitude. The conductivity changes by a 10 km vertical ascend and descend of ionosphere from the initial position are -0.17 and $+0.20$ of the normalized conductivity, respectively. The arrows represent the electric current perpendicular to the geomagnetic field. The direction of the horizontal axis is chosen to the direction where the

linear growth rate given by equation (10) is maximum with 1.5 mV/m eastward electric field and 170 m/s eastward wind. That is, the horizontal axis of the simulation box is 40 degrees north from east. This horizontal axis is defined as X-axis, and the vertical axis is as Y-axis. The initial perturbations of conductivity, which is supposed to be generated by gravity waves, consist of two components, one is along the horizontal axis, and another is along the vertical axis. Their wave lengths are 64 km, and the amplitude of the conductivity perturbations correspond to ±3.6km vertical modulations for each component. This initial perturbations of conductivity are applied only on the northern ionosphere, and no perturbation is applied on the southern ionosphere.

Background eastward electric field at both hemispheres is 1.5 mV/m which supports the ionosphere against the gravity force. 170 m/s of the eastward neutral wind is applied only in the northern hemisphere on this equilibrium state. This eastward neutral wind is constant with time, because no feed back to the neutral wind from the ion drag force is included in this simulation. No neutral wind is applied in the southern ionosphere in this case.

The state of the northern hemisphere after 15 minutes is shown in Figure 24 (b) in the same format as that of Figure 24 (a). The perturbations whose wave vector along the vertical axis have vanished, and a sheet like structure has established. This shows that the wave perpendicular to the most unstable wave has been damped.

The appearance difference between the both sides of each sheet is attributed to the $\mathbf{E} \times \mathbf{B}$ instability. The sides at x = 30 km and 95 km, are linear along the Y-axis, and the sides at x = 0 km and 65 km show sinusoidal modulations. The gradient along the X-axis of the line-integrated conductivity is negative at the former locations, and positive at the latter locations. These horizontal gradients and the electric current in Y-direction enhance and damp the modulations of the both sides of the sheet structures by the $\mathbf{E} \times \mathbf{B}$ instability.

The electric potential at 40 minutes is shown in Figure 25. The field-aligned currents flow out at the high electric potential regions of the source ionosphere to the conjugate ionosphere and flows back into the low electric potential regions.

The evolution of the conductivity perturbations in the northern hemisphere is shown in Figure 26. Vertical axis is amplitude of the line-integrated Pedersen conductivity perturbations which is normalized by the background line-integrated conductivity. The difference between the maximum and minimum of the normalized conductivity is plotted as a solid line. The linear growth rate by equation (10) is plotted as a dashed line, and the linear growth rate including the effect of the electrical coupling with the conjugate ionosphere is plotted as a dotted line. This linear growth rate including the coupling effect is originally studied for the coupling with *E*-region ionosphere by *Klevans and Imel* [1978]. The growth rate in the initial 15 minutes is lower than that of the linear growth rate, and around zero. After 15 minutes, the perturbations keep growing with almost constant growth rate, comparable with the linear growth rate including the coupling effect. During the first 15 minutes, the perturbations whose wave vector along the vertical axis damp and the sheet like structure shown in Figure 24 (a) is formed. Once the sheet like structure is established, the structure keeps growing by the Perkins instability process.

3.3.2 A case of intense neutral wind in the both hemispheres

The evolution of modulations is studied for the case in which neutral wind is applied at the both hemispheres. The intensity of the neutral wind is 170 m/s eastward both in the northern and southern hemisphere (case B). The other conditions, such as conductivity, background electric field, and initial perturbations, are same as the case A.

The evolution of the difference of the conductivity in the northern ionosphere is repre-

sented by a solid line in Figure 27 with the same format as that of Figure 26. The evolution of the conductivity in the case A, where the intense $\mathbf{E} + \mathbf{U} \times \mathbf{B}$ is only in the northern hemisphere, is plotted as a dotted line for reference. The growth rate is significantly larger than that in the case A.

The dashed line in Figure 27 shows the conductivity evolution in the case when the wind directions in the both hemispheres are opposite each other, eastward in the northern hemisphere, westward in the southern hemisphere (case C). The amplitude of wind is 170 m/s in the both hemispheres. The other conditions are same as in the case A. We can see that the irregularities do not grow up in this opposite wind case.

In the southern hemisphere where no initial perturbations is applied, the perturbations of the ionospheric conductivity are excited by the polarization electric field which is initially generated in the northern hemisphere. The positive feed back between the change of the conductivity, the generated polarization electric field, and the movement of ionosphere, occurs not only in the source ionosphere but in the opposite hemisphere when the direction of the intense neutral wind is same in the both hemispheres. The eastward neutral wind in the opposite hemisphere enhances the perturbations (case B). On the other hand, negative feed back occurs when the directions of the effective electric field, $\mathbf{E} + \mathbf{U} \times \mathbf{B} \sim \mathbf{U} \times \mathbf{B}$, of the both hemispheres are opposite each other (case C). When the line-integrated conductivities in the both hemispheres are equal each other, no perturbation can grow up and damp. The slow growth of the conductivity perturbations of the case C after 15 minutes, which is shown in Figure 27, is caused by the difference of the line-integrated conductivity between the both ionospheres in this simulation.

3.3.3 A case of weak eastward current

The dependence of the linear growth rate on the background effective electric field is plotted on Figure 28. This growth rate is the maximum growth rate to the given background electric field. The linear growth rate is symmetric with respect to the north-south component of electric field, and includes the effect of the electric coupling between the conjugate regions. We can see the northward effective electric field is important. The irregularities grow up by the Perkins instability when the northward component of the effective electric filed is intense, and the east-west component is weak.

Another simulation made with 172 m/s neutral wind only in the northern hemisphere, which blows 10° northward from east (case D). The eastward component of neutral wind is 170 m/s, which is same as the other cases, and the northward component is 30 m/s. The other conditions are same as the other cases. In this case northward component of the neutral wind reduces the eastward component of the effective electric field. Because the force balance in the vertical direction is not satisfied, the ionosphere gradually descends by the gravity force. The evolution of the conductivity perturbation in the northern hemisphere is plotted in Figure 29. Solid line shows the amplitude of the conductivity perturbations, and dashed lines are the maximum and minimum values of the normalized conductivity. The gradual increases of the maximum and minimum values at the early stage indicate that the whole ionosphere gradually descends by the gravity. Dotted line is the evolution of the conductivity perturbations of the case A, in which the ionospheric conditions are same except for the northward component of neutral wind. The conductivity perturbations efficiently grow when the eastward component of the effective electric field is weak.

3.4 Discussion

3.4.1 Adequacy of the present formulations

The simulation in this study is two dimensional. Ionospheric parameters and equations are integrated along the geomagnetic field line. Electric potential, neutral wind, scale height of neutral atmosphere, the gravity acceleration, and the geomagnetic field, are assumed to be constant with altitude. The assumptions of the former two parameters influence on the result of the simulation.

Zinchenko and Nisbet [1977] defined the coupling length between the conjugate regions, and between the F- and E-regions. Larger scale electric field than this coupling length is supposed to be transmitted along the field line without significant damping by short circuit of currents. Their Figure 1 shows that the coupling length between the conjugate regions are less than 1 km in the most of the nighttime over Arecibo. Therefore, field line is practically equipotential between the both F-region ionospheres for the scale size of the irregularities discussed in this study. The coupling length between the F- and E-regions was calculated to be more than 10 km. Therefore the equipotential of the field line between the F- and E-regions could not be completely established. However, this does not affect in our case because the E-region is not included in this simulation from the reason discussed later.

The height profile of the neutral wind has been studied observationally and by the global circulation model simulation [Ganguly et al., 1987; Forbes and Roble, 1990]. They showed that the neutral wind is almost constant in the altitudes above E-region because of the high viscosity. Thus, the assumption of the constant neutral wind is acceptable.

The loss and production of ionospheric plasma are neglected in our simulation. The plasma loss by recombination is important below 300 km altitude because of the high neutral

density. In our study, local time is set to be around the midnight when the ionosphere is high enough to neglect the loss of plasma. Plasma flux from the plasmasphere is also neglected, although this flux plays an important role in the maintenance of the nighttime F-region ionosphere [Meléndez-Alvira et al., 1993]. Under these assumption, the total electron content is constant in this study.

Considering the electrical coupling between the F- and E-regions, some portion of the polarization electric field generated in the F-region irregularities would be canceled at the E-region. The efficiency of this cancelation is controlled by the ratio of the ionospheric conductivities of the two regions. The electric conductivity significantly varies with solar cycle and seasons. Field-line integrated Pedersen conductivity calculated with MSIS 86 model and IRI 90 model is 1.59 S and 0.58 S in summer and winter, respectively, under the solar maximum condition, for midlatitude F-region ionosphere in the midnight. The E-region conductivity in solar maximum is calculated to be 0.25 S and 0.19 S in summer and winter, respectively. Because the ratio of the E-region conductivity to that of the F-region is 0.16 and 0.33 in summer and winter, respectively, the effect of the E-region could be neglected in the solar maximum condition.

In the solar minimum period, however, the conductivity ratio of the E-region to F-region is 0.42 and 2.2 in summer and winter, respectively. In this period, especially in winter, the cancelation of the polarization field by the E-region cannot be neglected. However, the amplitude of the E-region neutral wind velocity is less than that of the F-region because the density of the neutral atmosphere is high. Furthermore, the direction of the wind varies within the E-region [Harper, 1981]. Thus, the line-integrated product of the conductivity and neutral wind of the E-region is smaller than that of the F-region. Therefore, the neglect of E-region does not affect the validity of the result, although the growth rate of irregularities

could be over estimated in the solar minimum condition.

Numerical simulation reveals some characteristics of the plasma process which evolves the ionospheric irregularities. These results are compared with the previously obtained observational results in the remainder of this section.

3.4.2 Comparison with the MEF observation

One of the characteristics of the MEF observed by satellites is that the direction of the electric field fluctuation is one-sided during one event. As shown in Figure 2 of *Saito et al.*, [1995], the electric field fluctuates not sinusoidally but to one-side of the background electric field. Such a one-sideness is not reproduced in this numerical simulation. The initial perturbations are given in a sinusoidal form, and this sinusoidal form is conserved with some distortion. Therefore the one-sideness could be caused by the non-sinusoidal form of the initial perturbations.

The conservation of the characteristics of the initial perturbation is also seen on the scale size. The scale size of the irregularities which evolves in the simulation is that of the initial perturbations. No scale dependence of the growth rate appears for the scale size from 10 km to 100 km in our simulation. The reason is that the Perkins instability is essentially independent on the scale size of the irregularities. The scale of MEF is several tens kilometer. This scale is supposed to be the scale size of the initial ionospheric perturbations generated by acoustic gravity waves. The acoustic gravity wave is assumed to generate the initial perturbations which play a role as the seed of the irregularities in this study. The detailed study of this seeding process is, however, out of our scope.

3.4.3 Background Ionospheric Current

As shown in the numerical simulation, an intense effective electric field, $\mathbf{E}+\mathbf{U}\times\mathbf{B}$, is necessary for the growth of the irregularities. However, the electric current creates the polarization electric field to prevent the intense electric current in the nighttime ionosphere. When the complete polarization is established, the ionospheric plasma drifts with the same velocity as the neutral wind. The coherence between plasma drift and neutral wind is reported by various authors [Burnside et al., 1983; Fejer, 1993; Coley et al., 1994]. The anti-correlation of the parallel and northward perpendicular drifts of plasma observed by the IS radars is supposed to be another evidence that plasma moves with neutral gas [Kelley, 1989].

To evolve the irregularities by the Perkins instability, the difference of the background plasma drift and neutral wind must be significantly large. In addition to this requirement, our simulation shows that irregularities are hard to grow up when the directions of the electric current in the both hemisphere are opposite. This is another restriction of the background condition in which ionospheric irregularities grow up by the Perkins instability. To confirm the process simulated in this study, we need observation of the ionospheric effective electric field, $\mathbf{E}+\mathbf{U}\times\mathbf{B}$, when the electric field fluctuations are observed.

3.4.4 Relation with Other Ionospheric Phenomena

The electric field fluctuations observed by satellites are supposed to be attributed to the polarization electric field generated by the line-integrated conductivity fluctuations. These conductivity fluctuations are the result of vertical modulations of the ionosphere. If this is the case, the vertical modulations would be observed at the footpoint of the electric field fluctuations. The conjugate observations of the Freja satellite and the MU radar were the opportunity to observed such an ionospheric structure, but the scale size of the structure is

too small to detect by the MU radar in the observation mode used there [Saito et al., 1996]. Well-defined bands of the F-region ionosphere is observed with the Arecibo IS radar in the nighttime, in which the F-region is alternately high and low with more than 30 km height difference [Behnke, 1979]. The horizontal scale of such bands is several tens km, comparable with the wave length of MEF. This structure seems to be responsible for the electric field fluctuations. But this relationship between the ionospheric structure observed by ground based radar and the MEF observed by satellites has not been clarified by a simultaneous observation.

3.5 Summary

Nighttime mid-latitude ionosphere is numerically simulated to study the evolution of the irregularities which generate the electric field fluctuations observed by satellites. This simulation includes the interaction between the F-region ionosphere in both hemispheres.

When intense eastward neutral wind is applied on the initial ionospheric perturbations, the perturbations are grown up through the Perkins instability. At the first stage of the evolution, the irregularities form a sheet like structure, whose wave vector is along the direction where the growth rate predicted by the linear analysis is maximum. In this stage, the growth rate of irregularities is almost zero. After the formation of this sheet like structure, the irregularities start to grow with the growth rate comparable to that predicted by the linear analysis. The coupling with the conjugate ionosphere is important in the evolution of irregularities even when the conjugate ionosphere is in winter. The electric current of the conjugate ionosphere can grow or damp the irregularities depending on its direction.

Further observations including the neutral wind and electric field at the both conjugate regions are necessary to assess the importance of these plasma process.

Chapter 4.

Summary

The DE 2 satellite observed electric field fluctuations on the topside of the nighttime midlatitude ionosphere. They extended several hundred kilometers in the latitudinal direction with wavelengths of several tens of kilometers, and their amplitudes were a few millivolts per meter. Such fluctuations were often observed at magnetically conjugate points in the northern and southern hemispheres. These electric field fluctuations are perpendicular to the geomagnetic field. They are not accompanied by any significant plasma depletion or electron temperature variations. Magnetic field fluctuations are sometimes observed simultaneously with electric field fluctuations. We interpret that these fluctuations are caused by field-aligned currents which flow from the ionosphere in one hemisphere to the conjugate point in the other hemisphere. The power spectrum of these midlatitude electric field fluctuations follows a power law of the form $Power \propto f^{-n}$, with the spectral index n of 3.5 to 4.5, which is steeper than that of the electric field fluctuations in the high-latitude ionosphere or in the equatorial ionosphere.

The Freja satellite and the MU radar conjugate observations had been conducted from

1993 to 1996 to clarify the generation mechanism of the mid-latitude electric field fluctuations (MEFs). The detection of the MEFs by the Freja satellite at higher altitude than 1000 km have confirmed that the MEFs are transmitted along the geomagnetic field line without any significant damping. One night of these conjugate observations, MEFs were observed in a traveling ionospheric disturbance (TID). In the nights when the MEFs were observed by Freja, large scale horizontal structures in the ionosphere were observed with the MU radar. Spread-F phenomena were also observed by ionosondes associating with these structures. The large scale modulation of the ionosphere, such as TIDs, might make small scale modulations grow up through ionospheric instabilities. Linear growth rate is evaluated using a set of equations describing the growth of the mid-latitude ionospheric irregularities [Perkins, 1973]. It is shown that the growth rate is too small under the average ionospheric condition, but, when the neutral wind inside TIDs is included, it can be large enough to generate MEFs.

To study the evolution process of irregularities, nighttime mid-latitude ionosphere is numerically simulated. This simulation includes the interaction between the F-region ionosphere in both hemispheres.

When intense eastward neutral wind is applied on the initial ionospheric perturbations, the perturbations are grown up through the Perkins instability. At the first stage of the evolution, the irregularities form a sheet like structure, whose wave vector is along the direction where the growth rate predicted by the linear analysis is maximum. In this stage, the growth rate of irregularities is almost zero. After the formation of this sheet like structure, the irregularities start to grow with the growth rate comparable to that predicted by the linear analysis. The coupling with the conjugate ionosphere is important in the evolution of irregularities even when the conjugate ionosphere is in winter. The electric current of the

conjugate ionosphere can grow or damp the irregularities depending on its direction.

The mid-latitude ionospheric irregularities have been studied by both of the observational and theoretical ways. There still have some questions to be solved. To solve these questions, further coordinated observations are necessary, in which various ionospheric parameters, such as neutral wind, electric field, and electron density profile, are observed at various positions, such as upper ionosphere by satellites, and magnetically conjugate points. Further theoretical studies, such as three dimensional simulations, are also necessary.

Appendix

1 Basic Equations of the Perkins and the $\mathbf{E}\times\mathbf{B}$ instabilities

The mid-latitude ionosphere is equipotential along the geomagnetic field line when the electric potential is more than kilometer scale size. It is convenient to use the field line integrated parameters for describing the mid-latitude ionosphere phenomena. A set of equations for the field line integrated Pedersen conductivity and the electric potential is derived here from the continuity and momentum equations of ion and the electric current continuity equation.

$$0 = F + ne\mathbf{v}\times\mathbf{B} - mn\nu(\mathbf{v}-\mathbf{U}) \quad (F \equiv ne\mathbf{E} - \nabla P + mn\mathbf{g}) \tag{11}$$

$$\mathbf{v} = \mathbf{U} + \frac{F}{mn\nu} + \frac{e}{m\nu}\mathbf{v}\times\mathbf{B}$$

$$\mathbf{v}_{\parallel} = \mathbf{U}_{\parallel} + \frac{F_{\parallel}}{mn\nu} \simeq \mathbf{U}_{\parallel} + \frac{\mathbf{g}_{\parallel}}{\nu} \tag{12}$$

$$\mathbf{v}_{\perp}\times\mathbf{B} = \mathbf{U}_{\perp}\times\mathbf{B} + \frac{F_{\perp}\times\mathbf{B}}{mn\nu} + \frac{eB^2}{m\nu}\mathbf{v}_{\perp}$$

$$\mathbf{v}_{\perp} = \mathbf{U}_{\perp} + \frac{F_{\perp}}{mn\nu} + \frac{e}{m\nu}\mathbf{U}_{\perp}\times\mathbf{B} - (\frac{eB}{m\nu})^2\mathbf{v}_{\perp} + \frac{eF_{\perp}\times\mathbf{B}}{(m\nu)^2 n}$$

$$\mathbf{v}_{\perp} = \frac{F_{\perp}\times\mathbf{B}}{neB^2} + \frac{m\nu F_{\perp}}{ne^2B^2} + \frac{m\nu}{eB^2}\mathbf{U}_{\perp}\times\mathbf{B} \simeq \frac{\mathbf{E}_{\perp}\times\mathbf{B}}{B^2} + \frac{m\mathbf{g}_{\perp}\times\mathbf{B}}{eB^2} \tag{13}$$

$$\mathbf{j}_{\perp} = \frac{mn\nu}{B^2}(\mathbf{E}_{\perp} + \mathbf{U}_{\perp}\times\mathbf{B}) \tag{14}$$

The continuity equation of ion is multiplied by $\frac{m\nu}{B^2}$. Then, the following equation is derived by the integration along the geomagnetic field line from the bottomside to the topside of the ionosphere.

$$\frac{m\nu}{B^2}\frac{\partial n}{\partial t} + \frac{m\nu}{B^2}\nabla_{\perp}\cdot(n\mathbf{v}_{\perp}) = -\frac{m\nu}{B^2}\nabla_{\parallel}\cdot(n\mathbf{v}_{\parallel})$$

$$\frac{\partial \sigma}{\partial t} + \nabla_\perp \cdot (\sigma \mathbf{v}_\perp) = \sigma \mathbf{v} \cdot \perp \frac{\nabla_\perp \nu}{\nu} - \nabla_\parallel \cdot (\sigma \mathbf{v}_\parallel) + \sigma \mathbf{v}_\parallel \cdot \frac{\nabla \| \nu}{\nu} \quad (\sigma \equiv \frac{mn\nu}{B^2})$$

$$\frac{\partial \Sigma}{\partial t} + \nabla_\perp \cdot \{\Sigma(\frac{\mathbf{E}_\perp \times \mathbf{B}}{B^2} + \frac{m\mathbf{g} \times \mathbf{B}}{eB^2})\} = -\Sigma \frac{E_{east}}{B} \frac{cosD}{H} + \Sigma U_\parallel \frac{sinD}{H} + \frac{Nmg_\parallel}{B^2} \frac{sinD}{H} \quad (15)$$

$$\frac{\nabla_\perp \nu}{\nu} = -\frac{cosD}{H} \mathbf{e}_{north}, \quad \frac{\nabla_\parallel \nu}{\nu} = \frac{sinD}{H} \mathbf{e}_\parallel$$

Following equations are derived from the continuity equation of the electric current.

$$\nabla_\perp \cdot \mathbf{J} = 0$$

$$\nabla_\perp \cdot \{\Sigma(\mathbf{E}_\perp + \mathbf{U}_\perp \times \mathbf{B})\} = 0 \quad (16)$$

2 Linear Growth Rate of the Perkins and the $\mathbf{E} \times \mathbf{B}$ instabilities

Assuming $\Sigma_1, \phi_1 \propto exp(\gamma t + i\mathbf{k} \cdot \mathbf{x})$, the growth rate is derived from the equation (15) in the frame moving in the velocity of $\frac{\mathbf{E}_\perp \times \mathbf{B}}{B^2} + \frac{m\mathbf{g}_\perp \times \mathbf{B}}{eB^2}$:

$$\gamma \Sigma_1 + i \nabla_\perp \Sigma_0 \cdot \frac{-\phi_1 \mathbf{k} \times \mathbf{b}}{B} = -ik_{east} \Sigma_0 \phi_1 \frac{cosD}{BH} - \Sigma_1 \frac{E_{0east}}{B} \frac{cosD}{H} + \Sigma_1 U_\parallel \frac{sinD}{H} \quad (17)$$

From the equation (16), the current continuity equation, the perturbation component of the electric potential is given in the following form:

$$\begin{aligned} \nabla_\perp(-\Sigma \nabla \phi + \Sigma \mathbf{U}_\perp \times \mathbf{B}) &= -\Sigma_0 \nabla_\perp^2 \phi_1 + \mathbf{E}^* \cdot (\nabla \Sigma_0) \\ &= k^2 \Sigma_0 \phi_1 + i \mathbf{E}_0^* \cdot \mathbf{k} \Sigma_1 = 0 \\ \phi_1 &= \frac{\mathbf{E}^*{}_0 \cdot \mathbf{k}}{ik^2 \Sigma_0} \Sigma_1 \end{aligned} \quad (18)$$

$$\mathbf{E}^* \equiv \mathbf{E} + \mathbf{U} \times \mathbf{B}$$

Under an assumption that the neutral wind has no vertical component, $U_{\parallel} = \frac{cosD}{sinD} U_{north}$, the growth rate is derived from equations (17) and (18).

$$\begin{aligned}
\gamma &= (\frac{k_{east}\mathbf{E^*}_0 \cdot \mathbf{k}}{k^2} - E_{0east} + U_{\parallel} B \frac{sinD}{cosD}) \frac{cosD}{BH} + \frac{\mathbf{E^*}_0 \cdot \mathbf{k}}{k^2 \Sigma_0 B} \nabla_{\perp} \Sigma_0 \cdot (\mathbf{k} \times \mathbf{b}) \\
&= \frac{k_{north}}{k^2} (k_{east} E^*_{0north} - k_{north} E^*_{0east}) \frac{cosD}{BH} + \frac{E^*_0 cos(\theta^* - \alpha)}{\Sigma_0 B} (-\nabla_{east} \Sigma_0 k_{north} + \nabla_{north} \Sigma_0 k_{east}) \\
&= E^*_0 sin\alpha (sin\theta^* cos\alpha - cos\theta^* sin\alpha) \frac{cosD}{BH} + \frac{E^*_0}{B} \frac{\nabla_{\perp} \Sigma_0}{\Sigma_0} cos(\theta^* - \alpha)(sin\beta cos\alpha - cos\beta sin\alpha) \\
&= \frac{E^*_0}{B} \frac{cosD}{H} sin\alpha sin(\theta^* - \alpha) + \frac{E^*_0}{B} \frac{\nabla_{\perp} \Sigma_0}{\Sigma_0} cos(\theta^* - \alpha) sin(\beta - \alpha) \qquad (19)
\end{aligned}$$

α, β and θ^* are the angles of the direction of the wave vector, the gradient of the line-integrated conductivity, and the effective electric field, $\mathbf{E}+\mathbf{U}\times\mathbf{B}$, from east, respectively.

The first term of the right hand side is caused by the field line integrated conductivity change as the result of the rise and descend of ionosphere (the Perkins instability). The second term is caused by the $\mathbf{E} \times \mathbf{B}$ drift with the gradient of the field line integrated conductivity (the $\mathbf{E} \times \mathbf{B}$ gradient drift instability).

The growth rate of the $\mathbf{E} \times \mathbf{B}$ type instability is maximum when $\mathbf{k} \| \mathbf{E}^*$, and proportional to $sin(\beta - \theta^*)$.

The growth rate of the Perkins instability is positive when the wave vector is between the $\mathbf{E}^*$ and east, and decreases when one of the angles of the wave vector from the $\mathbf{E}^*$ or from east gets lower. Therefore, the perturbation along the background electric field and east-westward is stable. The growth rate is maximum when $\alpha = \frac{\theta^*}{2}$.

Without the assumption that neutral wind is horizontal, the growth rate of the Perkins instability is given by the following expression.

$$\gamma = \frac{E_0}{B} \frac{cosD}{H} sin\alpha sin(\theta - \alpha) + \frac{cosD}{BH} (U_{\parallel} B \frac{sinD}{cosD} - U_{north} B cos^2\alpha + U_{east} B sin\alpha cos\alpha) \qquad (20)$$

References

Aggson, T. L., W. J. Burke, N. C. Maynard, W. B. Hanson, P. C. Anderson, W. R. Hoegy, and J. L. Saba, Equatorial bubbles updrafting at supersonic speeds, *J. Geophys. Res., 97,* 8581-8590, 1992.

Basu Su., Sa. Basu, S. Ganguly, and J. A. Klobuchar, Generation of Kilometer Scale Irregularities During the Midnight Collapse at Arecibo, *J. Geophys. Res., 86,* 7607-7616, 1981.

Behnke, R., *F* Layer Height Bands in the Nocturnal Ionosphere Over Arecibo, *J. Geophys. Res., 84,* 974-978, 1979.

Bering, E. A. III, A Sounding rocket observation of an apparent wake generated parallel electric field, *J. Geophys. Res., 88,* 961-979, 1983.

Bilitza D. (Ed.), International Reference Ionosphere 1990, *Rep. 90-22,* Natl. Space Sci. Data Cent., Greenbelt, Md., Nov. 1990.

Burke, W. J., D. E. Donatelli, R. C. Sagalyn, and M. C. Kelly, Low density regions observed at high altitudes and their connection with equatorial spread-*F*, *Planet. Space Sci., 27,* 593-601, 1979.

Burnside, R. G., J. C. G. Walker, R. A. Behnke, and C. A. Gonzales, Polarization electric fields in the nighttime F layer at Arecibo, *J. Geophys. Res., 1983,* 6259-6266, 1983.

Chapman, S., The electric conductivity of the ionosphere: A review, *Nuovo Cimento, 5,* Supple., 1385-1412, 1956.

Coley, W. R., R. A. Heelis, and N. W. Spencer, Comparison of low-latitude ion and neutral zonal drifts using DE 2 data, *G. Geophys. Res., 99,* 341-348, 1994.

Farthing, W. H., M. Sugiura, B. G. Ledley, and L. J. Cahill Jr., Magnetic field observations on DE-A and -B, *Space Sci. Instrum., 5,* 551, 1981.

Fejer, B. G., F region plasma drifts over Arecibo: solar cycle, seasonal, and magnetic activity effects, *J. Geophys. Res., 98,* 13,645-13,652, 1993.

Forbes, J. M., and R. G. Roble, Thermosphere-ionosphere coupling: an experiment in interactive modeling, *J. Geophys. Res., 95,* 201-208, 1990.

Forget, B., J.-C. Cerisier, A. Berthelier, and J.-J. Berthelier, Ionospheric closure small-scale Birkeland currents, *J. Geophys. Res., 96,* 1843-1847, 1991.

Fukao, S, T. Sato, T. Tsuda, K. Wakasugi, and T. Makihara, The MU Radar with an Active Phased Array System 1. Antenna and Power Amplifiers, *Radio Sci., 20,* 1155-1168, 1985.

Fukao, S, M. C. Kelley, T. Shirakawa, T. Takami, M. Yamamoto, T. Tsuda, and S. Kato, Turbulent Upwelling of the Mid-Latitude Ionosphere 1. Observational Results by the MU Radar, *J. Geophys. Res., 96,* 3725-3746, 1991.

Ganguly, S., R. A. Behnke, and B. A. Emery, Average electric field behavior in the ionosphere above Arecibo, *J. Geophys. Res., 92,* 1199-1210, 1987.

Georges, T. M., HF Doppler Studies of Traveling Ionospheric Disturbances, *J. Atmos. Terr. Phys., 30,* 735-746, 1968.

Gonzales, C. A., M. C. Kelley, R. A. Behnke, J. F. Vickrey, R. Wand, and J. Holt, On the latitudinal variations of the ionospheric electric field during magnetospheric disturbances, *J. Geophys. Res., 88,* 9135-9144, 1983.

Gurnett, D. A., R. L. Hugg, J. D. Menietti, J. L. Burch, J. D. Winningham, and S. D. Shawhan, Correlated low-frequency electric and magnetic noise along the auroral field lines, *J. Geophys. Res., 89,* 8971, 1984.

Harper, R. M., Some results on mean tidal structures and day-to-day variability over Arecibo, *J. Atmos. Terr. Phys., 43,* 255-262, 1981.

Hedin, A. E., MSIS-86 Thermospheric Model, *J. Geophys. Res. 92,* 4649-4662, 1987.

Holtet, J. A., N. C. Maynard, and J. P. Heppner, Variational electric fields at low latitudes, and their relation to spread-F and plasma irregularities, *J. Atmos. Terr. Phys., 39,* 247-262, 1977.

Hooke, W. H., Ionospheric Irregularities Produced by Internal Atmospheric Gravity Waves, *J. Atoms. Terr. Phys., 30,* 795-823, 1968.

Huang, C. S., C. A. Miller, and M. C. Kelley, Basic properties and gravity wave initiation of the midlatitude F region instability, *Radio Science, 29,* 395-405, 1994.

IAGA Division V, Working Group 8, International Geomagnetic Reference Field, 1995 Revision, *J. Geomag. Geoelectr., 47,* 1257-1261, 1995.

Kelley, M. C., *The Earth's Ionosphere,* Academic, San Diego, Calif., 1989.

Kelley, M. C., and S. Fukao, Turbulent upwelling of the mid-latitude ionosphere, 2, Theoretical framework, *J. Geophys. Res., 96,* 3747-3753, 1991.

Klevans, E. H., and G. Imel, E region coupling effects on the Perkins spread F instability, *J. Geophys. Res., 83,* 199-202, 1978.

Krehbiel, J. P., L. H. Brace, R. F. Theis, W. H. Pinkus, and R. B. Kaplan, The Dynamics Explorer Langmuir probe instrument, *Space Sci. Instrum., 5,* 493-502, 1981.

Lundin, R., G. Haerendel, and S. Grahn, The Freja Project, *Geophys. Res. Let., 21* 1823-1826, 1994.

Maruyama, T., $\mathbf{E} \times \mathbf{B}$ Instability in the F region at Low- to Midlatitudes, *Planet. Space Sci., 38,* 273-285, 1990.

Maynard, N. C., E. A. Bielecki, and H. F. Burdick, Instrumentation for vector electric field measurements from DE-B, *Space Sci. Instrum., 5,* 523-534, 1981.

Meléndez-Alvira, D. J., R. G. Burnside, and J. C. G. Walker, Modeling the Arecibo nighttime *F*2 layer 1. overhead properties, *J. Geophys. Res., 98,* 5993-6011, 1993.

Muldrew, D. B., The Formation of Ducts and Spread *F* and the Initiation of Bubbles by Field-Aligned Currents, *J. Geophys. Res., 85,* 613-625, 1980.

Oliver, W L., S. Fukao, T. Takami, M. Yamamoto, T. Tsuda, T, Nakamura, and S. Kato, Thermospheric Meridional Winds Measured by the Middle and Upper Atmosphere Radar, *J. Geophys. Res., 95,* 7683-7692, 1990.

Oliver, W. L., Y. Yamamoto, T. Takami, S. Fukao, M. Yamamoto, and T. Tsuda, Middle and Upper Atmosphere Radar Observations of Ionospheric Electric Fields, *J. Geophys. Res., 98,* 11,615-11,627, 1993.

Park, C. G., Downward mapping of high-latitude ionospheric electric fields to the ground, *J. Geophys. Res., 81,* 168-174, 1976.

Park, C. G., Comparison of two-dimensional and three-dimensional mapping of ionospheric electric field, *J. Geophys. Res., 84,* 960-964, 1979.

Perkins, F., Spread *F* and ionospheric currents, *J. Geophys. Res., 78,* 218-226, 1973.

Reid, G. C. , Ionospheric effects of electrostatic fields generated in the outer magnetosphere, *J. Res. Natl. Bur. Stand. U.S., Sect. D,* 69(6), 827-837, 1965.

Rodger, A. S., The simultaneous occurrence of spread-*F* at magnetically conjugate points, *J. Atmos. Terr. Phys., 38,* 1365-1368, 1976.

Rodger, A. S., and J. Aarons, Studies of Ionospheric *F* region Irregularities from Geomagnetic Mid-Latitude Conjugate Regions, *J. Atmos. Terr. Phys. , 50,* 63-72, 1988.

Scannapieco, A. J., S. R. McDonald, S. L. Ossakow, D. L. Book, and B. E. McDonald, Theoretical and Numerical Simulation Studies of Midlatitude F Region Irregularities, *NRL Memo. Rep. 3014,* Naval Research Lab., Washington D.C., 1975.

Sugiura, M., A fundamental magnetosphere-ionosphere coupling mode involving field-aligned currents as deduced from DE-2 observation, *Geophys. Res. Lett., 11,* 877, 1984.

Tsunoda, R. T., S. Fukao, and M. Yamamoto, On the Origin of Quasi-periodic Radar Backscatter from Midlatitude Sporadic *E*, *Radio Sci., 29,* 349-365, 1994.

Watanabe, S., and H. Oya, Occurrence characteristics of low latitude ionosphere irregularities observed by impedance probe on board the Hinotori satellite, *J. Geomagn. Geoelectr. , 38,* 125-149, 1986.

Yamamoto, M., N. Komoda, S. Fukao, R. T. Tsunoda, T. Ogawa, and T. Tsuda, Spatial Structure of the *E* Region Field-aligned Irregularities Revealed by the MU Radar, *Radio Sci., 20,* 337-347, 1994.

Yeh, K. C., D. Simonich, J. Mawdsley, and G. F. Preddy, Scintillation observations at medium latitude geomagnetically conjugate stations, *Radio Sci., 3,* 690-697, 1968.

Zinchenko, G. N., and J. S. Nisbet, Coupling of mid-latitude spread-*F* between conjugate stations, *J. Atmos. Terr. Phys., 39,* 469-474, 1977.

Figure captions

Figure 1: Electron temperature, satellite potential, and plasma density deduced from the Langmuir probe data and electric field obtained by VEFI, (a) in the southern hemisphere, and (b) in the northern hemisphere.

Figure 2: The parallel and perpendicular components of the electric field fluctuation, and φ and θ, which are the angles between the Magsat model field and the x-z plane and the x-y plane in SPC system, respectively, (a) in the southern hemisphere, and (b) in the northern hemisphere.

Figure 3: High-pass filtered x and y components of electric field and the plasma density from 12:33 to 12:53 UT on May 3, 1982.

Figure 4: The y component (vertical component) of the electric field fluctuation observed by the DE-2 in the northern and southern hemispheres.

Figure 5: Band-pass filtered magnetic and electric field obtained, (a) in the southern hemisphere, and (b) in the northern hemisphere.

Figure 6: Power spectrum of the perpendicular component of the electric field fluctuation, (a) in the southern hemisphere, and (b) in the northern hemisphere.

Figure 7: Histogram of the occurrence rate of the MEFs by the DE-2 observation with respect to local time.

Figure 8: Histogram of the occurrence rate of the MEFs by the DE-2 observation with respect to invariant latitude.

Figure 9: (a) Contour map of the occurrence rate of the MEFs with respect to local time and invariant latitude. (b) Same as (a) for the cases of AE index larger than 200. (c) Same as (a) for the cases of AE index smaller than 200.

Figure 10: Geographical distribution of the occurrence rate of the MEFs by the DE-2 observation.

Figure 11: Histogram of the occurrence rate of the MEFs by the DE-2 observation with respect to altitude.

Figure 12: Schematic illustration for the transhemisphere field-aligned current and the induced electric field which is northward and perpendicular to the geomagnetic field, and magnetic field in z direction along the DE-2 trajectory.

Figure 13: Calculated profiles of the electrostatic potential whose scale lengths are indicated.

Figure 14: Freja electric field observation on May 18, 1993. Electric field fluctuations are seen between 14:03:20 an 14:13:20 UT in both electric field components, E1 and E2.

Figure 15: The Freja trajectory over Japan on May 18, 1993. Solid line with an arrow head represents the Freja trajectory projected on 325 km altitude. The electric field fluctuations are superimposed to the trajectory. The hatched area represents the location of the TID peak when Freja flew across these region at 14:10 UT.

Figure 16: (a) The F-region height in the night of May 18, 1993, obtained by the northward and southward beams of the MU radar multi-beam observation with 20° zenith angle. (b) Same as (a), but obtained by the eastward and westward beams. (c) The apparent F-region height derived with the ionosondes at Shigaraki and Kokubunji.

Figure 17: The locations of the MU radar site and the electric field fluctuations observed by Freja during the conjugate observations. The orbits where the fluctuations were observed are projected on 300 km altitude in the northern hemisphere.

Figure 18: Freja electric field observation on June 8, 1995. Electric field fluctuations are seen between 15:36:20 an 15:45:00 UT in the both electric field components.

Figure 19: The MU radar Range-Time-Intensity plot from 21:00 on June 8 to 03:00 on June 9 JST in 1995. The radar echo intensity of the northward directed beam with 10° zenith angle is displayed. Electric field fluctuations were observed by Freja around 00:40 JST.

Figure 20: The F-region height in the night of June 8, 1995, obtained by the MU radar multi-beam observation. Solid line represents the average peak height derived by seven beams, and error bars represent the mean value of the deviations of the each beam peaks from the average peak height.

Figure 21: Same as Figure 19 from 21:00 on June 6 to 03:00 on June 7 JST in 1995, the night without the electric field fluctuations.

Figure 22: Same as Figure 20 on the night of June 6, 1995, except that they are derived from the eight beams.

Figure 23: The geometry of the effective electric field, $\mathbf{E}^*$, the gradient of field-line integrated Pedersen conductivity, $\nabla\Sigma$, and wave vector, k, in a plane perpendicular to the geomagnetic field.

Figure 24: (a) The initial state of the the perturbation component of the line-integrated Pedersen conductivity in the northern hemisphere, which is normalized by the background value. Arrows represent the electric current perpendicular to the geomagnetic field. Simulation box is 128 km$\times$128 km in a plane perpendicular to the geomagnetic field. The horizontal axis is 40 degree north from east. (b) 15 minutes later of (a) for the case A.

Figure 25: The electric potential at 40 minutes later for the case A. The horizontal axis is 40 degree north from east as Figure 24.

Figure 26: The evolution of the conductivity perturbations, with 170 m/s eastward wind in the northern hemisphere (case A), is represented by a solid line. Conductivity shown in this figure is the difference between the maximum and minimum of the line-integrated conductivity in the simulation box, and normalized by the background conductivity. Dashed and dotted lines are the linear growth rate with and without the effect of the electrical coupling between the conjugate ionospheres, respectively.

Figure 27: Solid line: The evolution of the conductivity perturbations, with 170 m/s eastward wind in the both hemispheres (case B). Dashed line: The evolution of the conductivity perturbations, with 170 m/s eastward wind in the northern hemisphere and 170 m/s westward wind in the southern hemisphere (case C). Dotted line: The evolution of the conductivity perturbations, with 170 m/s eastward wind only in the northern hemisphere (case A).

Figure 28: The linear growth rate of the Perkins instability with the background effective electric field. The effect of the electrical coupling between the conjugate regions is included.

Figure 29: Solid line: The evolution of the conductivity perturbations with weak eastward electric current and 170 m/s eastward wind only in the northern hemisphere (case D). Dashed lines: The maximum and the minimum of the perturbation component of the normalized line-integrated conductivity. Dotted line: The evolution of the conductivity perturbations, with 170 m/s eastward wind only in the northern hemisphere (case A).

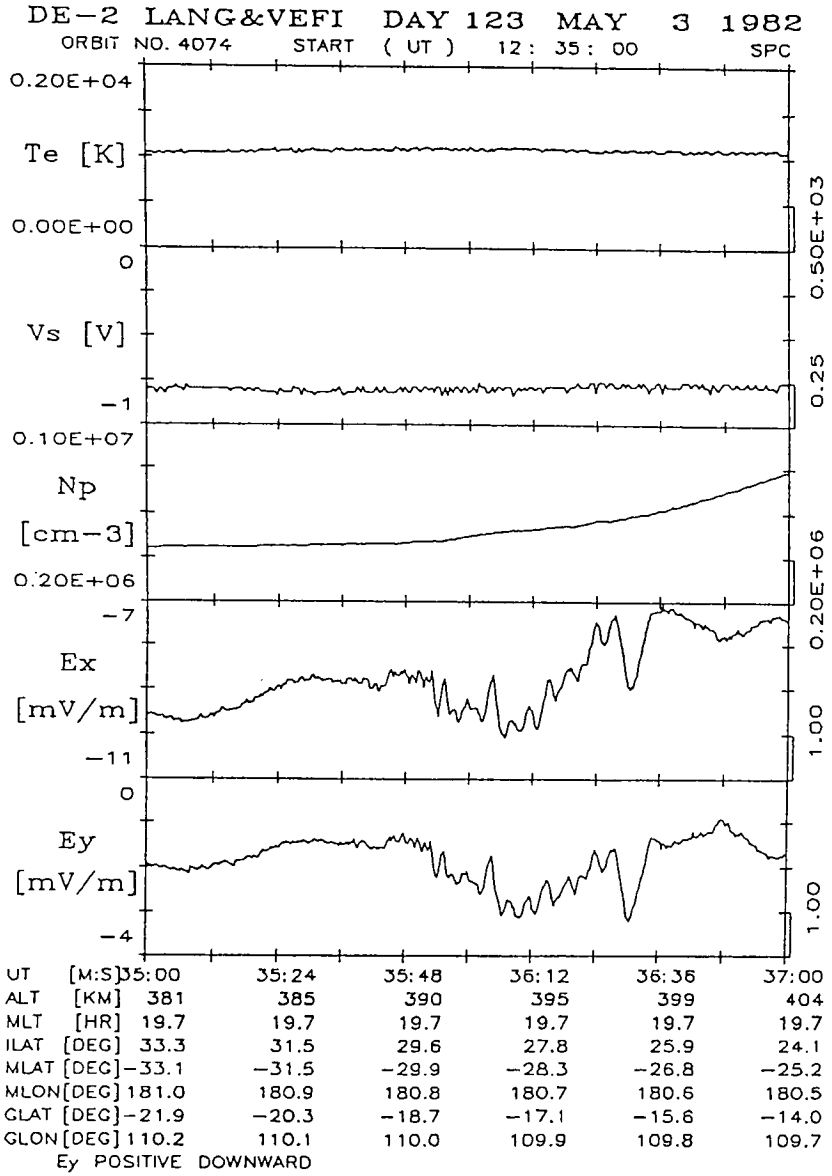

Figure 1 (a).

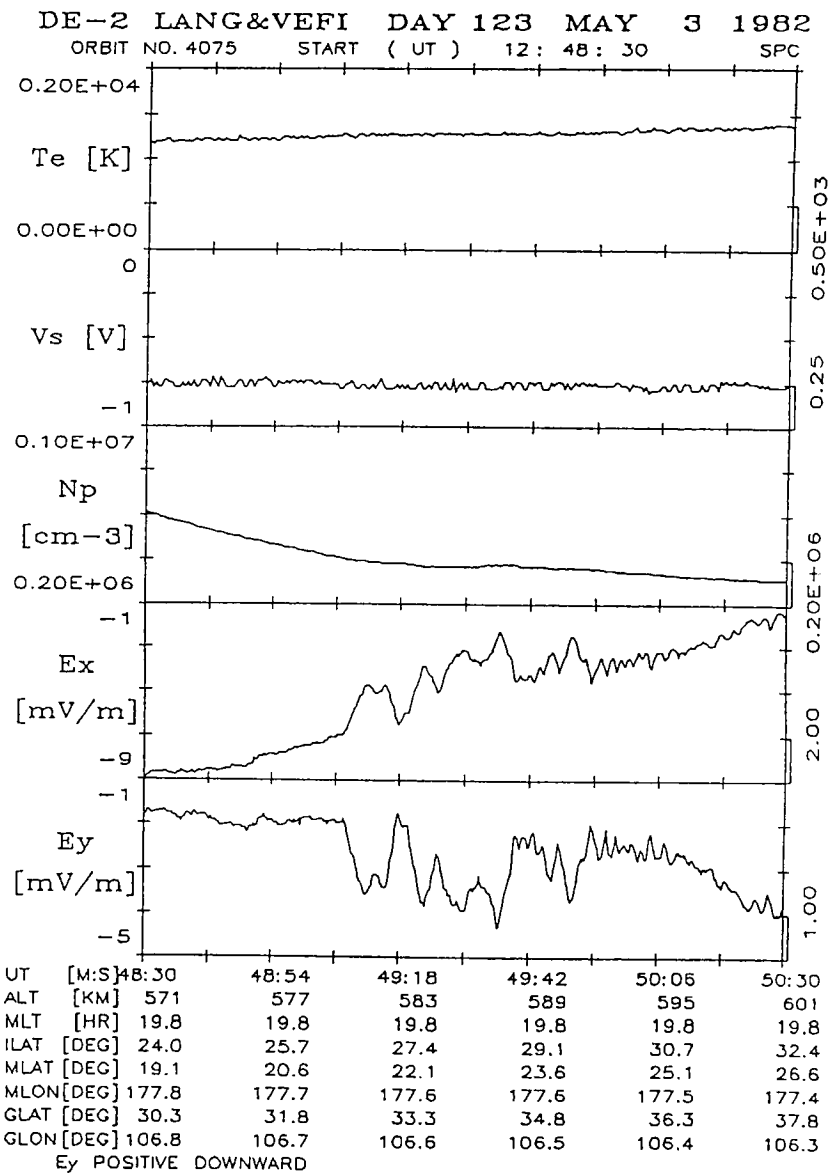

Figure 1 (b).

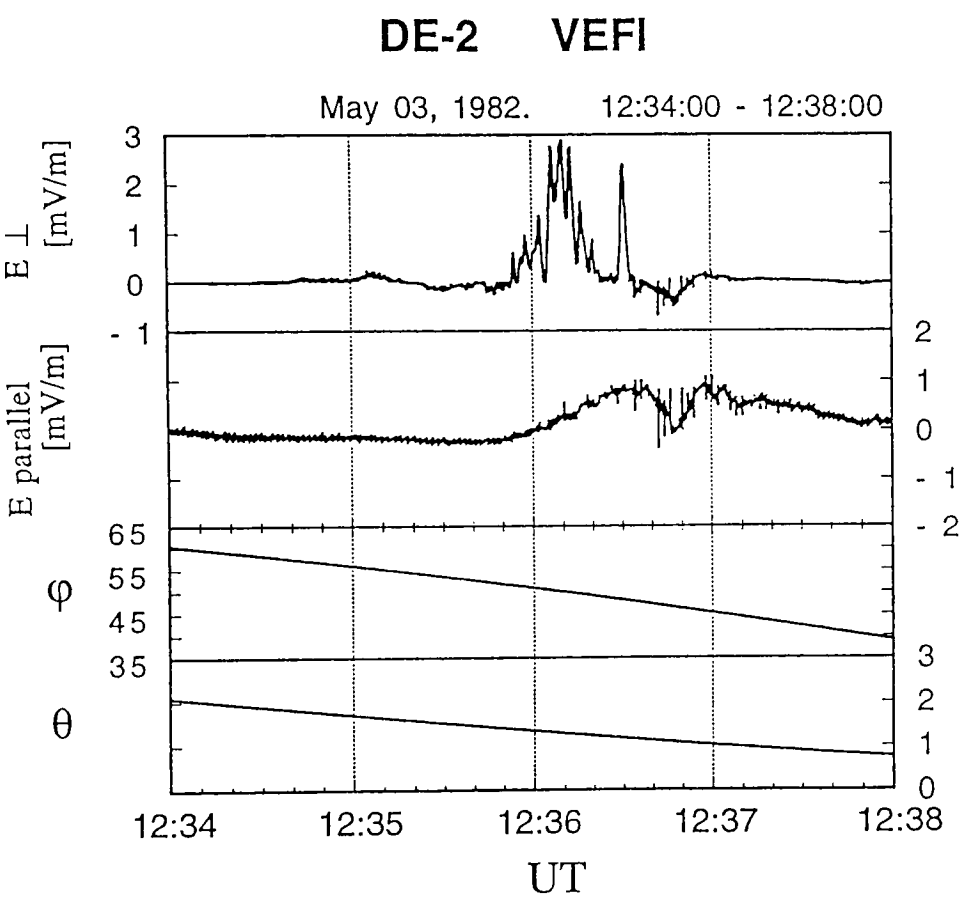

Figure 2 (a).

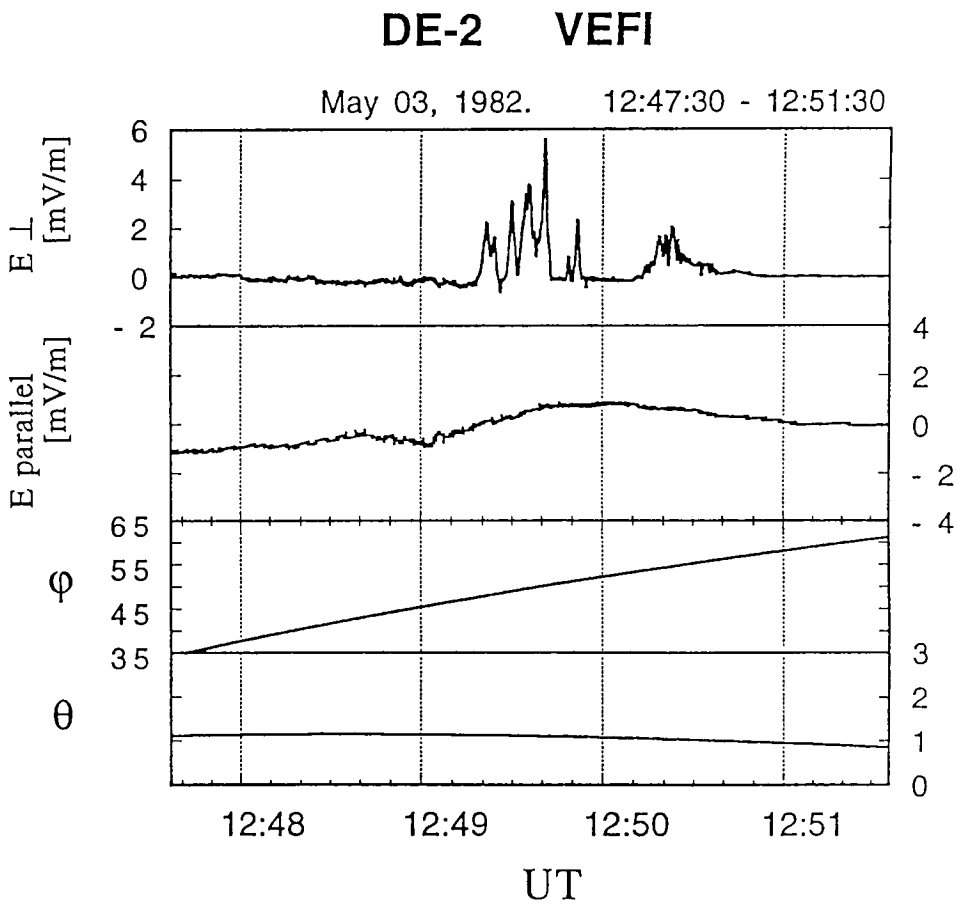

Figure 2 (b).

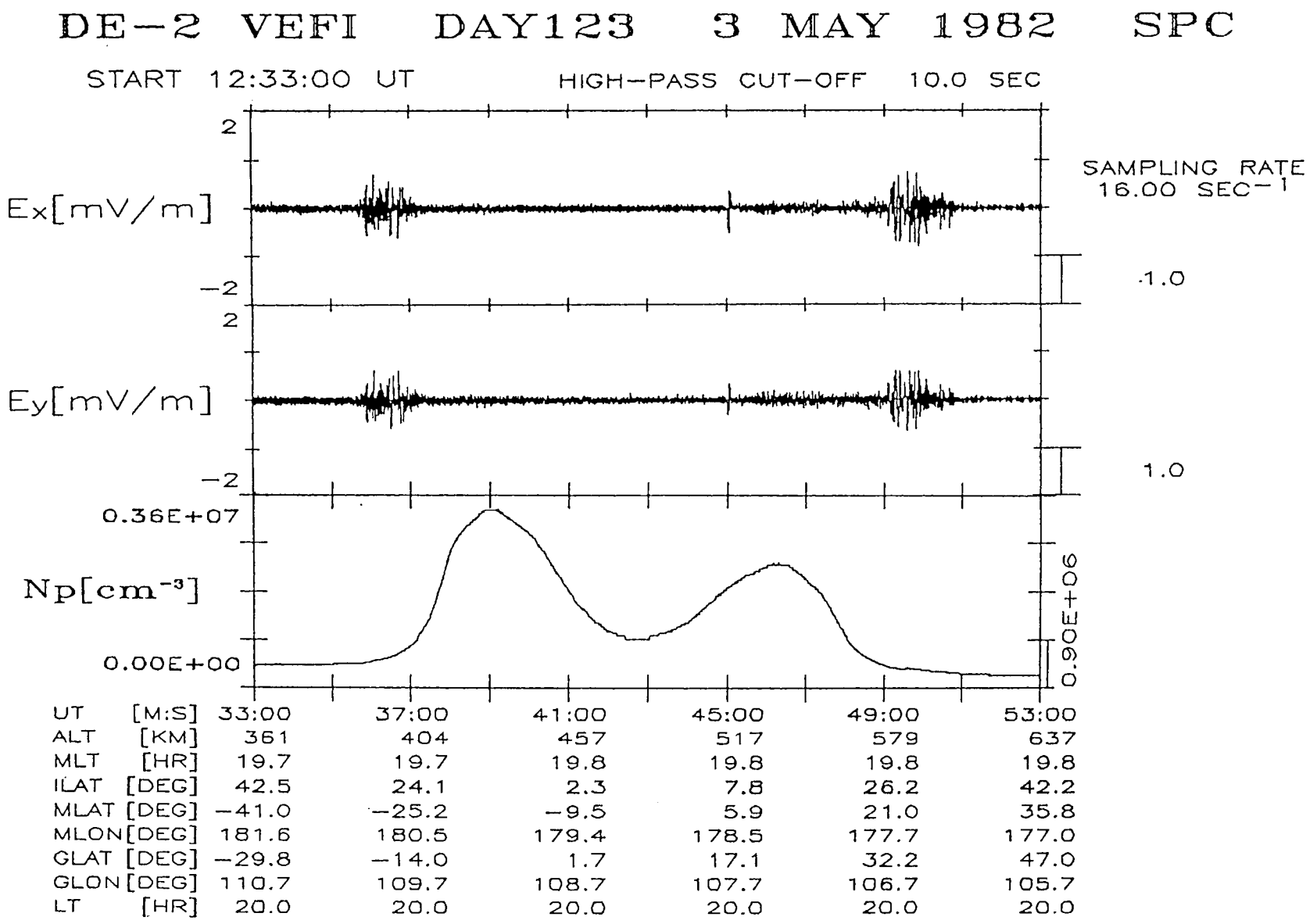
DE-2 VEFI DAY123 3 MAY 1982 SPC
START 12:33:00 UT
HIGH-PASS CUT-OFF 10.0 SEC
SAMPLING RATE
16.00 SEC-1
Ex[mV/m]
2
-2
1.0
Ey[mV/m]
2
-2
1.0
Np[cm-3]
0.36E+07
0.00E+00
0.90E+06
UT [M:S] 33:00 37:00 41:00 45:00 49:00 53:00
ALT [KM] 361 404 457 517 579 637
MLT [HR] 19.7 19.7 19.8 19.8 19.8 19.8
ILAT [DEG] 42.5 24.1 2.3 7.8 26.2 42.2
MLAT [DEG] -41.0 -25.2 -9.5 5.9 21.0 35.8
MLON [DEG] 181.6 180.5 179.4 178.5 177.7 177.0
GLAT [DEG] -29.8 -14.0 1.7 17.1 32.2 47.0
GLON [DEG] 110.7 109.7 108.7 107.7 106.7 105.7
LT [HR] 20.0 20.0 20.0 20.0 20.0 20.0

Figure 3.

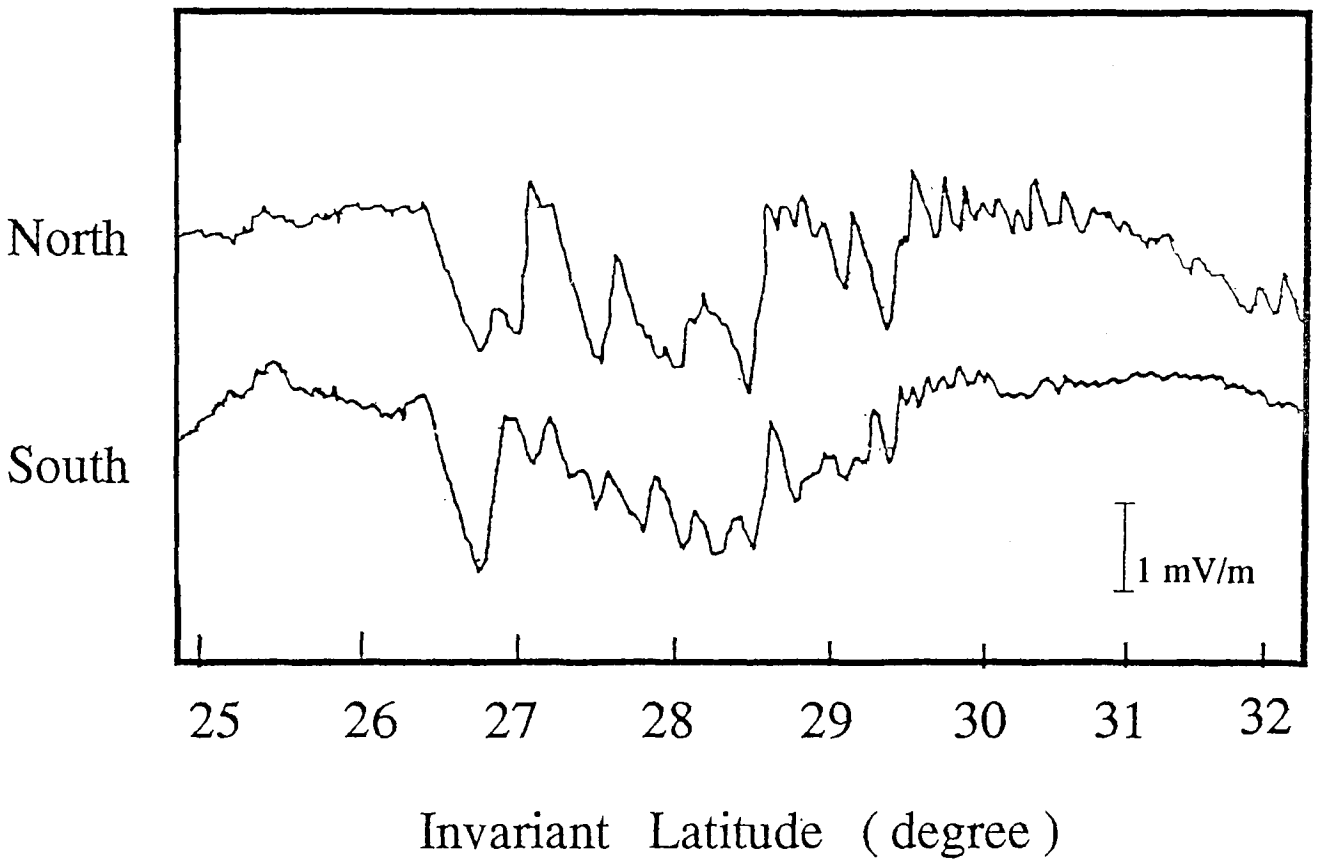
North
South
1 mV/m
25
26
27
28
29
30
31
32
Invariant Latitude (degree)

Figure 4.

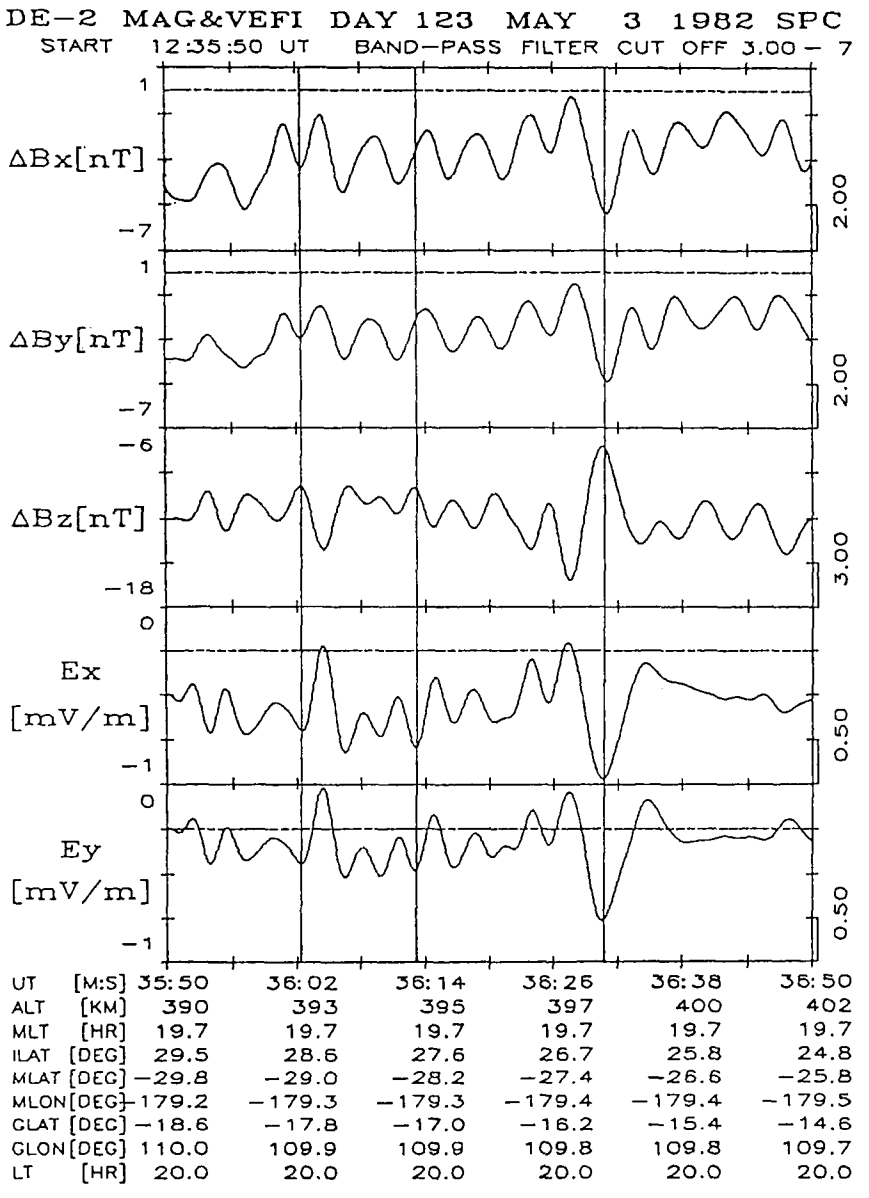

Figure 5 (a).

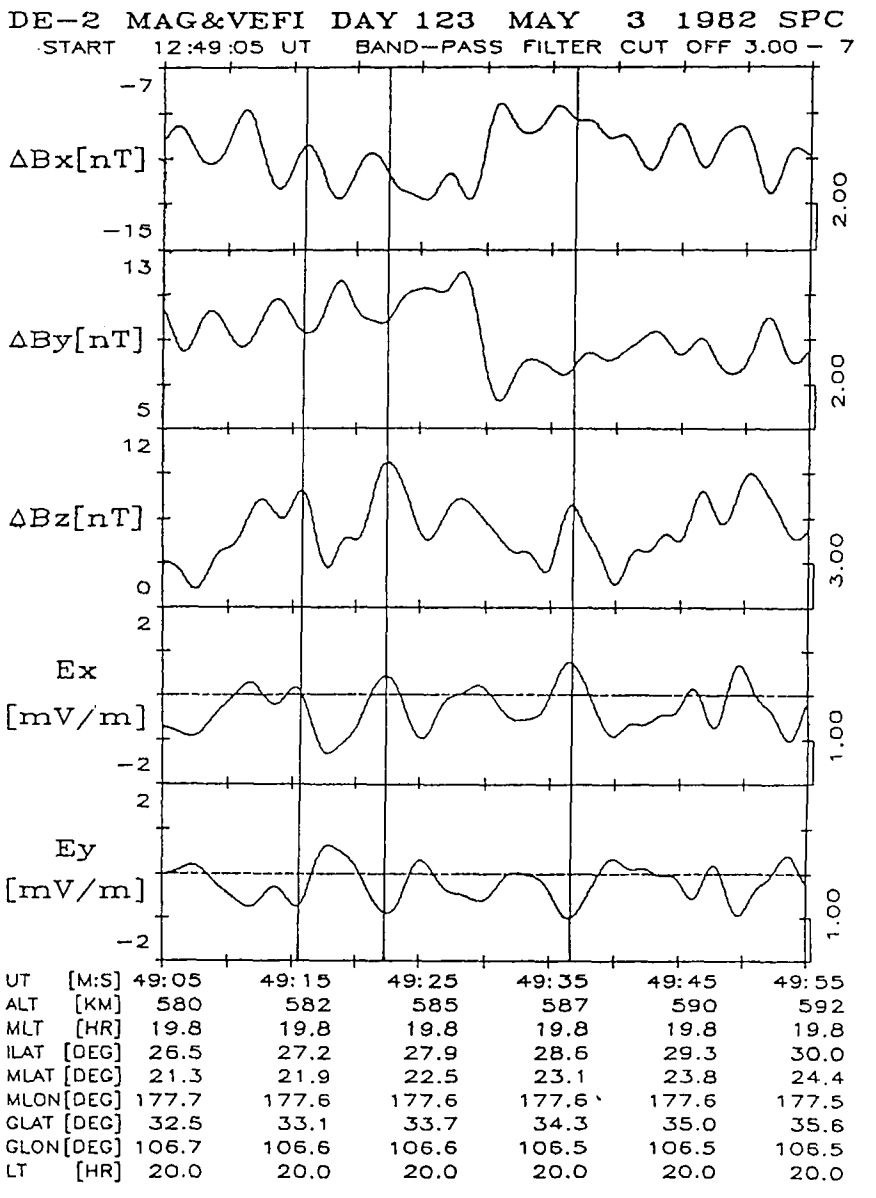

Figure 5 (b).

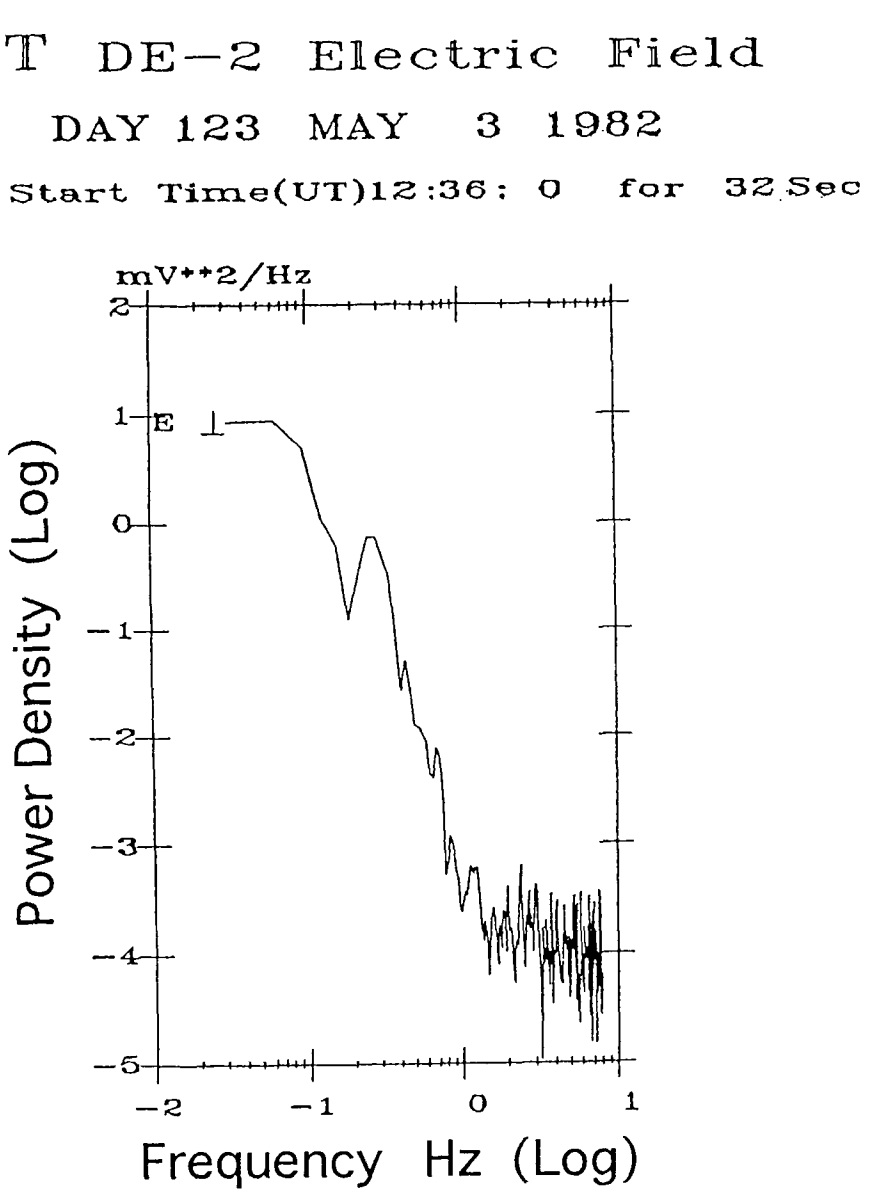

Figure 6 (a).

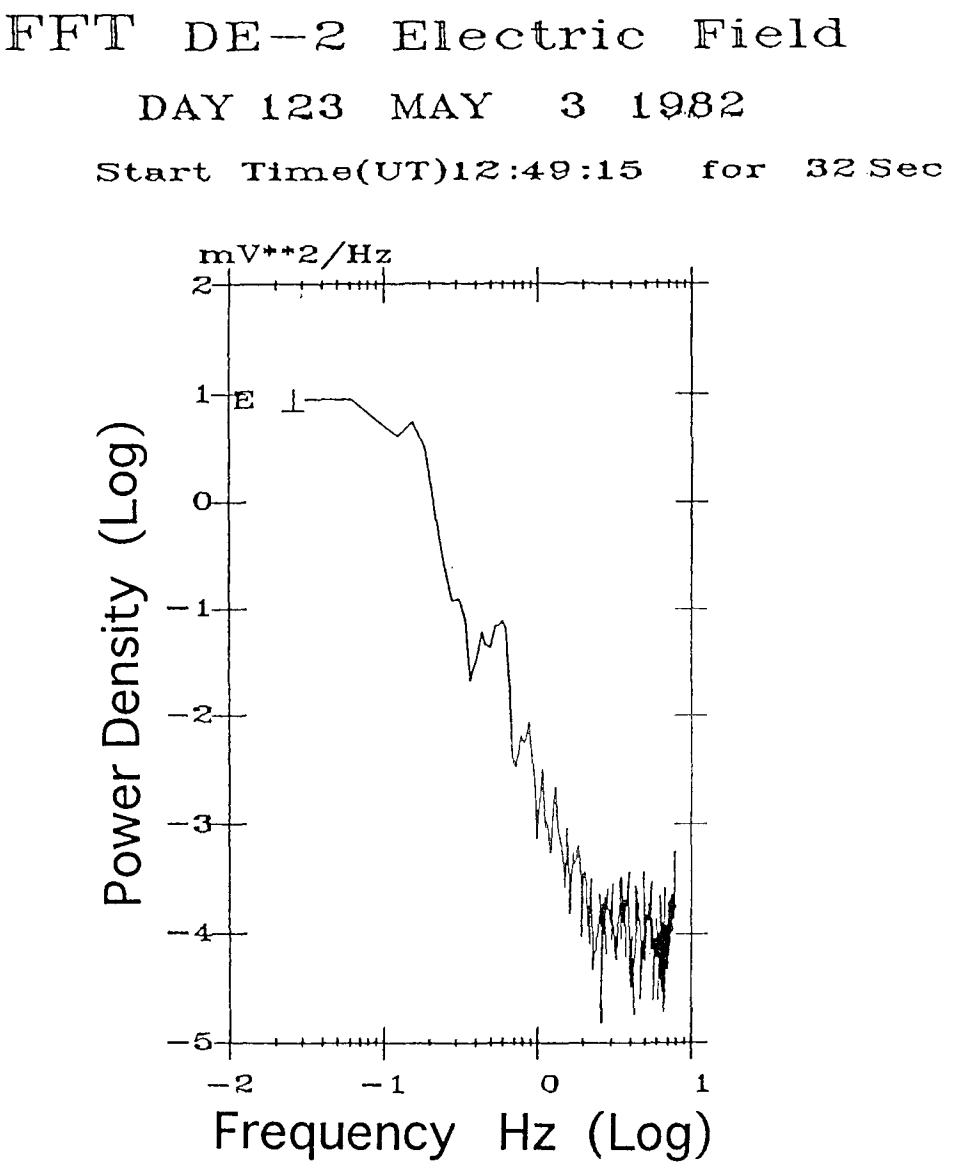

Figure 6 (b).

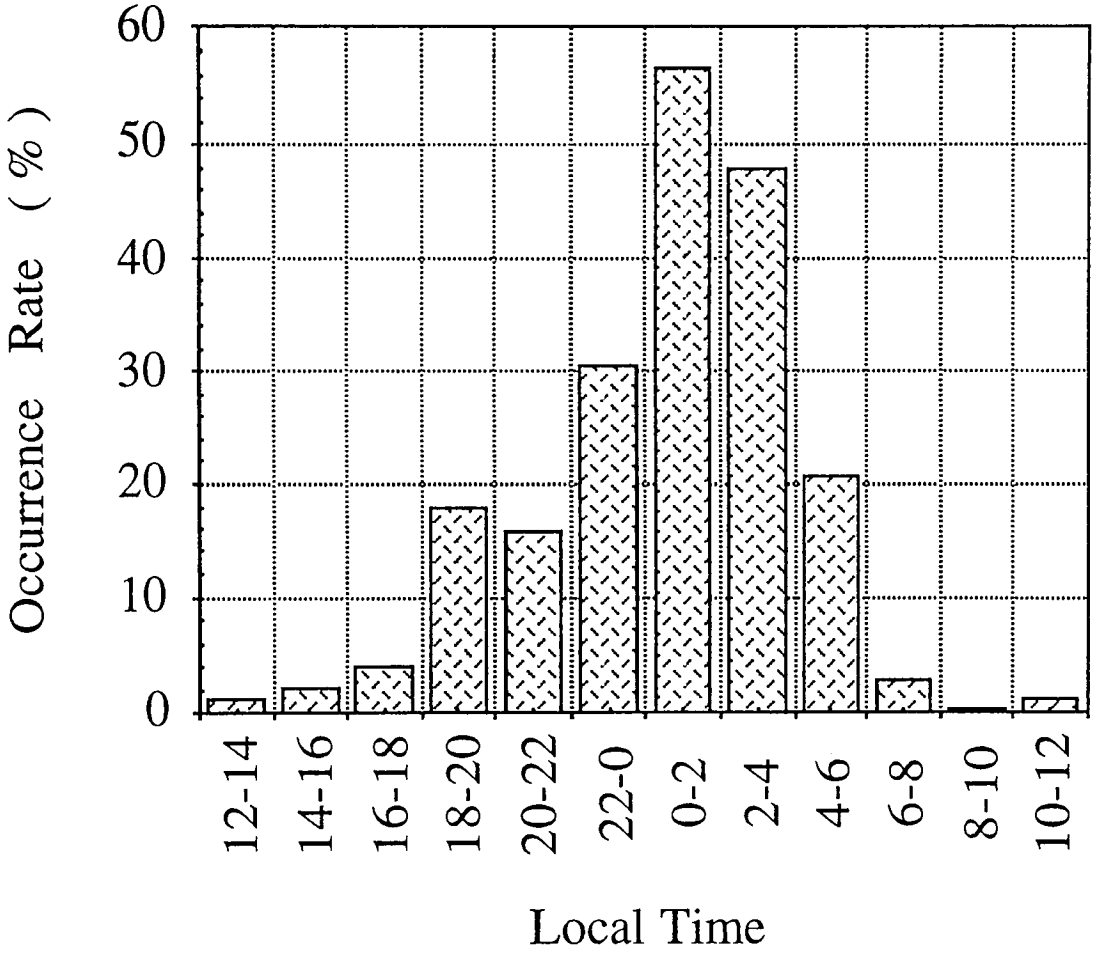
60
50
40
30
20
10
0
Occurrence Rate (%)
12-14
14-16
16-18
18-20
20-22
22-0
0-2
2-4
4-6
6-8
8-10
10-12
Local Time

Figure 7.

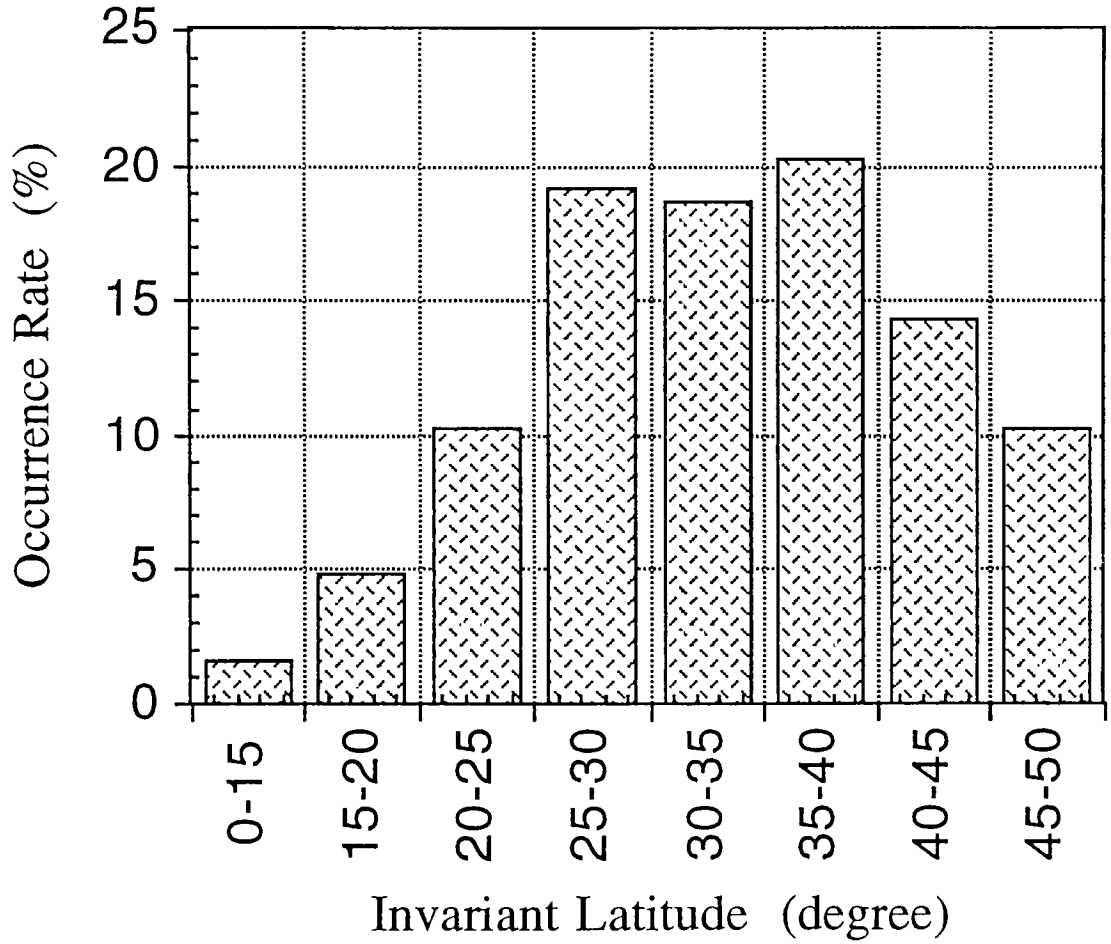
25
20
15
10
5
0
Occurrence Rate (%)
0-15
15-20
20-25
25-30
30-35
35-40
40-45
45-50
Invariant Latitude (degree)

Figure 8.

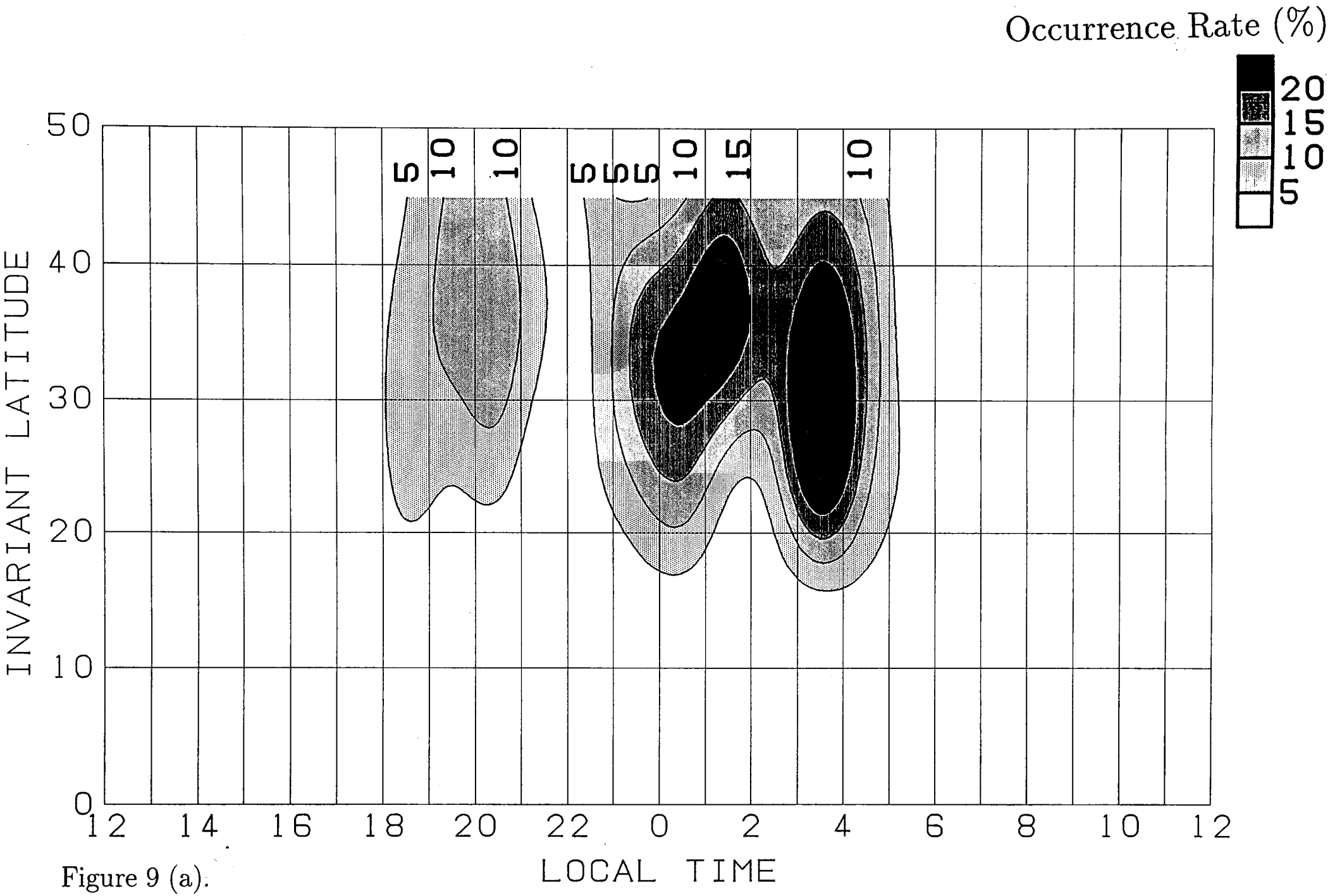
Occurrence Rate (%)
20
15
10
5
INVARIANT LATITUDE
50
40
30
20
10
0
5
10
10
5
5
5
10
15
10
12
14
16
18
20
22
0
2
4
6
8
10
12
LOCAL TIME

Figure 9 (a).

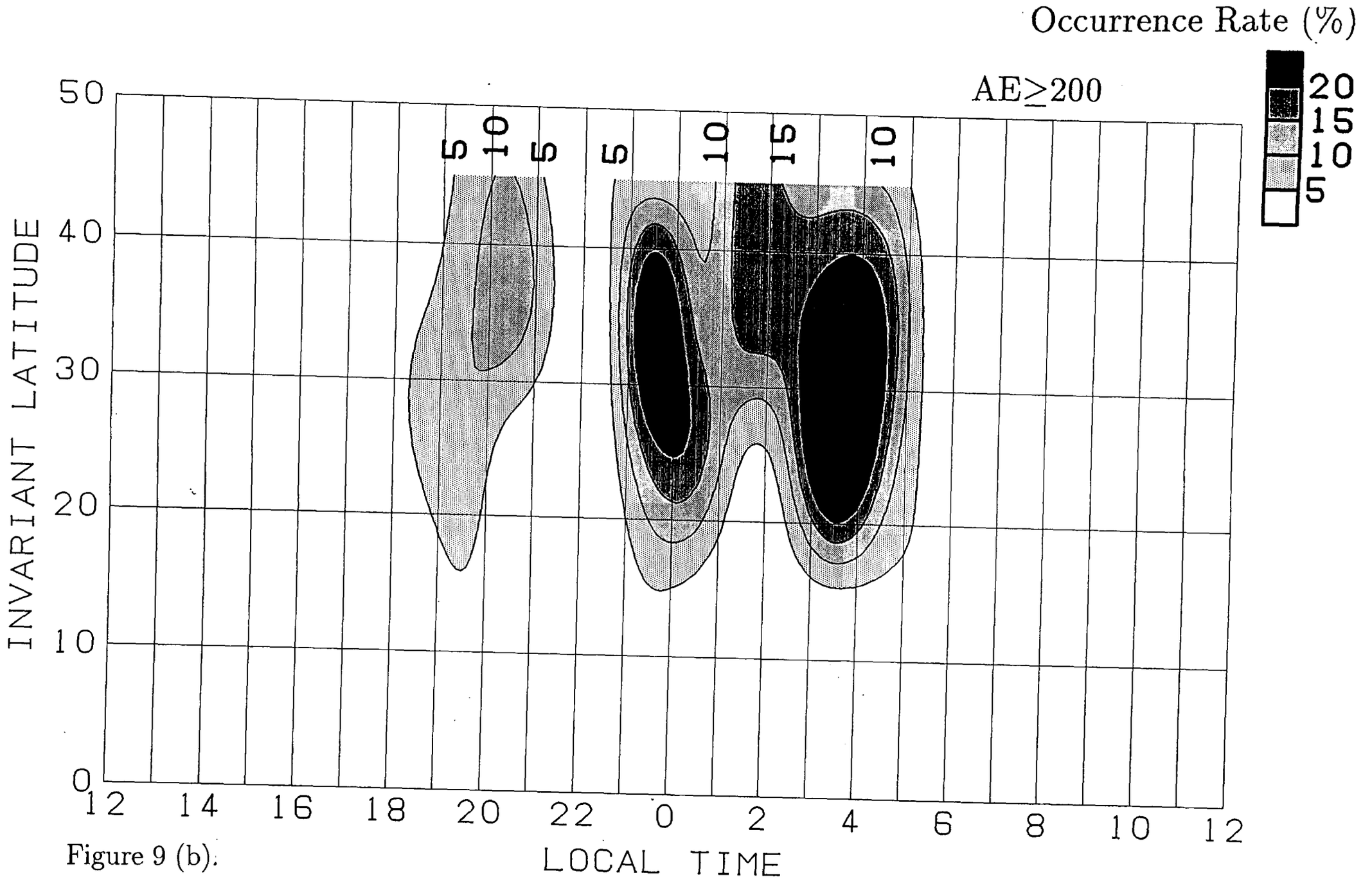
Occurrence Rate (%)
20
15
10
5
AE≥200
5
10
5
5
10
15
10
INVARIANT LATITUDE
50
40
30
20
10
0
12
14
16
18
20
22
0
2
4
6
8
10
12
LOCAL TIME

Figure 9 (b).

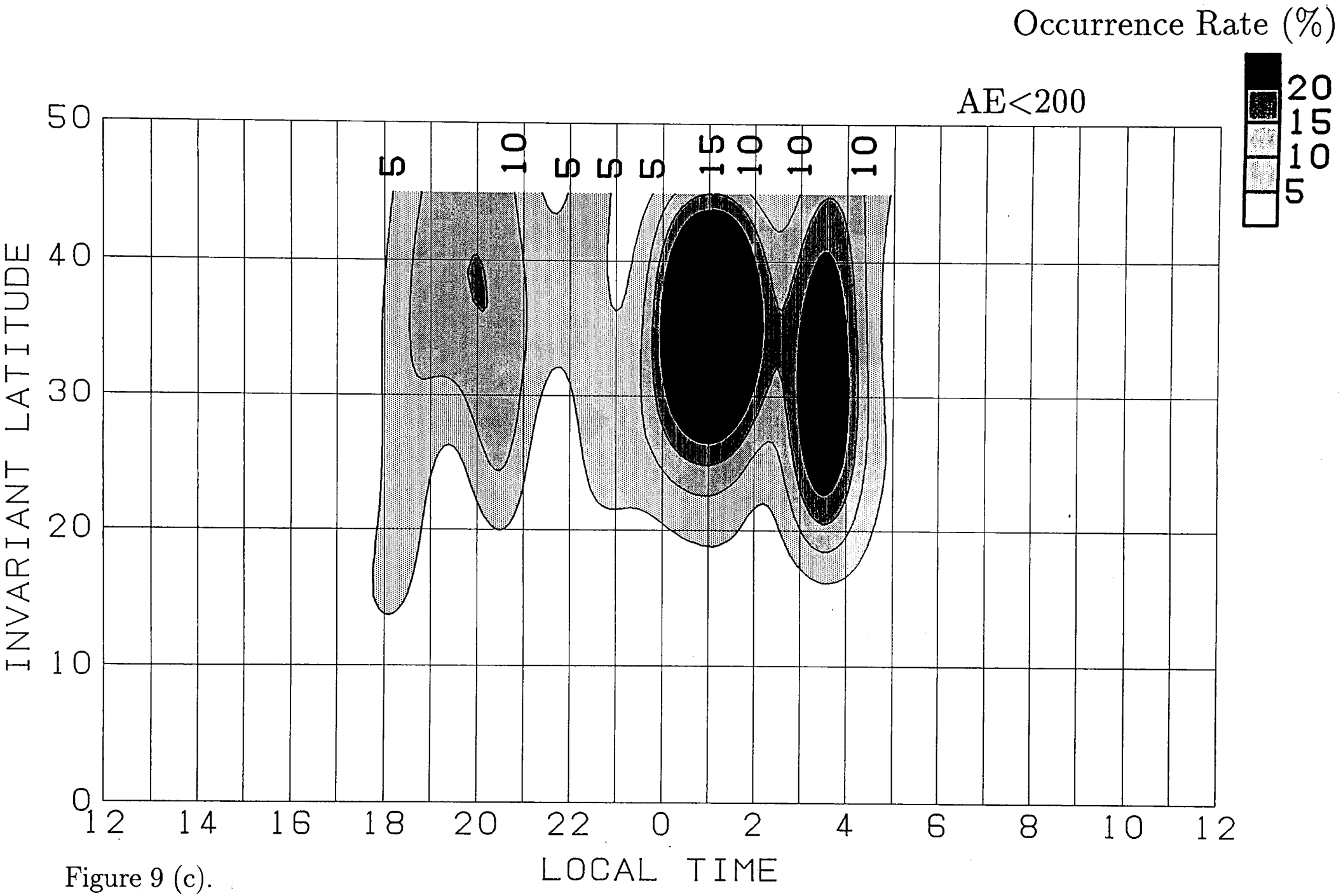
Occurrence Rate (%)
20
15
10
5
AE<200
5
10
5
5
5
15
10
10
10
INVARIANT LATITUDE
50
40
30
20
10
0
12
14
16
18
20
22
0
2
4
6
8
10
12
LOCAL TIME

Figure 9 (c).

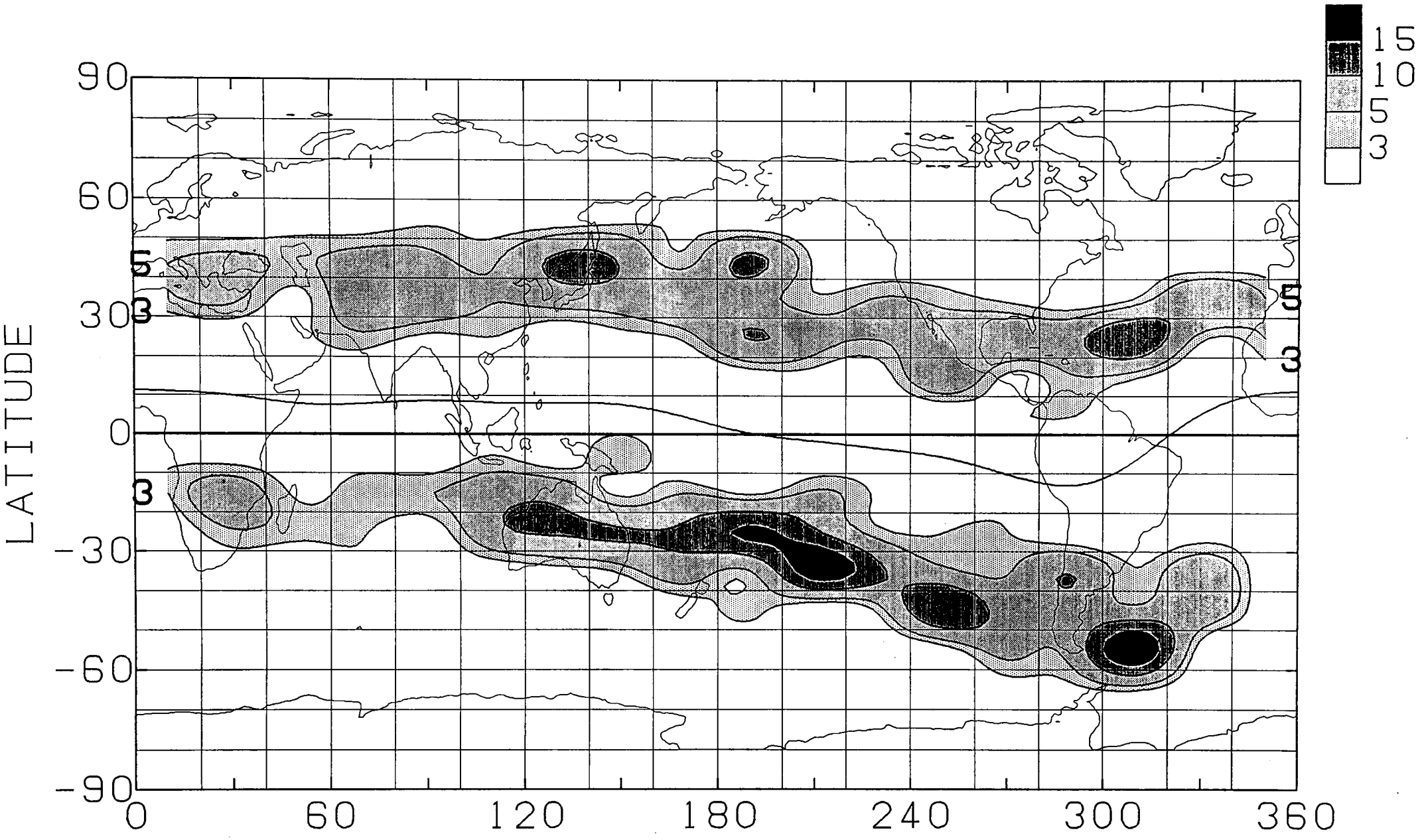
15
10
5
3
90
60
30
0
-30
-60
-90
LATITUDE
0
60
120
180
240
300
360
GEOGRAPHIC LONGITUDE

Figure 10.

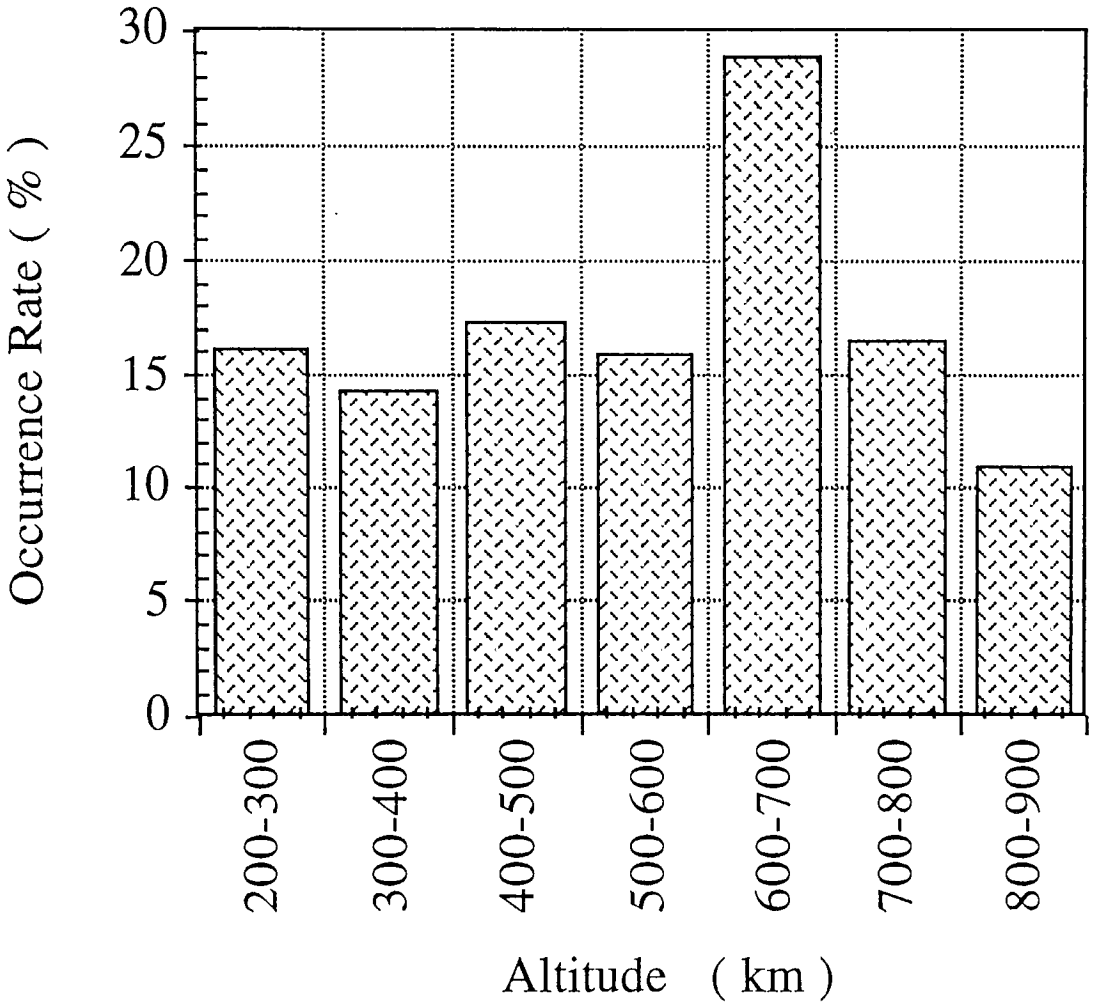
30
25
20
15
10
5
0
Occurrence Rate (%)
200-300
300-400
400-500
500-600
600-700
700-800
800-900
Altitude (km)

Figure 11.

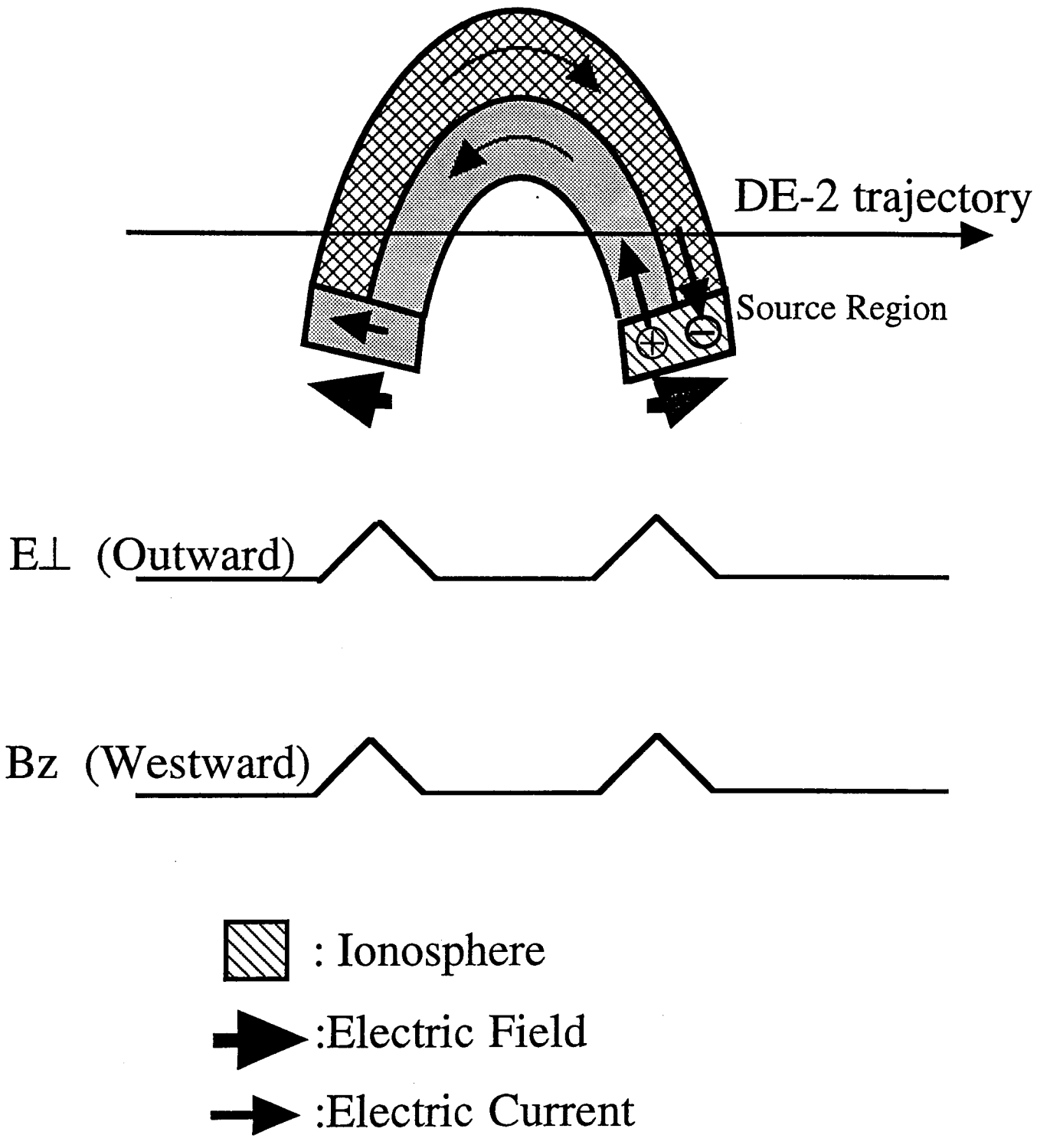
DE-2 trajectory
Source Region
E⊥ (Outward)
Bz (Westward)
: Ionosphere
:Electric Field
:Electric Current

Figure 12.

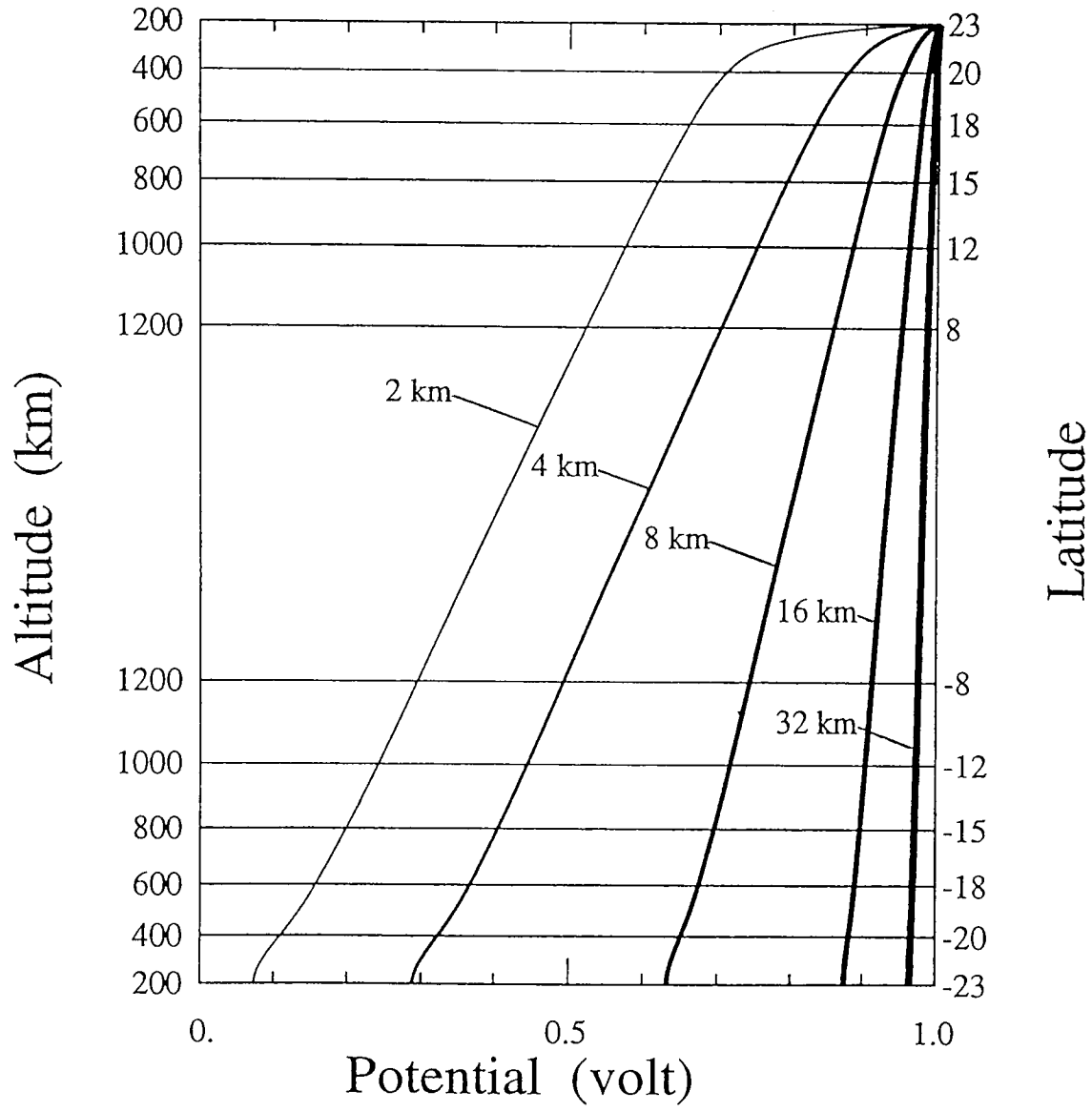
200
400
600
800
1000
1200
1200
1000
800
600
400
200
23
20
18
15
12
8
-8
-12
-15
-18
-20
-23
2 km
4 km
8 km
16 km
32 km
0.
0.5
1.0
Potential (volt)
Altitude (km)
Latitude

Figure 13.

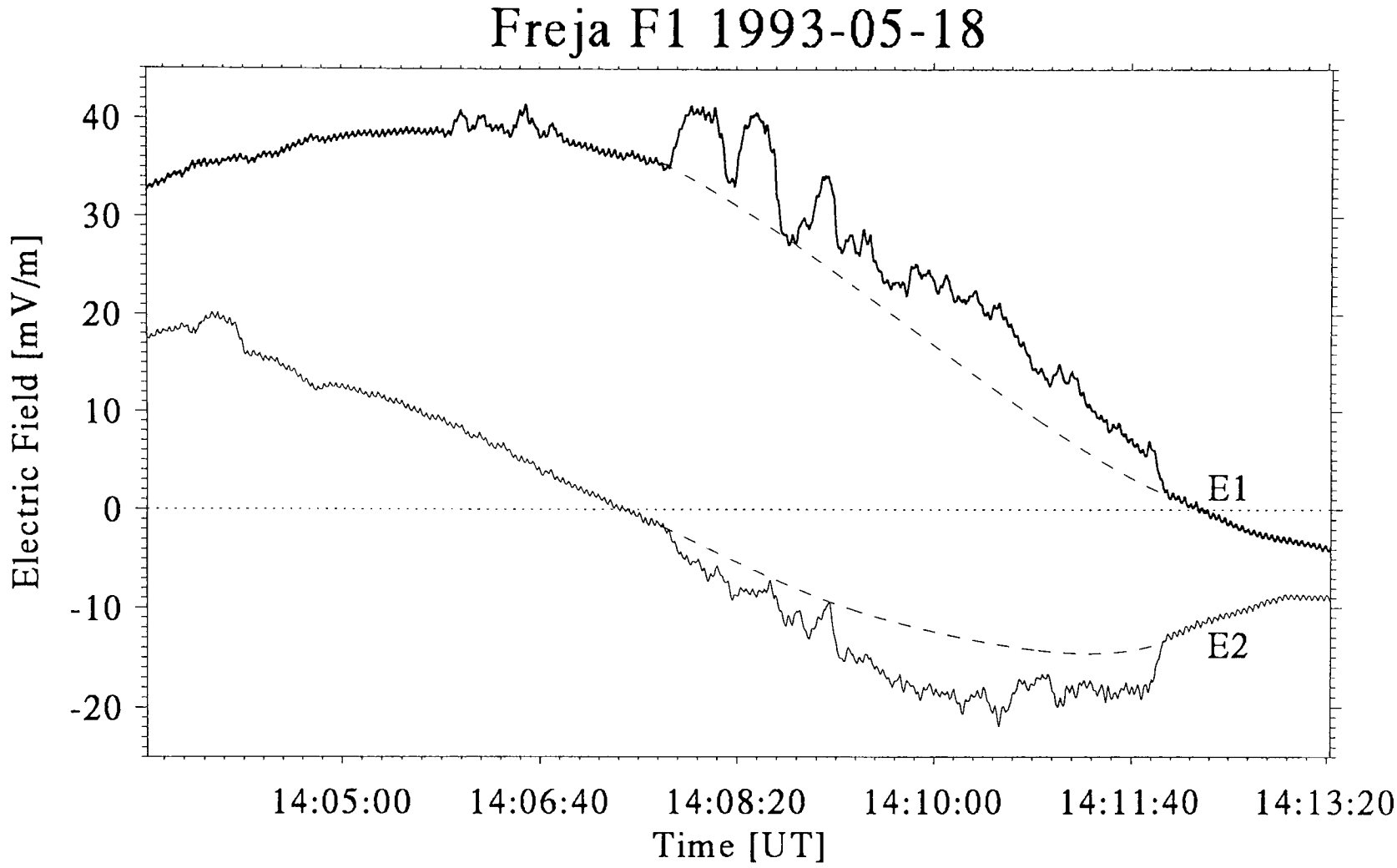
Freja F1 1993-05-18
Electric Field [mV/m]
40
30
20
10
0
-10
-20
E1
E2
14:05:00
14:06:40
14:08:20
14:10:00
14:11:40
14:13:20
Time [UT]

Figure 14.

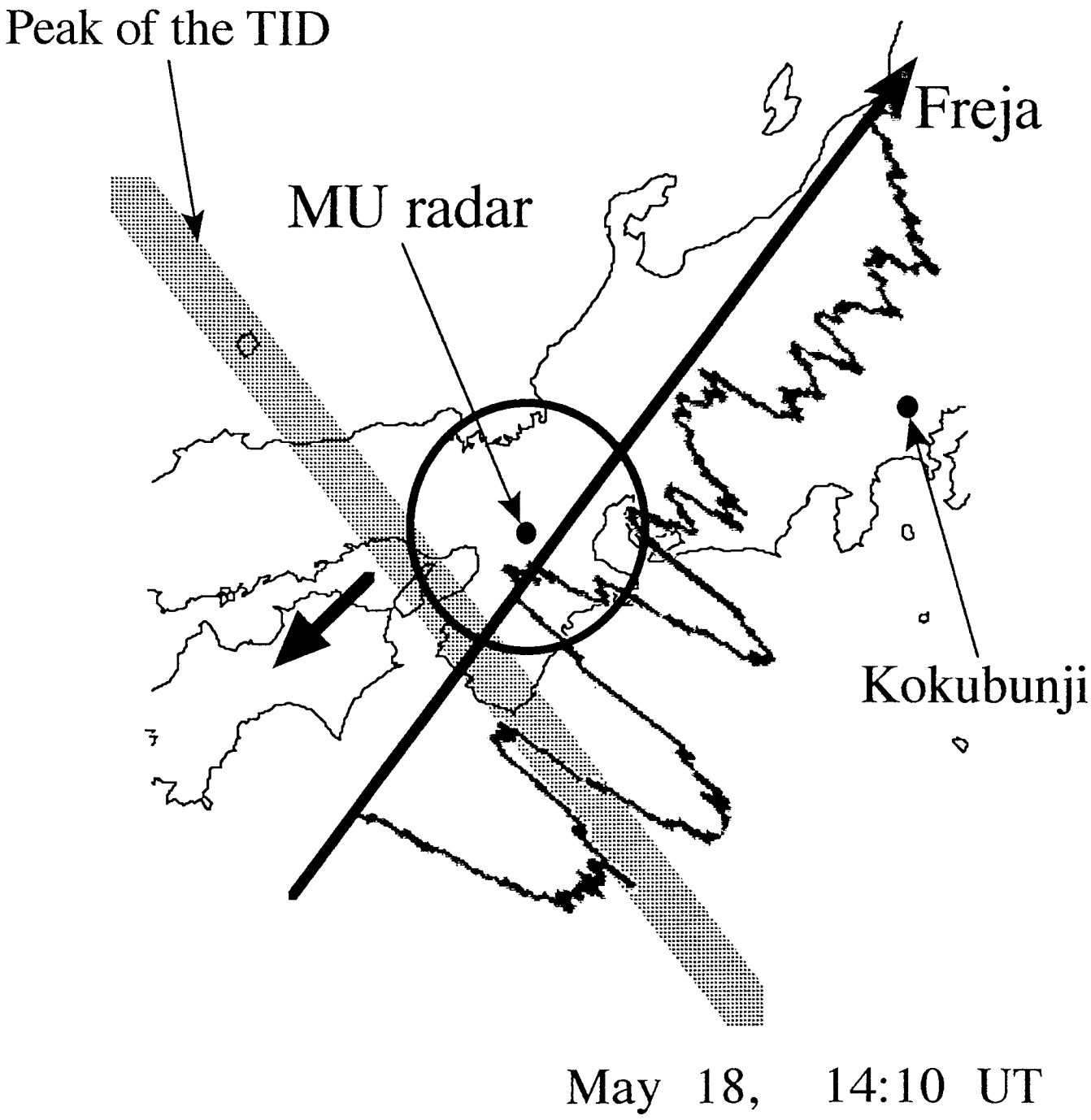

Figure 15.

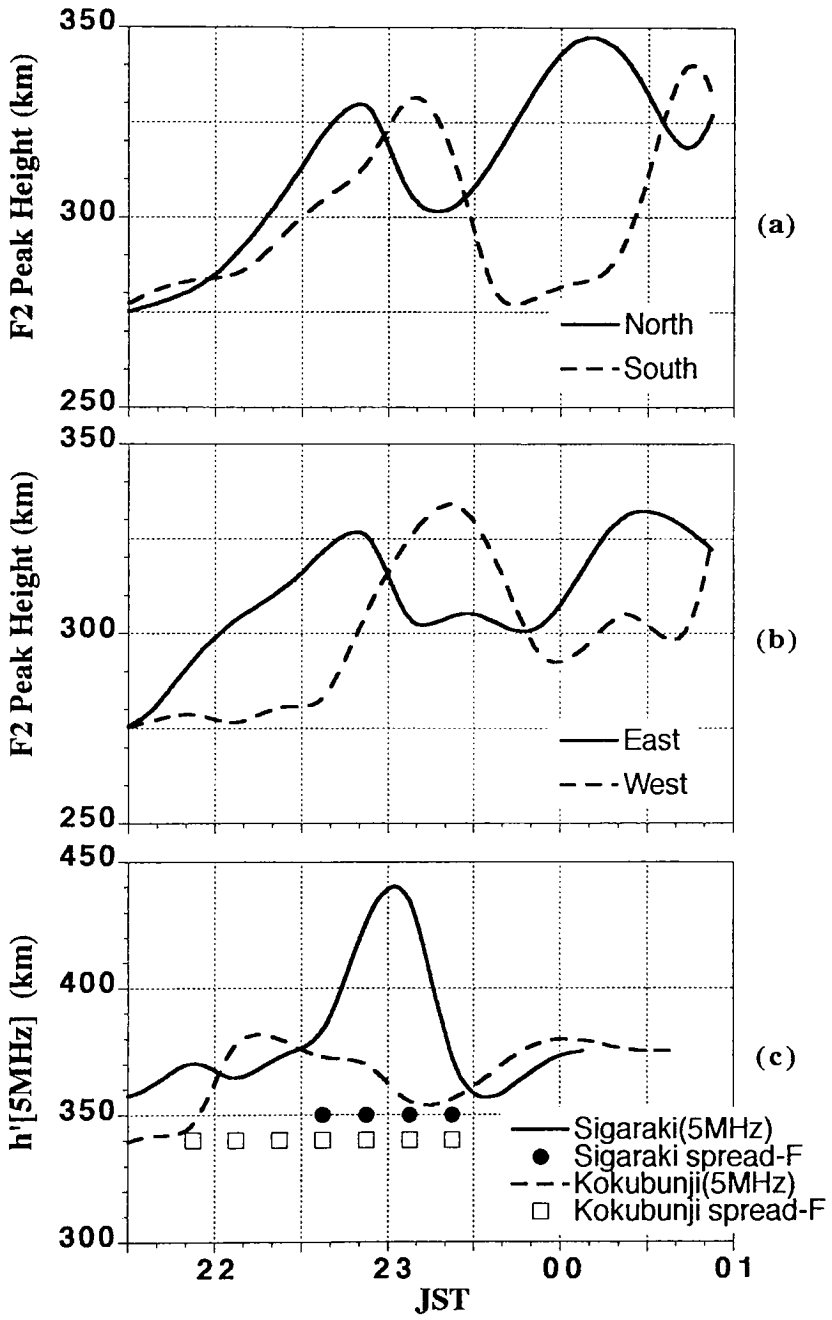
350
300
250
F2 Peak Height (km)
(a)
North
South
350
300
250
F2 Peak Height (km)
(b)
East
West
450
400
350
300
h'[5MHz] (km)
(c)
Sigaraki(5MHz)
Sigaraki spread-F
Kokubunji(5MHz)
Kokubunji spread-F
22
23
00
01
JST

Figure 16.

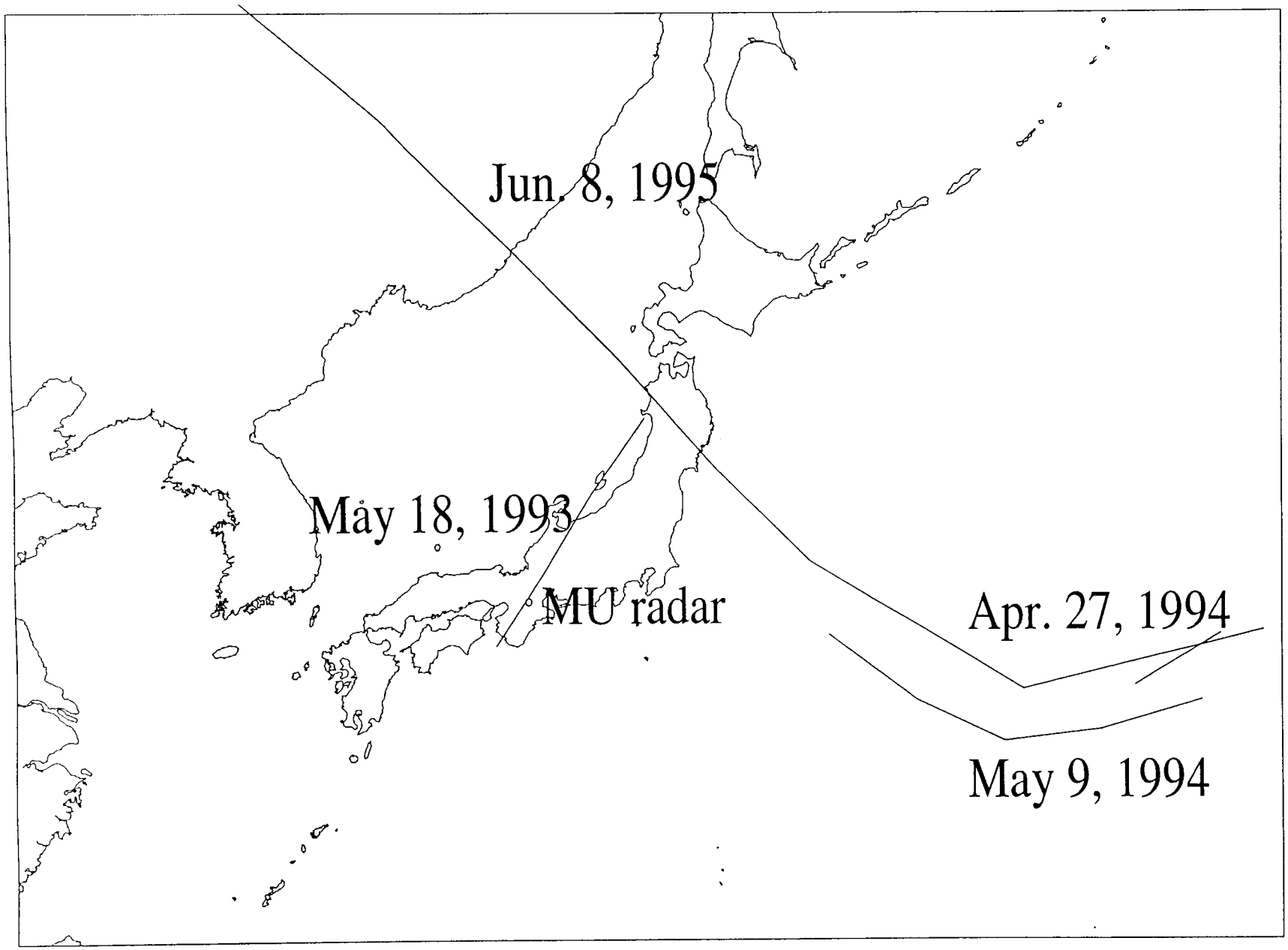

Figure 17.

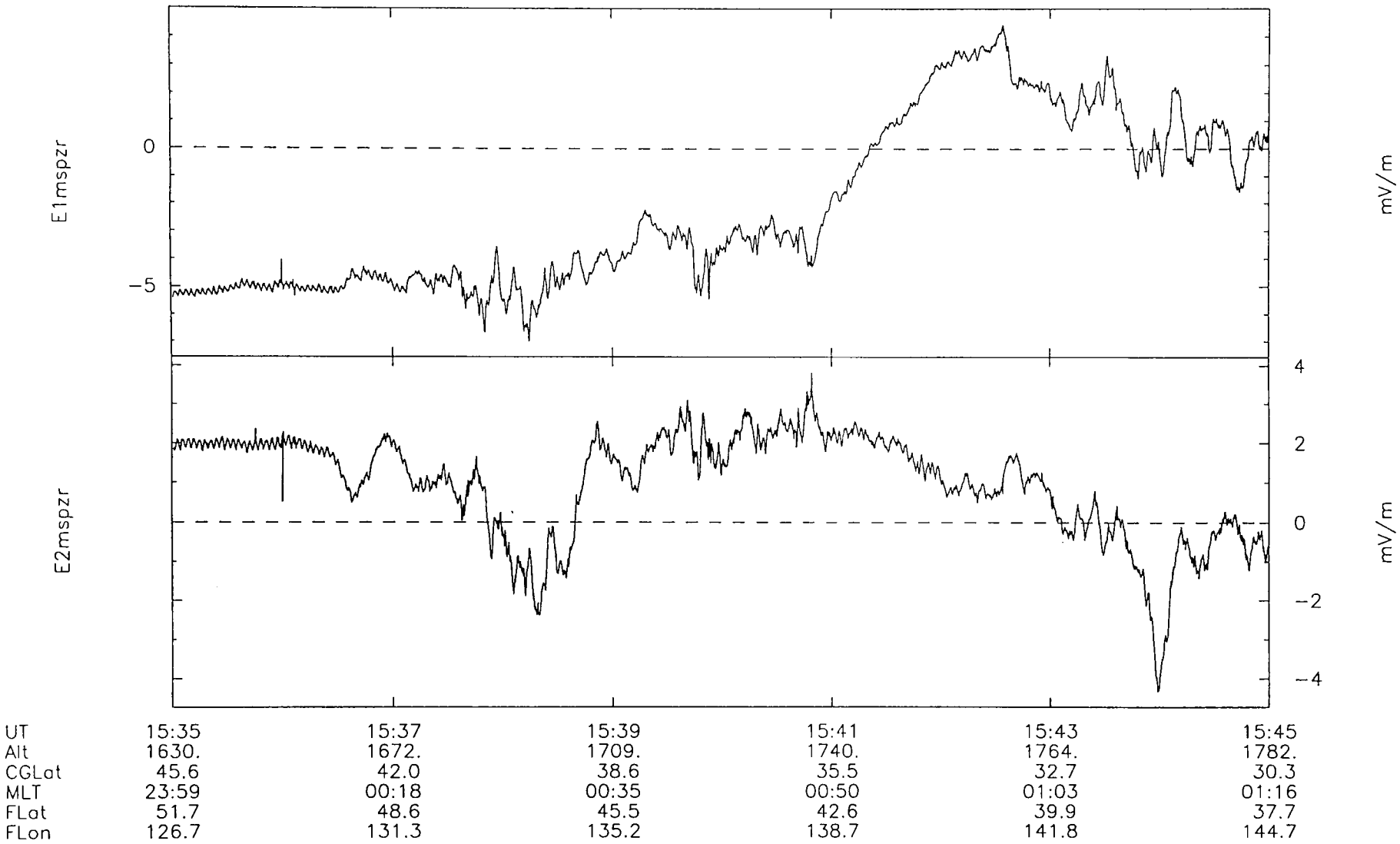
Freja F1 data 1995-06-08
Orbit 12891
E1mspzr
0
-5
mV/m
E2mspzr
4
2
0
-2
-4
mV/m
UT 15:35 15:37 15:39 15:41 15:43 15:45
Alt 1630. 1672. 1709. 1740. 1764. 1782.
CGLat 45.6 42.0 38.6 35.5 32.7 30.3
MLT 23:59 00:18 00:35 00:50 01:03 01:16
FLat 51.7 48.6 45.5 42.6 39.9 37.7
FLon 126.7 131.3 135.2 138.7 141.8 144.7

Figure 18.

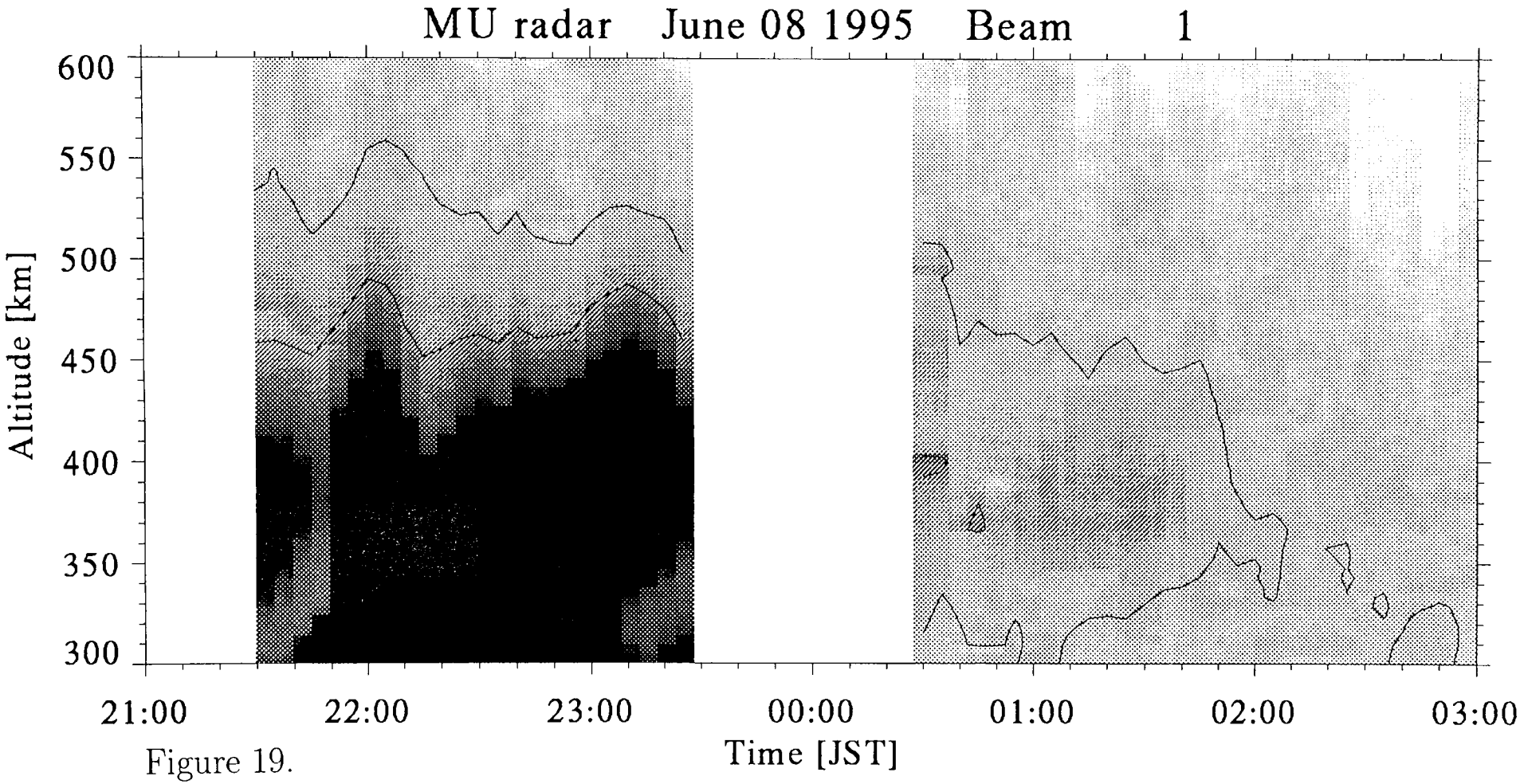
MU radar June 08 1995 Beam 1
600
550
500
450
400
350
300
Altitude [km]
21:00
22:00
23:00
00:00
01:00
02:00
03:00
Time [JST]

Figure 19.

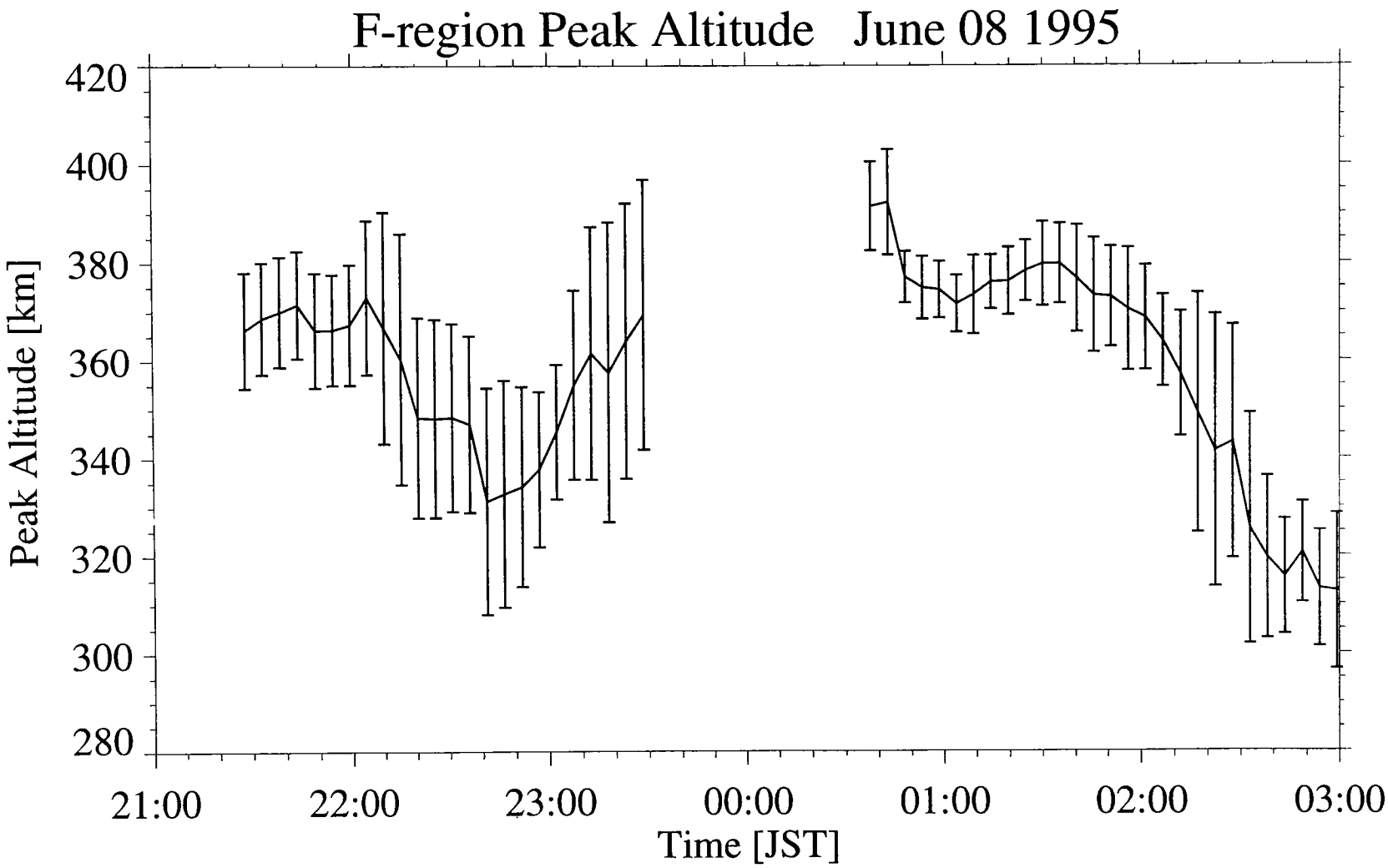
F-region Peak Altitude June 08 1995
Peak Altitude [km]
420
400
380
360
340
320
300
280
21:00
22:00
23:00
00:00
01:00
02:00
03:00
Time [JST]

Figure 20.

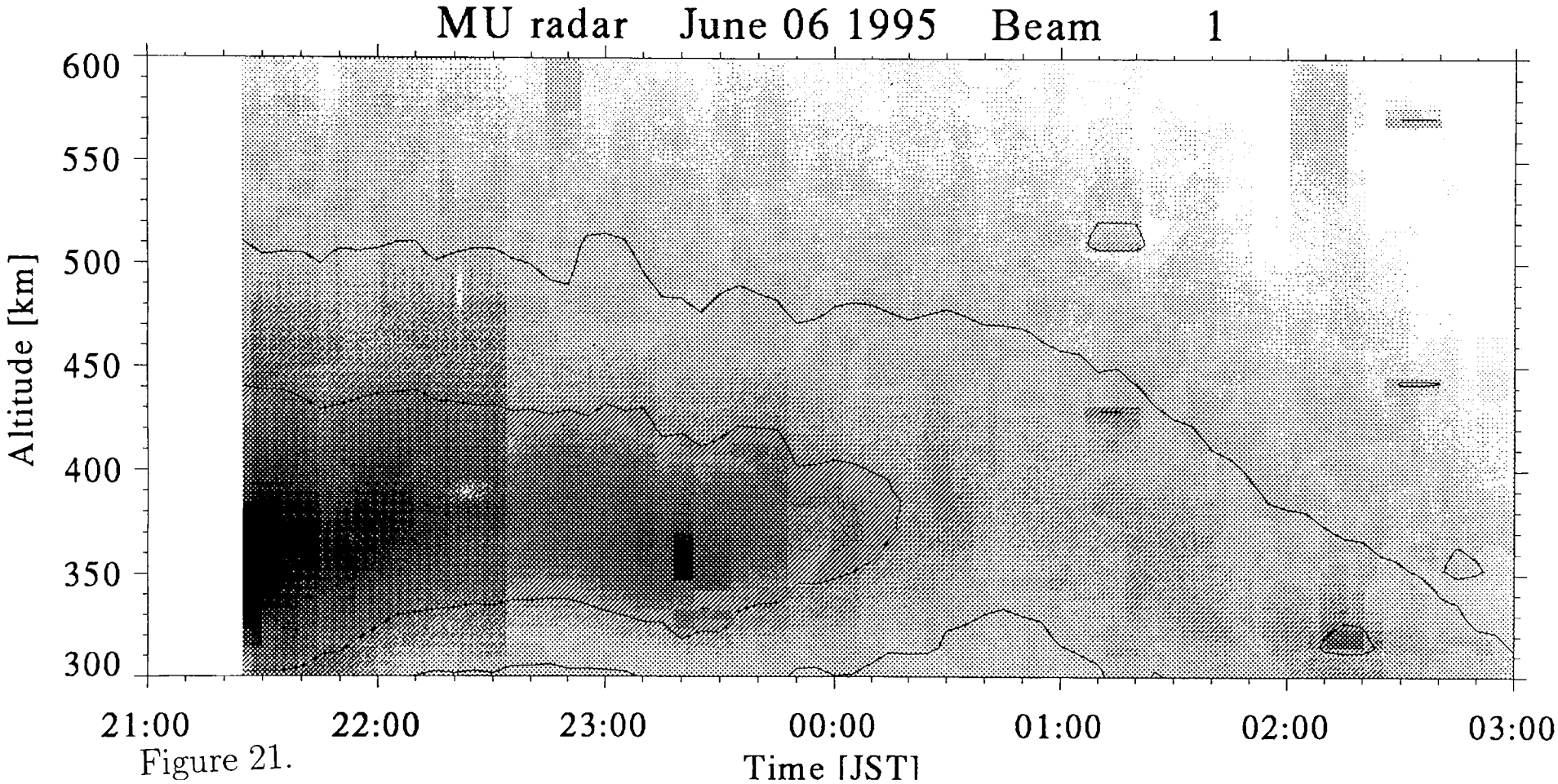
MU radar June 06 1995 Beam 1
600
550
500
450
400
350
300
Altitude [km]
21:00
22:00
23:00
00:00
01:00
02:00
03:00
Time [JST]

Figure 21.

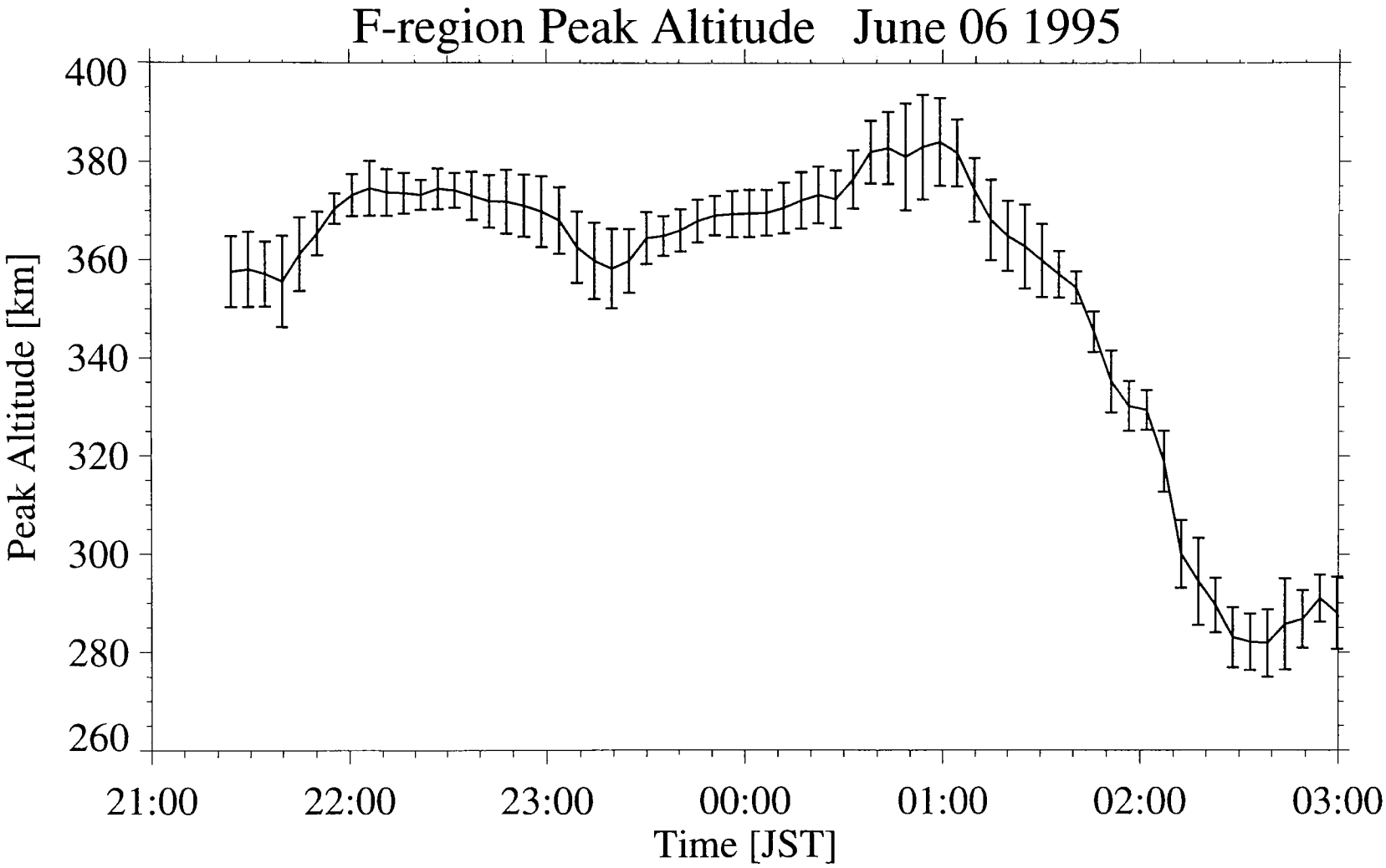
F-region Peak Altitude June 06 1995
Peak Altitude [km]
400
380
360
340
320
300
280
260
21:00
22:00
23:00
00:00
01:00
02:00
03:00
Time [JST]

Figure 22.

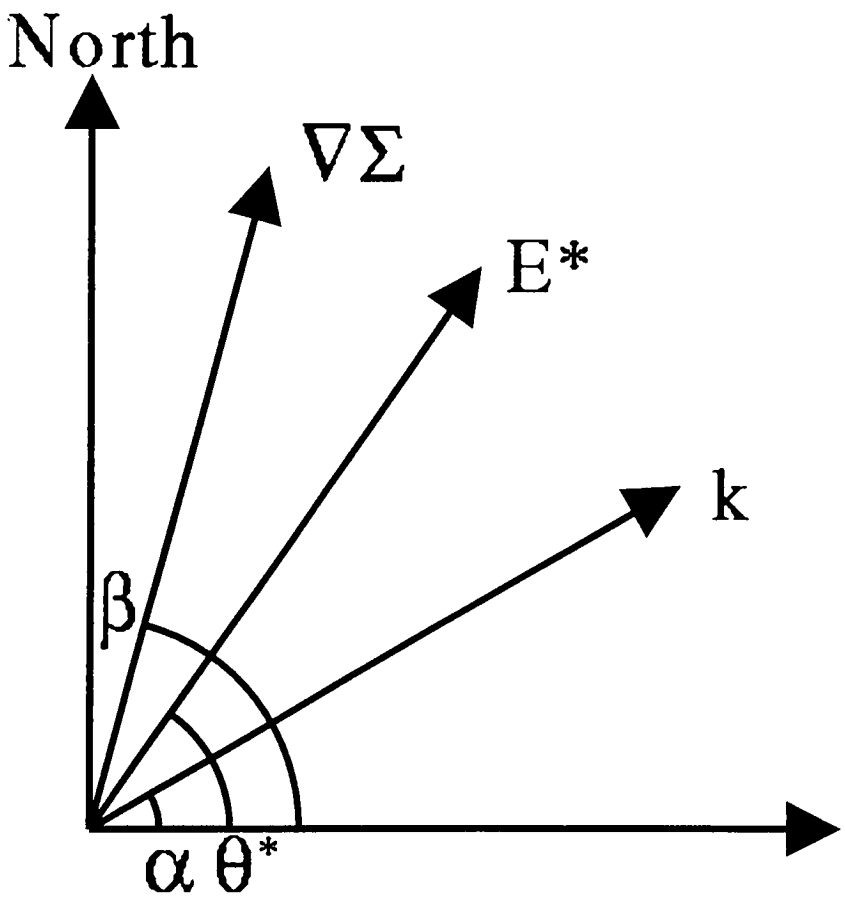

Figure 23.

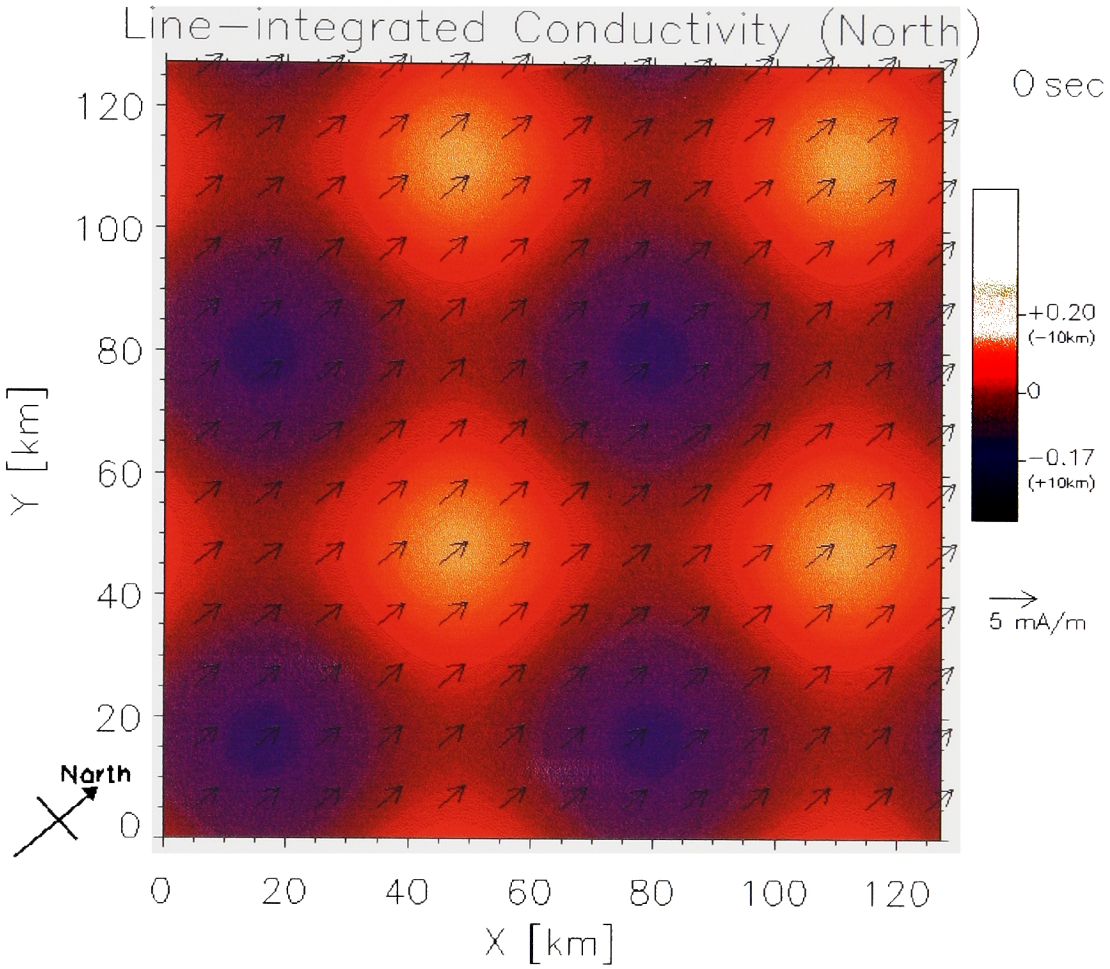
Line−integrated Conductivity (North)
0 sec
+0.20
(−10km)
0
−0.17
(+10km)
5 mA/m
North
Y [km]
X [km]
0
20
40
60
80
100
120

Figure 24 (a).

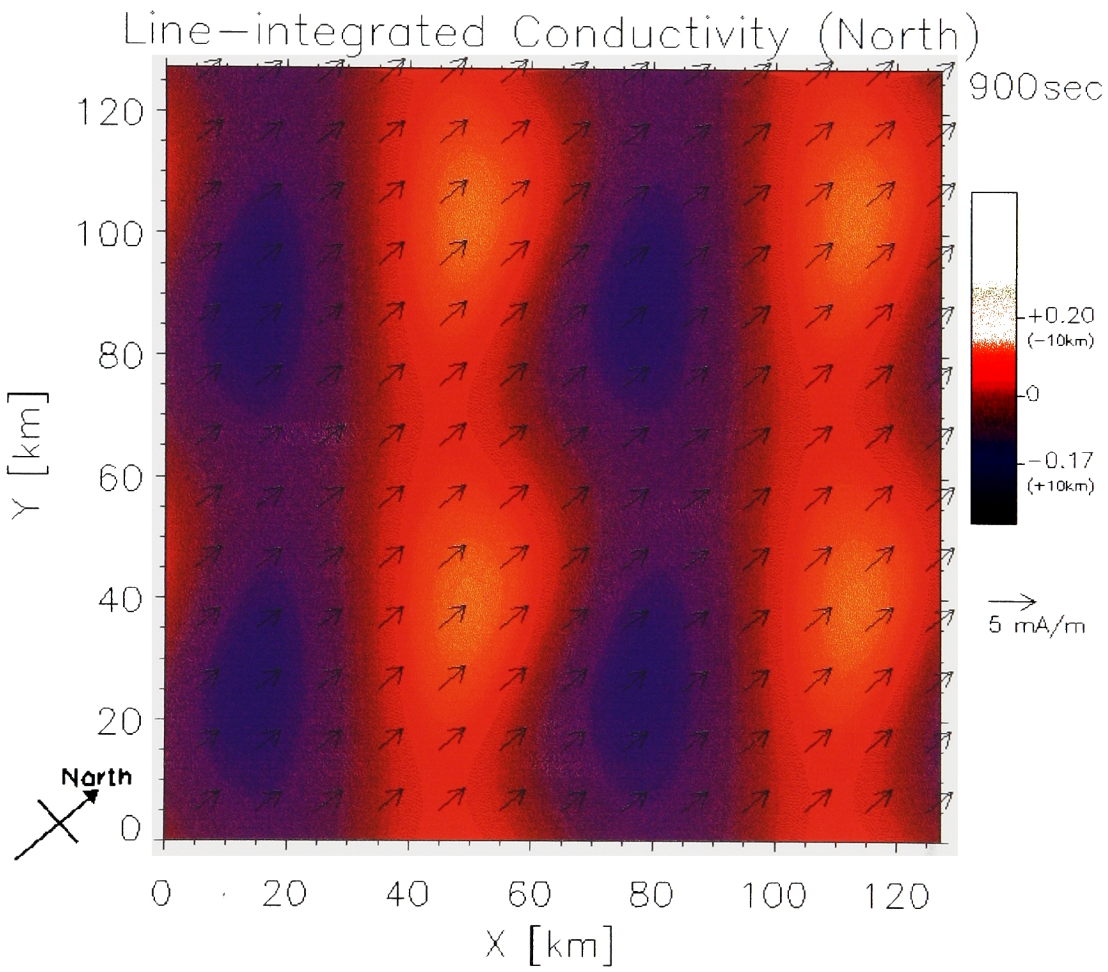
Line−integrated Conductivity (North)
900sec
+0.20
(−10km)
0
−0.17
(+10km)
5 mA/m
North
Y [km]
X [km]
0
20
40
60
80
100
120

Figure 24 (b).

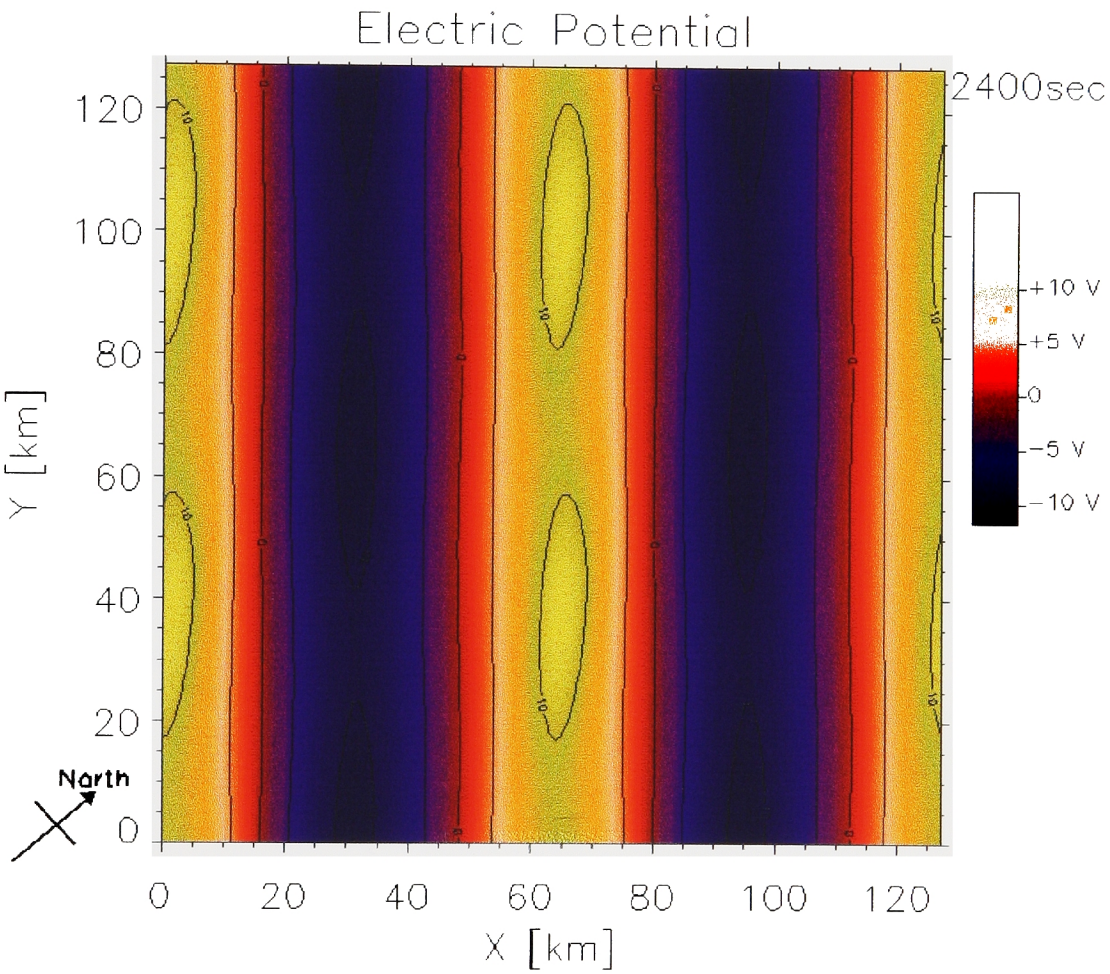
Electric Potential
2400sec
+10 V
+5 V
0
−5 V
−10 V
Y [km]
X [km]
North
0
20
40
60
80
100
120

Figure 25.

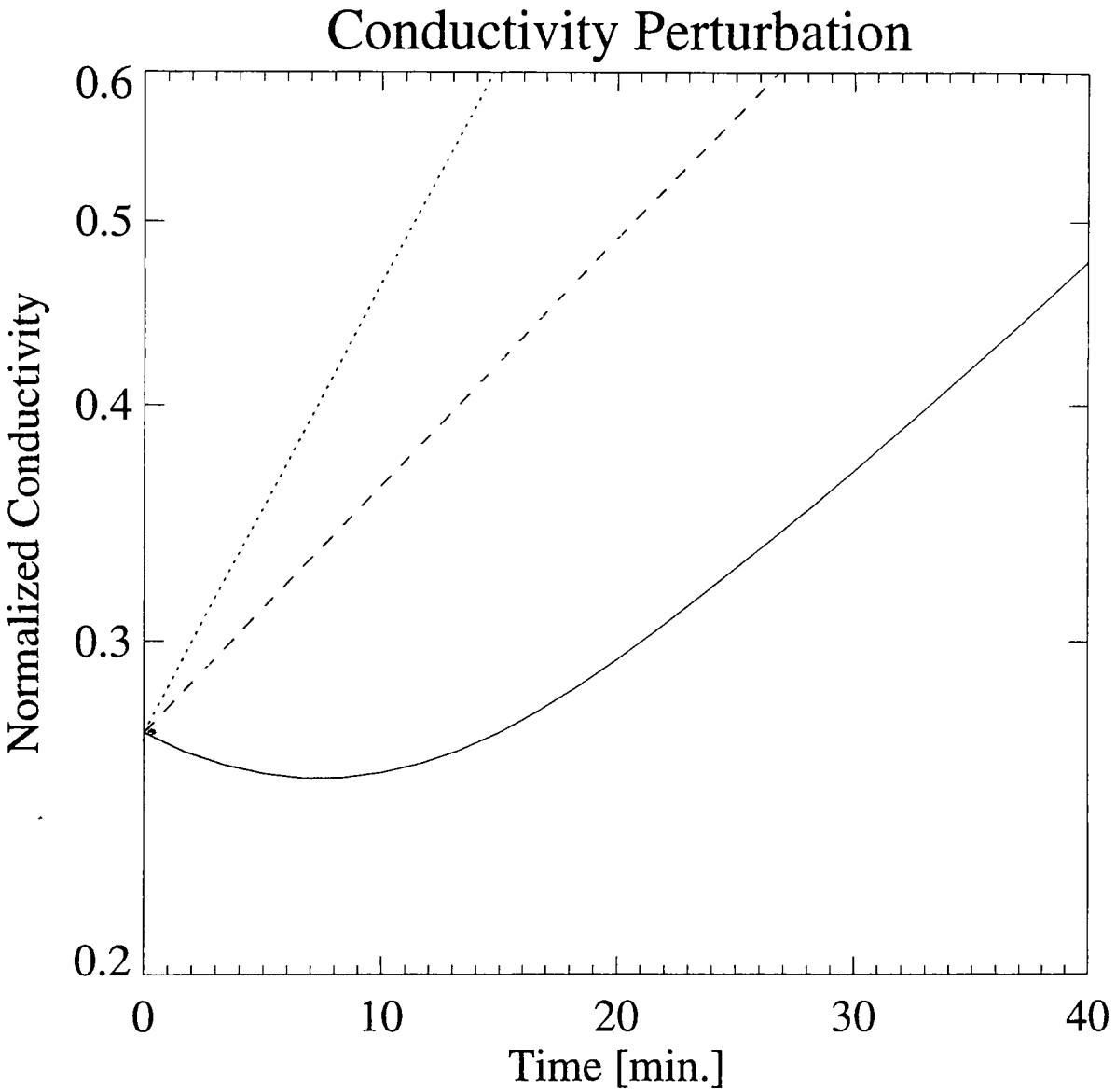
Conductivity Perturbation
Normalized Conductivity
0.6
0.5
0.4
0.3
0.2
0
10
20
30
40
Time [min.]

Figure 26.

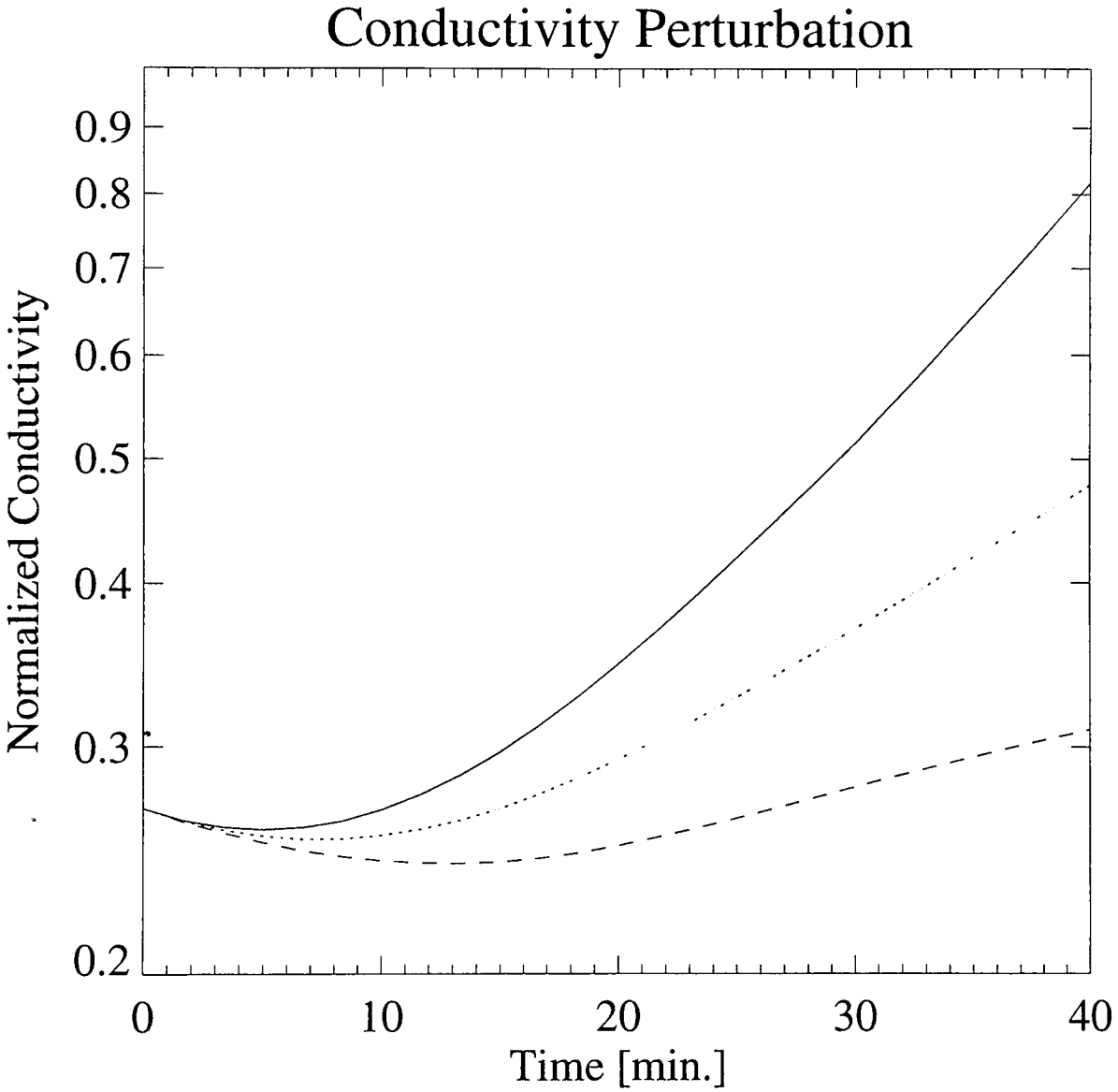
Conductivity Perturbation
Normalized Conductivity
0.9
0.8
0.7
0.6
0.5
0.4
0.3
0.2
0
10
20
30
40
Time [min.]

Figure 27.

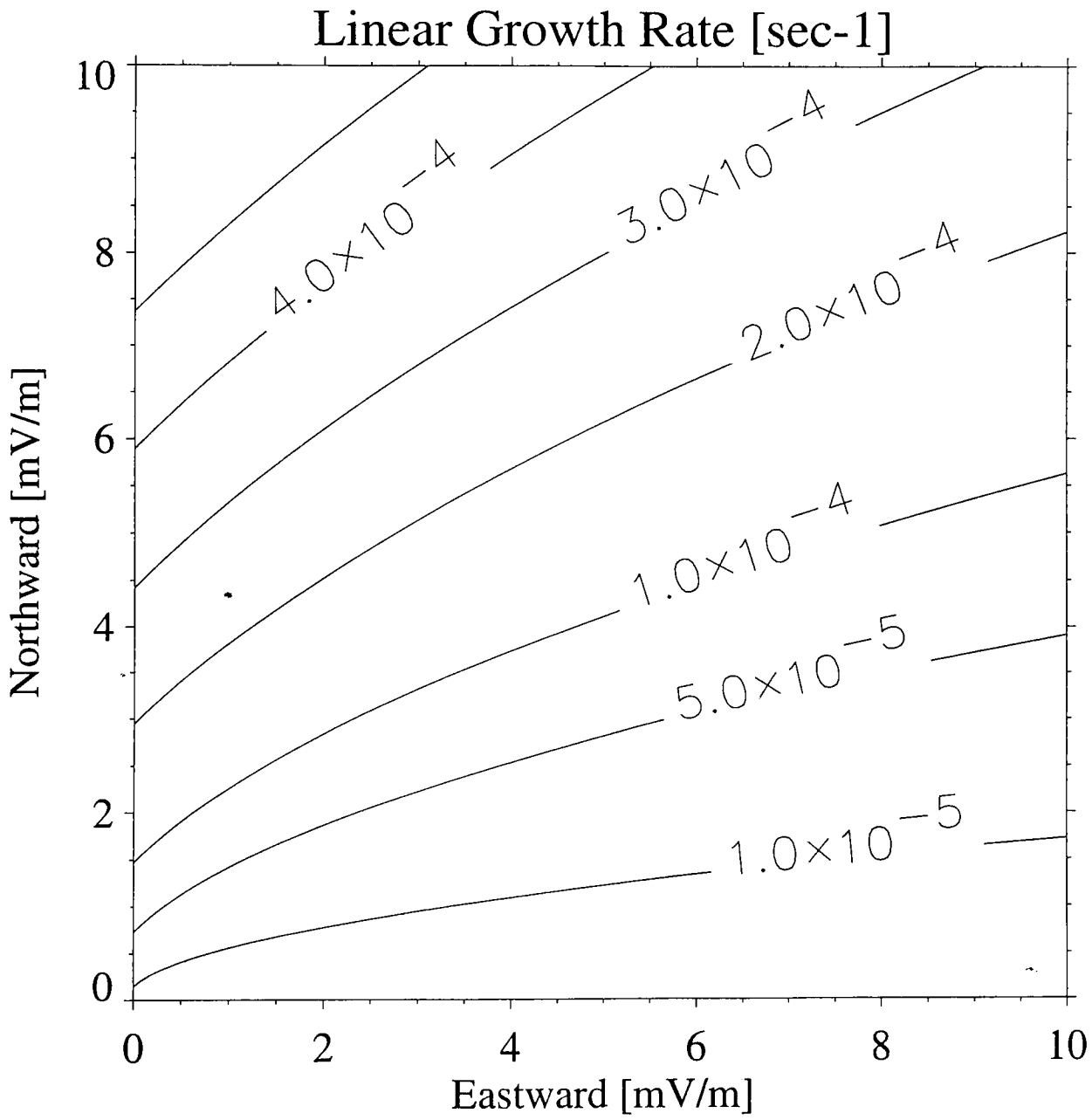
Linear Growth Rate [sec-1]
4.0×10⁻⁴
3.0×10⁻⁴
2.0×10⁻⁴
1.0×10⁻⁴
5.0×10⁻⁵
1.0×10⁻⁵
Northward [mV/m]
Eastward [mV/m]
0
2
4
6
8
10

Figure 28.

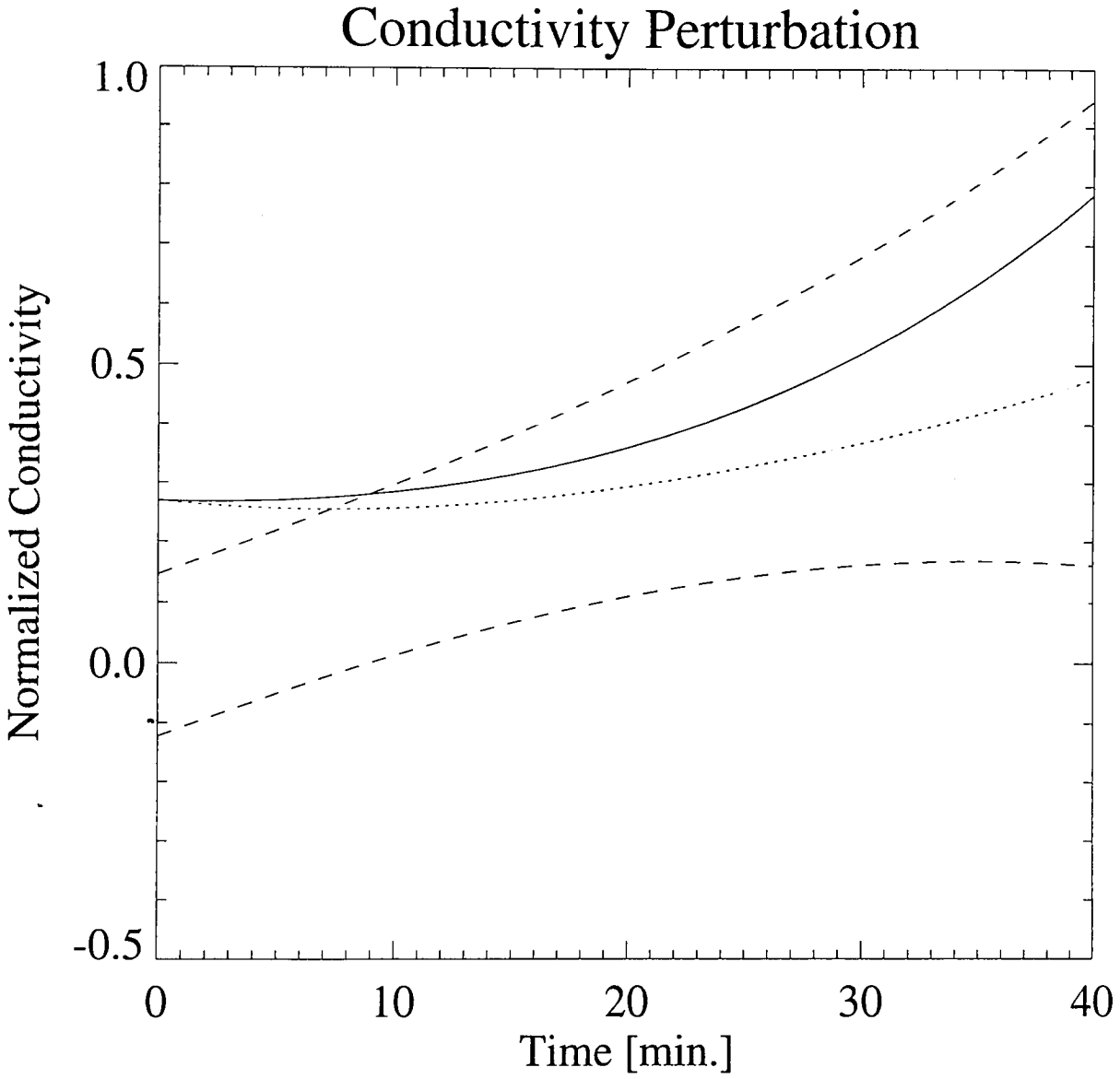
Conductivity Perturbation
Normalized Conductivity
1.0
0.5
0.0
-0.5
0
10
20
30
40
Time [min.]

Figure 29.

Papers

1. Conjugate Occurrence of the Electric Field Fluctuations
in the Nighttime Midlatitude Ionosphere
A. Saito, T. Iyemori, M. Sugiura, N.C. Maynard, T.L. Aggson, L.H. Brace,
M. Takeda, and M. Yamamoto

Journal of Geophysical Research, vol. 100, 21,439-21,451, 1995

2. Conjugate Observations of the Mid-latitude Electric Field Fluctuations
with the MU Radar and the Freja Satellite
A. Saito, T. Iyemori, L.G. Blomberg, M. Yamamoto, and M. Takeda

submitted to Journal of Atmospheric and Terrestrial Physics.

3. Evolution Process of Tens Kilometer Scale Irregularities
in the Nighttime Mid-latitude Ionosphere
A. Saito, T. Iyemori, and M. Takeda

submitted to Journal of Geophysical Research.